Single-Phase Crossflow Mixing in a Vertical Tube Bundle Geometry

An Experimental Study

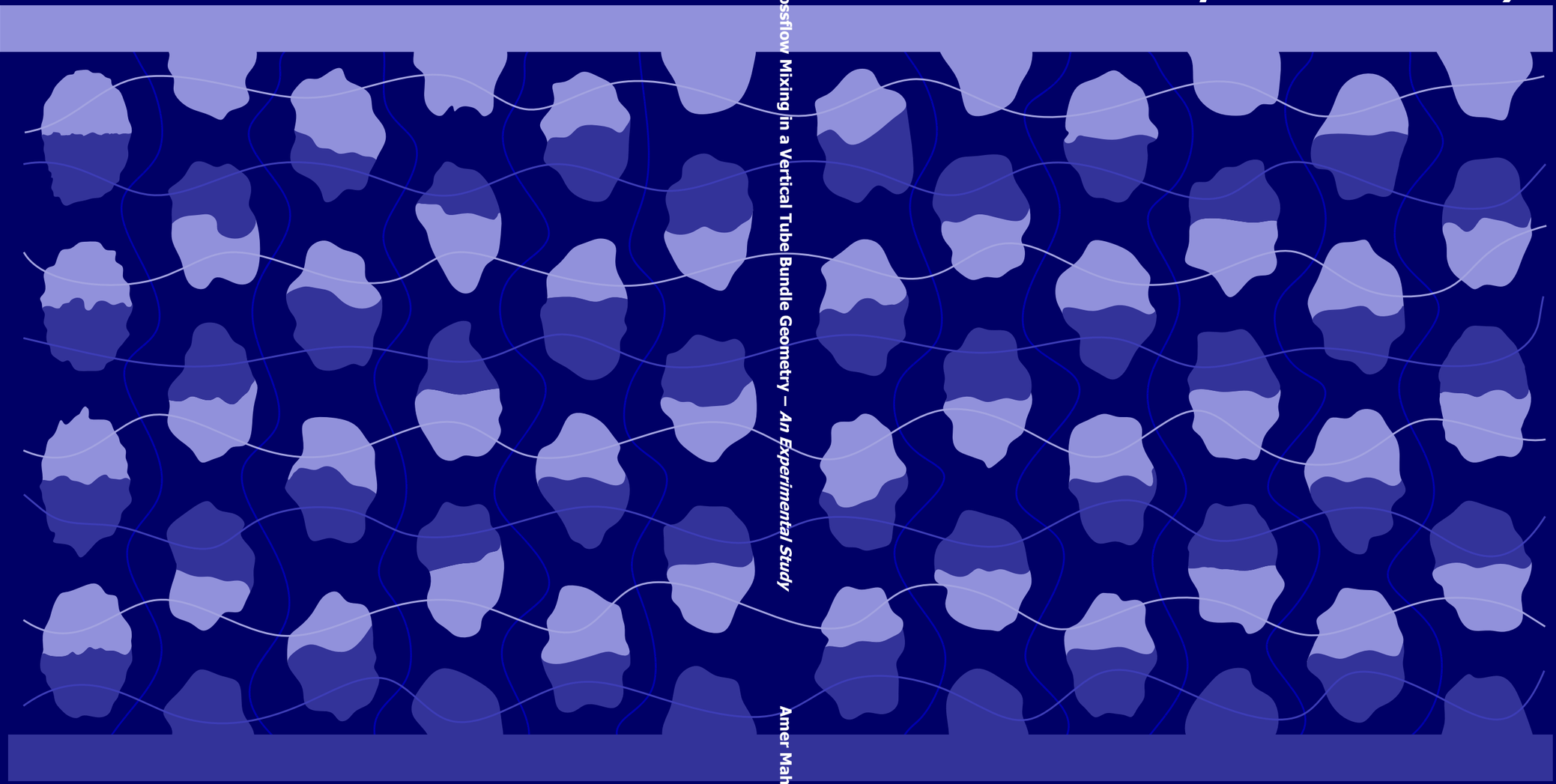

Single-Phase Crossflow Mixing in a Vertical Tube Bundle Geometry – An Experimental Study
Amer Mahmood

Amer Mahmood

Uitnodiging

Voor het bijwonen van de openbare verdediging van mijn proefschrift op:

Donderdag 23 juni 2011 om 10:00 precies in the Science Centre, Mijnbouwstraat 120, Delft

Aansluitend is er een receptie

Amer Mahmood
PNR-R3, Mekelweg 15, 2629 JB, Delft
samasl@yahoo.com

Single-phase crossflow mixing in a vertical tube bundle geometry

An experimental study

Proefschrift

ter verkrijging van de graad van doctor
aan de Technische Universiteit Delft,
op gezag van de Rector Magnificus prof. ir. K.C.A.M. Luyben,
voorzitter van het College voor Promoties,
in het openbaar te verdedigen op donderdag 23 juni 2011 om 10:00 uur

door

Amer MAHMOOD

Master of Science in Nuclear Engineering
Quaid-i-Azam University, Islamabad, Pakistan
geboren te Lahore, Pakistan

Dit proefschrift is goedgekeurd door de promotoren:

Prof. dr. ir. T.H.J.J. van der Hagen
Prof. dr. R.F. Mudde

Samenstelling promotiecommissie:

Rector Magnificus,	voorzitter
Prof. dr. ir. T.H.J.J. van der Hagen,	Technische Universiteit Delft, promotor
Prof. dr. R.F. Mudde,	Technische Universiteit Delft, promotor
Prof. dr. ir. J. Westerweel,	Technische Universiteit Delft
Prof. dr. ir. J.J.H. Brouwers,	Technische Universiteit Eindhoven
Prof. S. Tavoularis,	University of Ottawa, Ontario, Canada
Dr. ir. M. Rohde,	Technische Universiteit Delft
Dr. eng. T. Ikeno,	Nuclear Fuel Industries Ltd., Osaka, Japan

Published by: Uitgeverij BOXPress, Oisterwijk
Printed by: Proefschriftmaken.nl
ISBN 978-90-8891-301-3

Keywords: Coherent vortices, tube bundle, crossflow, mixing, tracer injection, PIV, LDA,

The research described in this thesis was performed in the section Physics of Nuclear Reactors (PNR), of the department Radiation, Radionuclides & Reactors (R3), of the Delft University of Technology, Delft, The Netherlands.

PRINTED IN THE NETHERLANDS

Summary

Among the roughly 450 nuclear power stations worldwide, most reactors are so-called Light Water Reactors (LWR). Two main LWR's designs exist, i.e. the Boiling Water Reactor (BWR) and the Pressurized Water Reactor (PWR). The operation limits of a LWR and its design must be such that the probability of damage to the fuel rods (arranged in a vertical tube bundle configuration) due to overheating is minimal. The fuel rods overheating might occur due to (i) the dual role of light water as a coolant and a moderator resulting in a feedback loop between the neutronics and the thermal hydraulics of the core, and (ii) the Critical Heat Flux (CHF) phenomenon, i.e., the heat flux causing the departure from nucleate boiling (in a PWR) and the liquid film dry out at the fuel cladding surface (in a BWR). In this context, the radial, inter-channel transport of heat/vapor (i.e., crossflow mixing) has an important bearing on assessing the probable damage to the fuel rods. Furthermore, the crossflow mixing of vapors can outset local instability through the nuclear feedback mechanisms resulting in power and flow oscillations. Motivated by these safety aspects of a LWR, the aim of the current study was to explore, in depth, the crossflow mixing in a vertical tube bundle geometry and to develop a mixing model by taking into account the shortcomings of the existing models.

Most of the existing crossflow mixing correlations/models are setup for turbulent flows while omitting the laminar and transitional flows that may exist in nuclear reactors. Moreover, in most of the cases these correlations were the outcome of experimental studies performed by using intrusive measurement techniques that have the disadvantage of inducing disturbances in the flow field. Finally, the issue of the role of secondary flows to crossflow mixing has been unclear for many years.

Considering the above-mentioned issues, an experimental study, supported by a few numerical simulations, was performed to identify different fluid flow patterns in a vertical tube bundle/similar geometry and the contribution of these patterns towards the lateral inter-channel transport of a passive scalar (such as heat). The geometries considered were compound channels connected by a rectangular gap, compound channels connected by a curved gap and a 4 x 4 tube bundle geometry. The experiments were performed in water at isothermal, single-phase flow and ambient operating conditions for channel Reynolds numbers ranging from approximately 900 to 22,000.. In the compound channels configuration, the flow field measurements were carried out by using Particle Image Velocimetry (PIV) for a range of gap sizes. For the tube bundle geometry, Laser Doppler Anemometry (LDA) was used for local velocity measurements.

The experimental results show that counter rotating coherent vortices exists adjacent to the channel-gap interface for all flow regimes, i.e., laminar, transitional and turbulent flows. These coherent vortices result in periodic crossflow zones in the gap region. These crossflow zones are transported in the streamwise direction (i.e., along the length of the rod bundle) without losing their characteristics. The root mean square of the spanwise velocity pulsations in

the gap region provides a good measure of the crossflow. In comparison with the large-scale structures, the secondary flows contribution towards crossflow appears to be insignificant (i.e. in the order of a few percent of the bulk velocity). As compared to the experimental findings, the Large Eddy Simulations (LES) adequately captured the characteristics of large-scale coherent structures. Furthermore, a comparison of the coherent and incoherent parts of the velocity field, for laminar flow in the gap region, revealed that the former governs the transport of high momentum fluid in the radial direction.

In order to be able to measure the velocities inside the bundle geometry with LDA, a Refractive Index Matching (RIM) technique was used. For this technique, Fluorinated Ethylene Propylene (FEP) was used as tube material. It had been shown that FEP could be effectively used as a solid RIM material with water at ambient conditions. A suitable thickness of FEP, however, needs to be selected to account for the attenuating effect.

Experiments on the radial mixing of a passive scalar induced by crossflow show that the mechanisms responsible for the inter-channel mixing depend on the gap hydraulic diameter. For large gap hydraulic diameters, turbulent mixing is the only mechanism responsible for the crossflow mixing. For medium-sized gap hydraulic diameters, both coherent structures and turbulent mixing (due to the turbulence in the gap region not occupied by the structures) contributes towards the crossflow mixing. For small gap hydraulic diameters, coherent structures are the only possible mean of crossflow mixing. Since the gap size of fuel rods bundle, in most LWR's, falls within the range of medium-sized gap hydraulic diameters, both mechanisms are expected to contribute towards crossflow mixing. If present, the coherent structures were found to impart a significant contribution towards crossflow mixing for all channel Reynolds numbers.

During the modeling phase, an important variable affecting the crossflow mixing, being the residence time of a scalar in a coherent structure, was identified. The residence time is a function of the spanwise and streamwise structure length, the root mean square of the spanwise velocity pulsations in the gap and the minimum gap spacing along the transverse axis. Based on this residence time concept, a continuous stirred tank (CST) based crossflow mixing model has therefore been proposed for the full range of channel Reynolds numbers. The model predicts the inter-channel crossflow mixing using the structure characteristics, i.e., the residence time of tracer in a structure and the streamwise structure velocity. By using the experimental observations, the model is finally evaluated in terms of pre-determinable parameters, such as, fluid bulk velocity and the gap hydraulic diameter. The model predictions are found to be within a band of ±20% of the experimental values for the full range of channel Reynolds numbers. Since the proposed model covers a large range of Reynolds numbers, it is expected to enhance the crossflow mixing prediction capabilities of existing LWR safety analysis codes for all coolant flow conditions and, consequently, to help to improve the overall safety of future nuclear reactor systems.

Samenvatting

Onder de 450 kerncentrales die op de wereld aanwezig zijn, is het merendeel een licht-water reactor (LWR). De licht-water reactoren kunnen ingedeeld worden in twee categorieën, te weten de kokend water reactor (BWR) en de druk water reactor (PWR). Een LWR moet zodanig ontworpen zijn dan de kans op schade aan de brandstof (in de vorm van een vertikale bundel van brandstofstaven) door oververhitting minimaal is. Een belangrijke oorzaak voor oververhitting is het verschijnsel van de kritische warmteflux (CHF), waar bij een bepaalde warmteafgifte in een PWR een isolerende dampfilm aan het oppervlak van de brandstof ontstaat, en in een BWR de koelende vloeistoffilm aan het brandstofoppervlak verdwijnt. Om schade aan de nucleaire brandstof te voorkomen is het dan ook van groot belang om het radiale transport van bijvoorbeeld warmte en damp tussen de subkanalen goed te begrijpen. Het doel van dit onderzoek is dan ook om dit radiale transport (Eng: cross-flow mixing) in een reactorbundel in detail te onderzoeken en een model hiervoor te ontwikkelen dat bepaalde tekortkomingen in huidige modellen en correlaties aanvult.

De huidige modellen en correlaties zijn met name ontwikkeld voor turbulente stroming. Laminaire stroming en stroming in het overgangsgebied van laminair naar turbulent worden dus veelal niet meegenomen. Bovendien zijn deze correlaties vaak ontwikkeld met behulp van instrusieve meettechnieken, welke de stroming zèlf verstoren en het resultaat dus nadeling kunnen beïnvloeden. Een discussie die nog steeds speelt is de bijdrage van secondaire stroming aan cross-flow mixing. Hierover bestond voor dit onderzoek nog veel onduidelijkheid.

Om deze redenen is dit experimentele (en voor een klein deel numerieke) onderzoek opgezet. Het doel van dit onderzoek is om de stroming in een vertikale reactorbundel te onderzoeken en te bepalen in hoeverre deze stroming het radiale transport van een scalaire grootheid (zoals warmte) beïnvloedt. De geometrieën die gebruikt zijn zijn twee kanalen verbonden door een rechthoekige spleet, twee kanalen verbonden door een gebogen spleet en een bundel bestaande uit 4x4 staven. De experimenten zijn uitgevoerd met water onder isotherme, één-fase-, en omgevingscondities, waarbij het Reynoldsgetal van de opstelling (betreffende het doorstroomde oppervlak van de gehele geometrie) gevarieerd is tussen 900 en 22,000. In de geometrieën die bestaan uit twee kanalen is de stroming gemeten met behulp van Particle Image Velocimetry (PIV), in de bundel is Laser Doppler Anemometrie gebruikt.

De experimenten tonen aan dat voor elk stromingsregime tegendraaiende, coherente vortices worden gevormd in het overgangsgebied tussen de spleet en de subkanalen. Deze coherente vortices vormen periodieke zones waarin het radiale transport (Eng: cross-flow) plaatsvindt, en bewegen opwaarts in de geometrie (dus met de hoofdstroming mee) zonder

noemenswaardig te veranderen. De RMS waarde van de fluctuaties in de laterale stroomsnelheid in de spleet is een goede graadmeter voor de cross-flow. De bijdrage die secondaire stroming levert aan de cross-flow blijkt vrijwel verwaarloosbaar te zijn ten opzichte van de coherente vortices (in de orde van een paar procent van de bulksnelheid). Ook uit Large Eddy simulaties (LES) komt duidelijk naar voren dat er grote, coherente vortices worden gevormd en dat, voor laminaire stroming in de spleet, het coherente deel van de stroming het radiale transport domineert.

Om de snelheden in de bundel met behulp van LDA te kunnen meten is een techniek toegepast waarin het bundelmateriaal dezelfde brekingsindex heeft als die van het water. Het materiaal dat bij omgevingscondities hiervoor geschikt werd bevonden is Fluorinated Ethylene Propylene (FEP). De dikte van het materiaal moet echter zo klein mogelijk zijn om de verzwakking van het laserlicht zo klein mogelijk te houden.

Experimenten waarbij de radiale menging (cross-flow mixing) van een passieve scalar werd gemeten laten zien dat de mechanismen die verantwoordelijk zijn voor deze menging afhankelijk zijn van de hydraulische diameter van de spleet. Voor relatief grote spleten blijkt radiale menging plaats te vinden door turbulentie. Voor kleinere spleten blijken zowel de coherente vortices als turbulentie (in de gebieden buiten de vortices) bij te dragen aan de radiale menging. Voor zeer kleine spleten wordt de stroming in de spleet laminair en bevorderen alleen de coherente vortices de radiale menging. Omdat de spleetgrootte van de meeste LWR's valt in de tweede categorie mag verondersteld worden dat in een LWR beide mechanismen een rol spelen bij cross-flow mixing. De bijdrage die de coherente structuren leveren is daarbij aanzienlijk voor alle Reynoldsgetallen van de opstelling.

Tijdens het opstellen van een model voor de radiale menging bleek de verblijftijd van de scalar in een coherente vortex een belangrijke parameter te zijn. Hierbij wordt gesteld dat de verblijftijd een functie is van de grootte van de vortex, de RMS waarde van de fluctuaties in de laterale stromingssnelheid in de spleet en de minimale spleethoogte. Om deze reden is een model voor de radiale menging opsteld dat gebaseerd is op de verblijftijd en dat voor een groot Reynoldsgetal-bereik gebruikt kan worden. In dit model wordt uitgegaan van geschakelde, continu doorstroomde, geroerde vaten (Eng: continuous stirred tank, CST). Het model is getest aan de hand van de experimenten, waarbij alleen de macroscopische grootheden (zoals de stromingssnelheid van de bulk en de hydraulische diameter van de spleet) als input dienden voor het model. Het model voorspelt de radiale menging met een maximale afwijking (ten opzichte van de metingen) van ±20%. Omdat dit model geschikt is voor een groot bereik van Reynoldsgetallen kan het model een positieve bijdrage leveren aan de verbetering van numerieke codes voor licht-water reactoren en dus aan de veiligheid van toekomstige kerncentrales.

Table of contents

Nomenclature

Latin

A	area	m^2
C	concentration	kg/ltr
C_{12}^R	cross correlation between two velocity signals	-
D	gap depth / diameter	m
d_f	fringe spacing	m
D_{dt}	discriminant of the characteristic equation of velocity gradient tensor	s^{-2}
D_h	hydraulic diameter	m
D_t	turbulent mass diffusivity	m^2/s
f_d	Doppler burst frequency	Hz
k	turbulent kinetic energy	m^2/s^2
L	length	m
P	pitch	m
q_x	spanwise inter-channel mass flux	kg/m^2 s
r	pipe radius	m
Re	Reynolds number	-
S	gap spacing	m
t / T	time	s
u, v, w	spanwise, axial and transverse velocity components, respectively	m/s
$\overline{u'v'}$, $\overline{u'w'}$, $\overline{v'w'}$	turbulent shear stress components	m^2/s^2
v^*	friction velocity	m/s
v_1	velocity at monitoring point 1	m/s
v_2	velocity at monitoring point 2	m/s
V	volume	m^3
V_{bulk}	streamwise bulk velocity	m/s
V_c	streamwise centerline velocity	m/s
W	width of a structure	m
x, y, z	spanwise, axial and transverse coordinates, respectively	m
y_{12}	streamwise distance between two velocity monitoring points	m
Z	impedance	ohm

Greek

α	angle between laser beams	radians
τ_{12}	time shift between two velocity signals	s
τ	residence time of tracer in a structure	s
Δ	shift in corresponding variable	-

δ	distance between the center of main channels	m
ν	kinematic viscosity	m^2/s
μ	dynamic viscosity	Pa s
θ	inter-channel tracer transfer	-
η	refractive index	-
ε	dissipation rate of turbulent kinetic energy per unit mass	m^2/s^3
ϕ	volumetric flow rate	m^3/s
Φ_u	spectral power density of spanwise velocity component	m^2/s
λ	wavelength	m
λ_{ci}	imaginary part of the complex eigen values of velocity gradient tensor	s^{-1}
ν_t	turbulent viscosity	m^2/s

Subscripts

1	channel 1	-
2	channel 2	-
12	from channel 1 to 2	-
21	from channel 2 to 1	-
b	blue	-
ch	channel	-
e	entrance	-
eff	effective	-
g	green	-
gap	related to gap	-
g-app	approximated from gap parameters	-
o	initial	-
p	pipe	-
v	violet	-

Superscripts

avg	average	-
CL	center line	-
cross	one channel to other in spanwise direction	-
ex	exit	-
exp	experimental	-
in	inlet	-
inflec.pt.	inflection point	-
max	maximum	-
min	minimum	-
out	outlet	-
rms	root mean square	-
str	structure	-
tur	turbulence	-

Abbreviations

APSD	Auto Power Spectral Density
BWR	Boiling Water Reactor
CCD	Charge-Coupled Device
CFD	Computational Fluid Dynamics
CFL	Courant – Friedrichs – Lewy Number
CST	Continuous Stirred Tank
CW	Continuous Wave
DNS	Direct Numerical Simulation
FEP	Fluorinated Ethylene Propylene
GS	Geometric Scale
LDA	Laser Doppler Anemometry
LES	Large Eddy Simulation
LWR	Light Water Reactor
NPP	Nuclear Power Plant
PIV	Particle Image Velocimetry
PMMA	Poly Methyl Methacrylate
POD	Proper Orthogonal Decomposition
PVC	Poly Vinyl Chloride
PWR	Pressurized Water Reactor
RANS	Reynolds Averaged Navier Stoke's
RIM	Refractive Index Matching
RMS	Root Mean Square
VS	Velocity Scale

1

Introduction

Vortex street in the wake of a cylinder

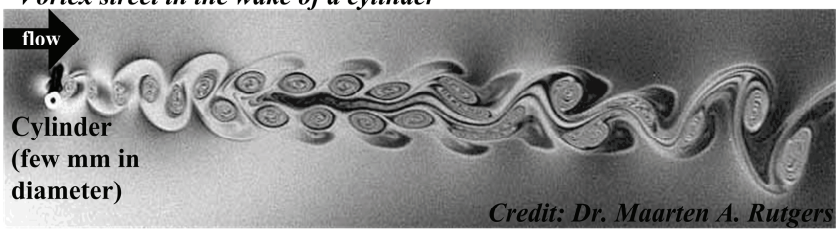

Stratus cloud patterns in the wake of an island

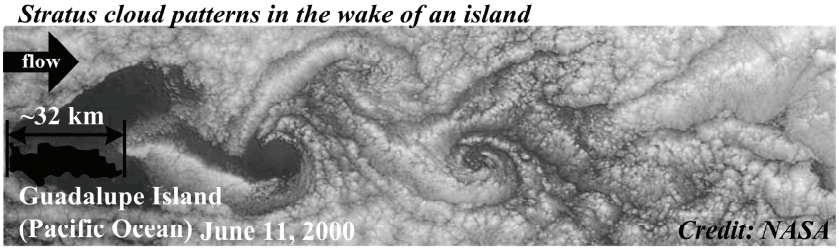

The patterns formed in a moving fluid have fascinated people since the earliest recorded observations of *Leonardo da Vinci*. To portray the random and chaotic behavior of these patterns, for the first time, he used the word "turbulence" (in Italian "la turbolenza", originating from Latin "turba" meaning turmoil). In contrast, fluid flows could exhibit organized motion of different scales. The images above show the diversity in the scale of these organized patterns for flow past an obstacle; a cylinder and an island. An interesting feature of these vortical patterns is their coherence, i.e., they retain their identity for a significant lifetime and appear repeatedly in more or less the same form (henceforth-

coherent vortices). Coherent vortices are common in nature and in different industrial applications, such as along the banks of a flood plain [1], in the wake of an island, in flat plate cooling fins [2] and in a tube bundle geometry [3] (a configuration often used in heat exchangers and nuclear reactors). Figure 1-1 shows a few of these examples.

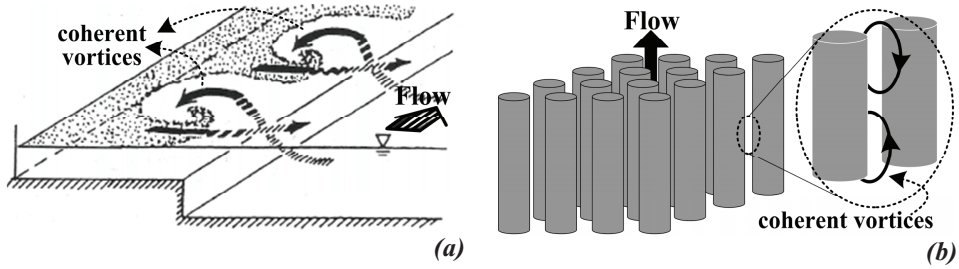

Figure 1-1: (a) Coherent vortices along the banks of a flood plain and their affect on sediment transportation [1], (b) Coherent vortices formed between two adjacent tubes in vertical tube bundle geometry (reconstructed from the model proposed by Möller [3]).

In addition to their aesthetic appearance, these coherent vortices have the potential of affecting the transport and mixing of passive particles (water masses, temperature, pollutants, etc.). By passive particles, we mean particles that take on the velocity of a fluid very rapidly without a significant influence on the flow field. This property marks the practical significance of the coherent vortices in meteorology, oceanography and different engineering applications. For example, environmental dispersion of pollutants, sediment transport along the banks of a flood plain and heat transfer in the core of a nuclear reactor (often being a tube bundle geometry).

Development of a deep understanding of the transport of the passive particles by coherent structures in the core section of a nuclear reactor (being a tube bundle geometry) is the primary aim of the work presented in this thesis. For single-phase flow conditions, experimental investigations constitute the major part of this study, with partial support from the numerical computations.

1.1. Motivation-Application to a nuclear power plant

Nuclear power plants (NPP) work in pretty much the same way as fossil fuel burning power plants, except that a "fission chain reaction" inside a nuclear reactor makes the heat instead. In the core of a nuclear reactor neutrons can be absorbed in the nuclei of the atoms of nuclear fuel (normally uranium), thereafter the nucleus can split and release energy in the form of heat. Fluid (coolant) pumped through the reactor takes the heat away to make

steam. The steam drives a turbine that drives an electricity generator to produce electricity. Figure 1-2 illustrates the electricity generation process in a nuclear power plant.

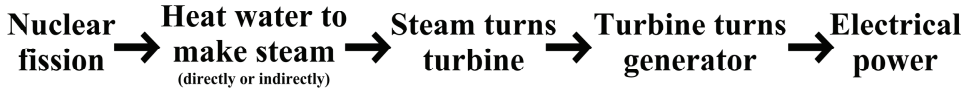

Figure 1-2: Basic processes involved in power production from a nuclear power plant.

Along with hydro, wind and solar power, nuclear power is the major source of "carbon-free" energy today. With growing worries about future energy needs and global warming, it is not surprising that governments and utilities are increasingly considering building a substantial number of additional nuclear power plants. However, for a large expansion of nuclear power to succeed, four critical problems needs to be addressed, namely, costs, safety, waste and proliferation [4]. In the past two decades, after the 1986 Chernobyl accident, the issue of safety has emerged as a prime challenge to the future growth of the nuclear power industry. The present work is a contribution towards the resolution of the safety issues of a nuclear power plant. The following paragraphs further elucidate this point.

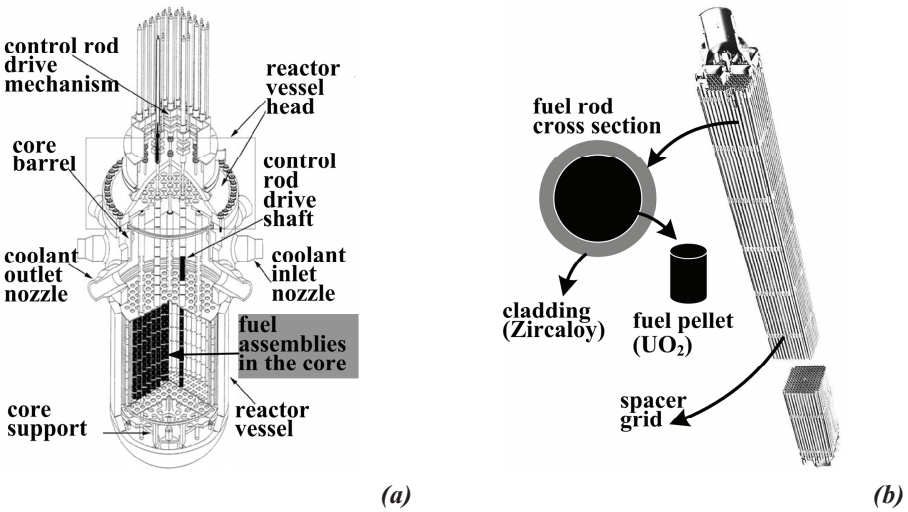

Figure 1-3: (a) Internal structures of a typical PWR reactor pressure vessel, (b) A PWR square arrayed fuel rod assembly with a cross sectional view of a fuel rod.

Two most popular types of Light Water Reactors (LWR) are the Boiling Water Reactor (BWR) and Pressurized Water Reactor (PWR) with coolant inside the core as a steam water mixture and water in the liquid phase, respectively. Figure 1-3 shows a typical core containing reactor pressure vessel and a fuel rod assembly used in a PWR. The fuel

rod assemblies, constituting the core, consist of square arrayed cladding tubes (generally made of zircaloy) filled with cylindrical pellets of fissile material, U-235 (an isotope of uranium), in the form of UO_2. Light water coolant not only removes the thermal energy generated by fission but also acts as a moderator to reduce the kinetic energy of the fission neutrons. The reduction in the kinetic energy of the fission neutrons is required to sustain the fission chain reaction, since the probability of fission of U-235 nucleus is higher for low energy neutrons, the so-called thermal neutrons. This linkage of fission process to the coolant/moderator temperature and density implies that in a LWR a feedback loop exists between the neutronics and the thermal hydraulics of the core.

An important safety aspect in a NPP is to maintain the integrity of the core, by avoiding the damage to the fuel rod and cladding due to overheating. The overheating can occur due to the Critical Heat Flux (CHF) phenomenon, i.e., the heat flux causing the departure from nucleate boiling (in a PWR) and the liquid film dry out at the fuel cladding surface (in a BWR). In this context, a better understanding of scalar (like heat and vapor) transport in fuel rod assemblies is required to assess the probable damage to the fuel rods. In addition, the radial transport of vapors can onset instability through the nuclear feedback mechanisms resulting in power and flow oscillations. Motivated by aforementioned safety aspects of a LWR, the present study focuses on exploring, in depth, the radial transport of a scalar in a vertical tube bundle geometry (representing fuel rods configuration in a LWR core).

1.2. Coherent vortices in a vertical tube bundle geometry

The fuel rod assembly in a LWR belongs to the class of square-latticed vertical tube bundle geometries. In this geometry, the flow area bounded by four tubes defines a sub-channel. Each sub-channel connects to the adjacent ones by a gap between two rods. The pitch-to-diameter ratio (P/D) of a tube bundle defines the gap spacing S, see Figure 1-4. In addition to the major axial flow in vertical direction, there also exists a transverse flow between two adjacent sub-channels, through the gaps between them, known as crossflow.

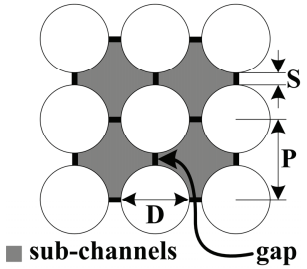

Figure 1-4: Cross-sectional view of a square pitched tube bundle defining sub-channels and gaps.

Rogers and Todreas [5] in 1968 identified the following two mechanisms constituting the single-phase crossflow in vertical tube bundle geometry and influencing the process of inter-sub-channel crossflow mixing (henceforth crossflow mixing):

(1) Diversion crossflow: Lateral flow caused by a net transverse pressure difference between adjacent sub-channels. Lateral pressure differences can result from different sub-channel hydraulic diameters, heat flux distributions and gradual or abrupt changes in flow areas caused, for example, by element bowing and tube supporting spacer grids, respectively.

(2) Turbulent crossflow: This is a result of stochastic flow and pressure fluctuations. Three transport mechanisms, in fully developed turbulent flow, near gap regions have been identified: convection by mean motion, turbulent convection, and turbulent diffusion [6]. The first mechanism represents secondary flows of Prandtl's second kind, generated by the non-uniformity of turbulent stresses. Turbulent convection and diffusion are associated with large-scale and small-scale eddies, respectively.

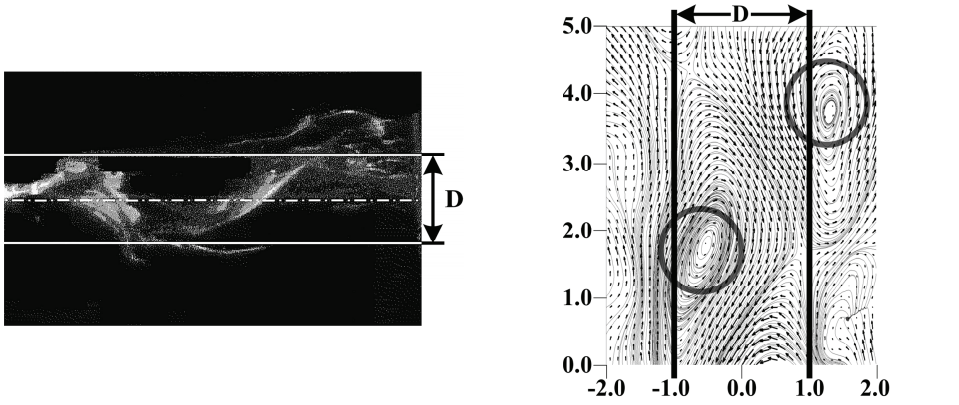

Figure 1-5: (a) An image showing the stream wise movement of the large-scale vortices in the gap region made visible by smoke injection [15], (b) 2D view of large-scale vortices in the gap region of compound rectangular channels [16], circles indicate the center region of a vortex.

In succeeding years, a number of researchers has verified the existence of large-scale coherent vortices near the gap region in a tube bundle geometry. In 1973-1974, Rowe *et al.* [7, 8] based on their measurements were the first to indicate that macroscopic flow processes exist adjacent to the gap region in a square arrayed tube bundle. Furthermore, they found out that rod gap spacing (P/D) is the most significant geometric parameter affecting the flow structure. In the later years, Möller, Rehme, Hooper, Wood, Wu and Trup, Meyer, Guellouz and Tavoularis, Lexmond *et al.*and Baratto *et al.* [3, 9, 10, 11, 12, 13, 14, 15, 16, 17] are few out of many who confirmed the findings of Rowe [7, 8] with their experiments. Figure 1-5(a) shows the stream wise movement of the large-scale

vortices in the gap region, obtained by Guellouz [15] using smoke injection technique. Figure 1-5(b) presents a more detailed picture of these coherent vortices, captured by Lexmond *et al.* [16] from their two dimensional flow field measurements.

Following the discovery of large-scale coherent vortices, in a tube bundle geometry, the next logical step was to quantify their contribution towards the crossflow mixing. Among most of the researchers, there is now a consensus that, for single-phase turbulent flow large-scale coherent vortices, existing near the gap region, are the main contributor to the crossflow mixing. Rogers and Tahir [18], Möller [19], Rehme [20], Lexmond *et al.* [16] and Guellouz and Tavoularis [21] are few of those who had demonstrated and stressed the dominant role of these vortices in the crossflow mixing.

In addition to experimental studies, a lot of information is available from the numerical investigations of the flow patterns in these configurations. Most of the computational work focused on the verification of the experimental results. For example, Biemüller *et al.* [22] obtained qualitative agreement between their Large Eddy Simulations (LES) and their measurements in two rectangular channels connected through a slot near the wall. Recently in 2009, by using a combination of LES and Proper Orthogonal Decomposition (POD), for the test section used by Lexmond *et al.*[16], Merzari *et al.* [23] verified the presence a mode containing alternating vortices on the edges of the narrow gap region. A description of the previous research work related to the coherent structures and corresponding crossflow mixing is included in the subsequent relative chapters.

The effect of large-scale coherent vortices on the crossflow mixing in a tube bundle geometry is rather a unique case. Since most of the above-mentioned studies were carried out for turbulent flows, many researchers had considered this phenomenon under the heading of turbulent crossflow mixing. Although eddies of different scales do exist in turbulent flows, conventionally these eddies are seen as non-coherent in nature. In fact, this is also the reason behind the use of the terminology ‘vortices’ instead of ‘eddies’, since the latter is considered associated with conventional turbulence. Furthermore, owing to the existence of these large vortices in laminar and transitional flows also, it seems reasonable to add this as a new crossflow mixing contributing phenomenon, in addition to the two mentioned above.

1.3. Objectives and scope of this study

The present study is meant to explore the crossflow mixing phenomenon in a vertical tube bundle or similar geometry, at isothermal, single-phase flow and ambient operating conditions. There are three possible choices to study the dynamics of complex fluid flows:

experimental, numerical or theoretical. These approaches have their own merits and demerits/limitations. For example, computational resources are still not fast enough to carry out numerical simulations for complex flows without any underlying assumptions. On the experimental side, although we treat a phenomenon directly, the number of measurement points limits the detailed evaluation of the flow domain. In fact, experiments, simulations and analytical theories in the field of fluid flow analysis complement each other. The major portion of the present work is based on measurements with some use of numerical computations to overcome the limitations of the experimental methods.

A comprehensive review carried out by Meyer [24] and Rehme [20] presented the historical evolution of the flow patterns identification and crossflow mixing in a tube bundle or similar geometries, respectively. For conciseness, only the main and the most relevant conclusions are included here. These reviews lead to the following unanswered issues:

- Most of the past work on flow patterns identification in a tube bundle relates to turbulent flows. This leads to the question, whether there may be any near gap flow patterns in transitional and laminar flows. Moreover, if they exist, how does their behavior depend on the gap geometry and the flow parameters? It is worth mentioning here that the heat removal from the core of a NPP operating at full power is achieved by turbulent flow of the coolant. However, during shut down or low power mode and in some accidental conditions the transitional or even laminar flow conditions might prevail in the core.
- The previous flow field measurements were generally performed by intrusive techniques. For near gap flow field investigation it would be beneficial to use a non-intrusive measurement technique, since the intrusively measuring probes have a known disadvantage of inducing distortion in the flow field.
- How would the flow field in the gap region look like? The previous studies merely pose hypothetical gap flow models, predicted from point measurements.
- Being a follow up procedure to flow patterns identification work, most of the crossflow mixing information available is for turbulent flows only.
- Generally, all the existing crossflow mixing correlations depends on the empirical data valid only for limited gap spacing of a tube bundle geometry.

Based on these issues the objectives set forth for this study are as follows:

1. To identify and characterize the near gap flow phenomena covering all three flow regimes, namely, laminar, transitional and turbulent. In addition, we will also comprehend the influence of the gap geometry on flow patterns. Moreover, we intend to use non-intrusive measurement techniques supplemented by detailed flow field visualizations. These visualizations will be helpful in better understanding the physical behavior of the near gap flow patterns.
2. For a tube bundle or similar geometries, the lack of crossflow mixing data for laminar and transitional flow conditions stems from the fact that for these flow conditions the flow pattern identification related information is scarce. Our second objective is to quantify the corresponding crossflow mixing for each flow condition covered in the first objective.
3. The third objective is to find out the interdependence of the crossflow mixing on the near gap flow patterns and the macroscopic parameters such as the geometrical parameters and mean flow.

The uniqueness of this study is that we are going to investigate the crossflow mixing over all three flow regimes and taking into account the gap geometry effect. It is envisaged that by comparison of the results we will be able to classify the crossflow mixing associated with a particular flow regime and geometry. This will further lead us to explore the possibility of a crossflow mixing model, applicable to all these conditions.

1.4. Thesis synopsis

The outline of the rest of this dissertation is as follows:

- Chapter 2 describes the results of experimental and numerical studies on crossflow in compound channels. The design idea, the experimental facilities, numerical setup and data analysis procedures are first documented. Coherent vortices characteristics, such as velocity and length in the streamwise direction, are presented as a function of gap geometry and Reynolds numbers. Furthermore, the contribution of secondary flows to crossflow as compared to coherent vortices is discussed.
- Chapter 3 presents results of experimental work carried out to investigate crossflow in a tube bundle geometry. Flow patterns responsible for crossflow are identified and their characteristics are presented on the same lines as done for compound channels

in the preceding chapter. The relevance of the compound channels results to tube bundles is discussed. In addition, the pros and cons of the use of the refractive index matching material in the tube bundle geometry are illustrated.

- Experimental work related to crossflow mixing in compound channels, i.e., inter-sub-channel transport of a passive scalar through the gap region, is presented in Chapter 4. First the description of the experimental technique is given, followed by the crossflow mixing results as a function of gap geometry and Reynolds numbers. Furthermore, the findings of an additional experimental study (for turbulent flows) are presented that segregates the contribution of large-scale coherent vortices and turbulent mixing towards crossflow mixing.
- In Chapter 5, a crossflow mixing model is proposed based on the results of the experimental work carried out for compound channels and the tube bundle. The modeling is approached in such a way that it covers laminar as well as turbulent flows. The shortcomings and assumptions used in the model are highlighted.
- Full-length conclusions are drawn in Chapter 6 along with recommendations for future studies.

2

Coherent vortices in compound channels

2.1. Introduction

The flow geometry in a tube bundle resembles two channels connected by a narrow gap (compound channels) and the fluid behavior, up to a certain extent, is similar in both cases [24]. Using this concept, many researchers have studied the flow patterns in compound channels, with the intention that their findings would be extendable to a tube bundle geometry. In fact, the first indication on the existence of large-scale coherent structures in a tube bundle came from van der Ros and Bogaardt [25] in 1970, from their heat transfer experiments in compound rectangular channels, see Figure 2-1. They reported, "the thermocouple signals at locations outside the centre gap are random turbulent but the recordings as well as the visible waves are very regular in amplitude and frequency for locations inside the gap".

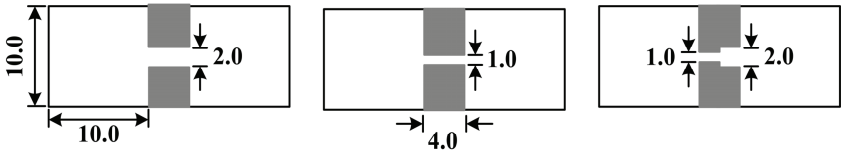

Figure 2-1: Compound channels connected by a narrow gap, cross section of setups used by Ros and Bogaardt [25].

In the following paragraphs, we present a review of literature available on the large-scale coherent vortices in compound channels and in channels containing a single rod. Based on our interest the review is limited to the single-phase, isothermal flow conditions. Although emphasis is on the experimental work, numerical studies are also considered. The figures shown in this section are not to scale and all dimensions are in millimeters.

Meyer and Rehme [14] experimentally investigated turbulent flow (Re_{ch}=2.5x10^5) of air through compound rectangular channels using hot-wire anemometry in 18 geometrical configurations, defined by different combinations of b1, b2, D and S, see Figure 2-2(a).

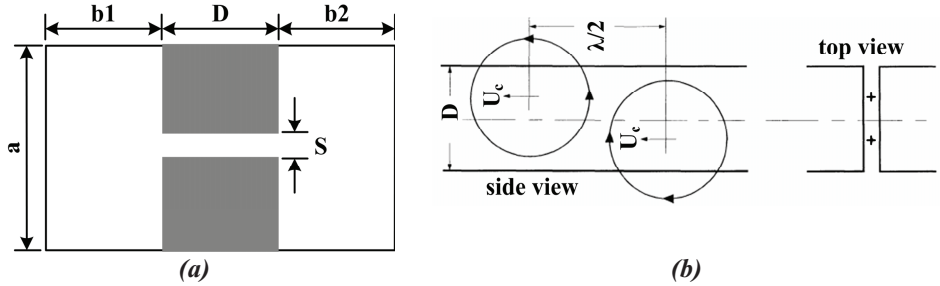

Figure 2-2: (a) Setup of compound rectangular channels used by Meyer and Rehme [14] and (b) proposed flow model in the gap region of depth D. Crosses in the top view indicate the center of the vortices.

Their flow model in the gap region, Figure 2-2(b), consists of two oppositely rotating vortices with centers located in the gap, on both sides of the centerline. The vortices in the gap, driven by the higher velocities in the channel region, move axially with velocity U_c. The diameter and the axial separation of two consecutive vortex centers was estimated equal to the gap depth (D) and λ/2, respectively, with λ being the length of one period of flow pulsations in the gap region. They also approximated U_c as a velocity at the edge of the gap and a length scale as a square root of width (S) times depth (D) of the gap, supplementing Möller's [3] finding in a 4 rod setup.

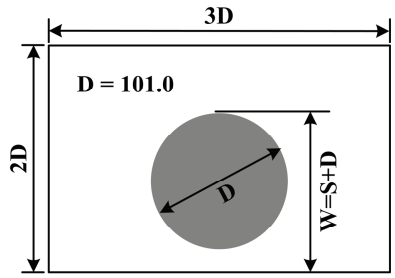

Figure 2-3: Cross section of the setup used by Guellouz and Tavoularis [15].

Guellouz and Tavoularis [15] investigated the behavior of large-scale vortices in the gap region formed between the rod and the plane wall in a rectangular channel containing a single cylindrical rod. With air as a working fluid, they used hot wire anemometry for velocity field measurements and smoke injection for flow visualization at Re_{ch} equal to 108,000. Top view of the experimental setup is shown in Figure 2-3. Their visualization results clearly showed that large-scale vortices occur at a regular interval across the gap. From the experimental findings they correlated the average streamwise convection speed (U_c) of the vortices and the streamwise spacing (λ) between two vortices to the bulk fluid velocity (U_{bulk}), the period of oscillations in the autocorrelation coefficient of the flow pulsations (T) and the gap spacing (W/D).

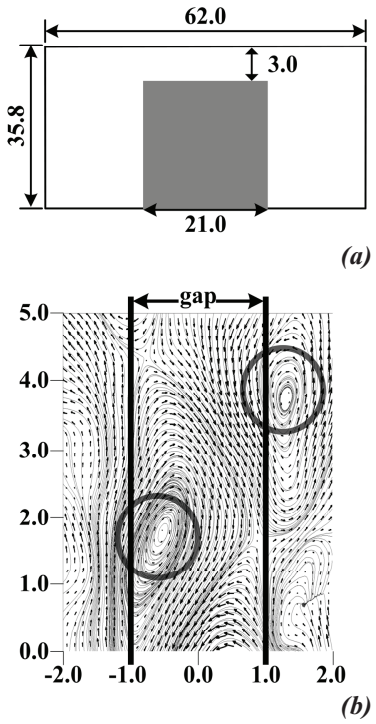

Figure 2-4: (a) Cross sectional view of the Lexmond *et al.* test section [16], (b) large scale vortices in the gap region, circles indicate the center of a vortex.

The preceding paragraphs show that the past experimental work, on flow patterns identification in compound channels, relates to turbulent flow and the flow field measurements were generally performed by hot wire anemometry, an intrusive technique. In 2005, Lexmond *et al.* [16] carried out experiments in a simple geometry of two rectangular channels connected by a near wall rectangular gap, see Figure 2-4(a). To visualize and characterize the vortex street in the gap region they used the non-intrusive 2D Particle Image Velocimetry (PIV) technique. As far as we know this was the first time use of the non-intrusive 2D PIV method in the category of compound channels. With water as working fluid, the Re_{ch} ranged from 800 to 10,000 and covered the full range of flow regimes. At $Re_{ch} >$ 1000, they observed a street of counter rotating vortices on either side of the gap, see Figure 2-4(b). The streamwise length of the vortices decreases with increasing Re_{ch} up to 2000, above which the average vortex length becomes constant (7±0.5 cm).

We have looked at the experimental work carried out over the years to identify the flow patterns, particularly large-scale coherent structures, in a tube bundle or similar geometries. In addition to this, a lot of work is available on the numerical investigations of the flow patterns in these configurations. Most of the computational work focuses on the verification of the experimental results acquired in the above-mentioned geometries. For example, Biemüllcr *et al.* [22] obtained qualitative agreement between their Large Eddy Simulations (LES) and their measurements in two rectangular channels connected through a slot near the wall, similar to the one shown in Figure 2-4(a). The LES results confirm the presence of two counter-rotating vortices with centers on opposite sides of the gap centerline. Chang and Tavoularis [26] performed numerical investigations for flow configuration shown in Figure 2-3. Recently in 2009, by using a combination of LES and Proper Orthogonal Decomposition (POD), for the test section used by Lexmond *et al.*[16], Merzari *et al.* [23] verified the presence a mode containing alternating vortices on the edges of the narrow gap region.

The primary aim of the present study is to develop a deeper understanding of the crossflow across the gap region connecting two sub-channels of a vertical tube bundle geometry. As a starting point, we have considered compound rectangular channels connected by a near wall gap, representing two interconnected sub-channels of a tube bundle geometry. The present work is in fact an extension of the study carried out by Lexmond *et al.*[16]: we have considered the effect of the variation in the gap shape and spacing on the near-gap flow patterns. The intention is to move in steps from a relatively simple gap geometry, i.e., rectangular, to the one that is more representative of the gap region in a tube bundle, the curved one. This study allowed us to examine the characteristics of the near gap large-scale vortices and the corresponding crossflow pulsations in the gap regions as a function of gap geometry for the full range of Reynolds numbers. Furthermore, the physical background of the origin of the large-scale vortices in above-mentioned geometries is also explored. We have used non-intrusive 2D Particle Image Velocimetry (PIV), for flow field investigations, to avoid the flow field disturbance associated with intrusive measurement techniques.

Since the measurements provided two dimensional flow field results, numerical calculations (at Reynolds number 2690) are used to supplement the experimental work in the third, i.e. gap perpendicular, dimension. Dominant contribution of secondary flows toward the crossflow, over large-scale vortices, in a tube bundle (or similar geometry) is still emphasized by some researchers [27, 28, 29]. Although, this topic is covered in detail in the next chapter (Chapter-3), the current numerical work also allowed us to examine the existence of the secondary flows and their contribution towards the crossflow, in comparison to the large-scale vortices.

2.2. Experimental setup

All the experimental work was carried out at ambient conditions using tap water as the working fluid. Velocity measurements within the test section were made by using two-component particle image velocimetry (PIV). For this study, and in the rest of the thesis, the Cartesian coordinate system is used, with x, y and z being the gap parallel, streamwise and the gap perpendicular directions, respectively (see Figure 2-5). The corresponding x, y and z-velocity components are represented as u, v and w, respectively. The bulk velocity, V_{bulk}, is calculated by dividing the total flow rate with the lateral cross sectional flow area of the setup. The channel Reynolds number (Re_{ch}) is defined according to Equation (2-1):

$$Re_{ch} = \frac{V_{bulk} D_h^{ch}}{\upsilon} \qquad (2\text{-}1)$$

where υ is the kinematic viscosity of water and D_h^{ch} is the hydraulic diameter based on the total lateral cross sectional flow area of the test section. The following paragraphs describe the test section, the measurement technique and the data processing methodology.

2.2.1. Test section

Figure 2-5 shows the detailed front and the cross sectional views of the two test sections considered. Both test sections consist of two vertical square ducts connected by a near wall gap region. Test section 1 (R-3) has a rectangular gap of depth (D) 21.0 mm and spacing (S) of 3.0 mm, see Figure 2-5(a, b). Test section 2 shown in Figure 2-5(c, d) has a curved gap region with D = 21.0 mm and S (in this case minimum gap spacing) = 2.0 mm (C-2) and 3.0 mm (C-3). The minimum gap spacing in test section 2 was adjusted by inserting a suitable padding between the base plate (wall A) and the solid channels partitioning duct G. The duct G was made of PVC while the other three walls were made of 8.0 mm thick glass/Perspex sheet to facilitate the PIV optics. For both test sections, the flow areas scaling and the gap spacings of 2.0 mm and 3.0 mm were based on typical LWR core sub-channel dimensions. Table 2-1 summarizes the geometric parameters for each test section.

Table 2-1 Geometric parameters of the test sections

Gap type	*Test section	S (mm)	D (mm)	Lateral cross sectional flow area (cm^2)	Lateral cross sectional wetted perimeter (cm)
Rectangular	R-3	3.0	21.0	16.5	27.32
Curved	C-2	2.0	21.0	15.3	25.86
Curved	C-3	3.0	21.0	15.5	25.66

** R=rectangular gap, C=curved gap, following digit represents the minimum gap spacing in mm*

Water from an overhead tank was re-circulated through the test section by a centrifugal pump. The water entering the test section from the bottom flows vertically upward and emerges at the top. Test section 2 has two inlets and two outlets while test section 1 has one inlet and two outlets, see Figure 2-5(a, c). A wedge shaped flow splitter divides the flow from the single inlet in case of test section 1. For all these experiments, the intention was to match the flow rate in both the channels as closely as possible. However, after working with R-3 it was realized that a better control over the flow rate through the test section can be obtained with two separate inlets, one for each channel. Shifting to two inlets, for C-2 and C-3, has shown significant improvement in the flow symmetry, see Figure 2-17 in § 2.5.2. Furthermore, uniform flow conditions for both the channels were ensured by making the downstream and upstream piping symmetric.

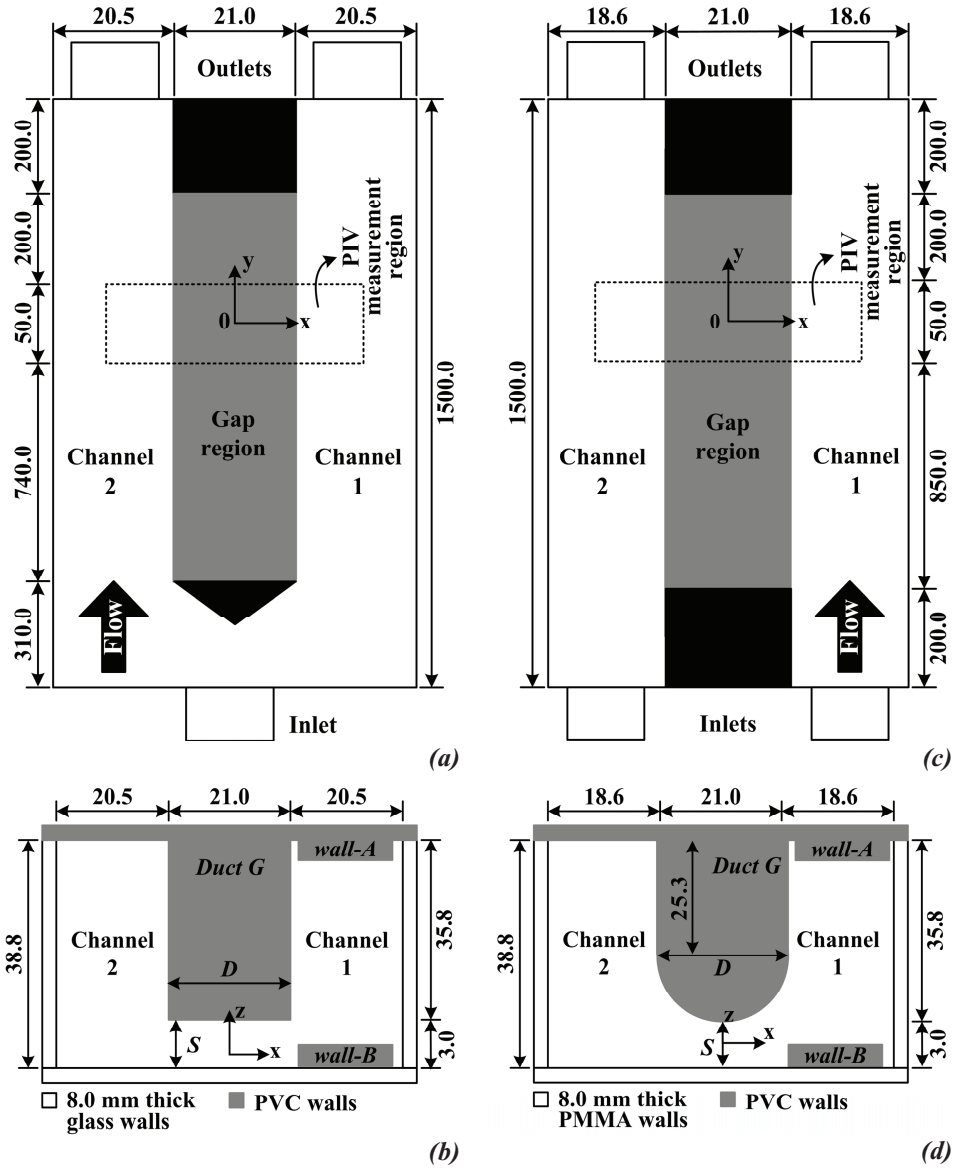

Figure 2-5: Test sections 1 and 2 with definition of the coordinate systems, gap depth and spacing. (a) and (c) show the front view of the test sections 1 and 2, respectively. The light grey colour along the axial direction represents the presence of the gap, whereas the dark shade represents the blockage of the gap. The cross-sectional view of test sections 1, (b), and 2, (d), show the inner dimensions.

(All dimensions are in mm, figures are not to scale.)

The experimental flow loop for C-2 and C-3 is shown in Figure 2-6. The volumetric flow rate was monitored by rotameters before the inlet and with electronic flow meters behind the outlets. The flow rate was controlled with an accuracy of ±2%.

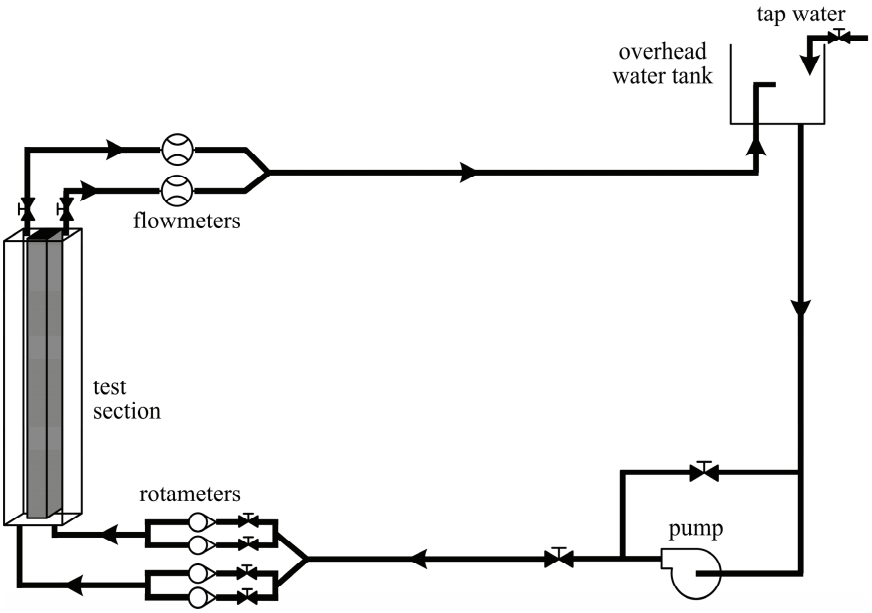

Figure 2-6: Experimental flow loop for test section 2. Same flow loop was used for test section 1 but with one inlet.

2.2.2. 2D PIV

The velocity field in the measurement section was determined using 2D-PIV [30]. The seeding particles, small enough to follow the flow but large enough to be detectable by the optical setup, were added to the fluid. A high intensity sweeping laser beam illuminates the particles. A high-speed camera captures the still images of these particles, separated by a short time interval. The displacement of the particles, determined by cross correlating two consecutive images, allows calculation of the velocity field in the plane of the laser sheet.

Figure 2-7(a) shows the PIV setup and the location of the laser sheet defining the xy measurement plane for the test section C-2/C-3. The laser used is a Spectra-Physics BeamLok 25 W continuous Ar-ion laser. Neutrally buoyant hollow glass spheres (Sphericel) of 11.0 μm average diameter and density of 1.1 gm/cm^3 were used as seeding particles. The seeding particles were added to water resulting in a theoretical particle concentration of at least 15 particles per interrogation window. A sweeping laser beam, obtained by reflecting a continuous wave (CW) laser beam on a parabolic mirror from an

14 faced rotating mirror, creates a 1.0 mm thick pseudo laser sheet, shown in Figure 2-7(b). Such a setup results in a high power sweeping laser beam, useful for PIV studies at higher Re_{ch}. A variable mirror frequency, ranging from 150 to 350 Hz, was used at different flow rates so that the particles displacement, between two consecutive images, remain less than 1/4th of the PIV interrogation window size. The laser sheet in the gap was aligned with reference to the main outer wall, the one facing the camera, by using the metallic guiding slots with opening of 1.0 mm, see Figure 2-7(a).

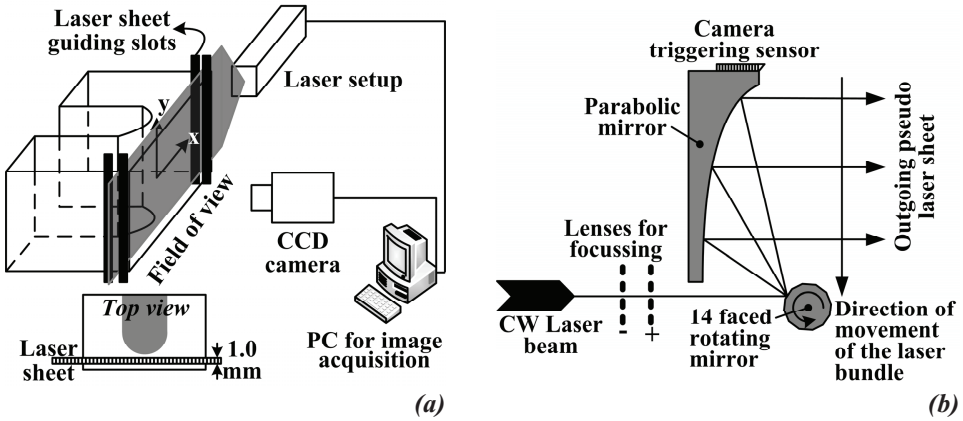

Figure 2-7: Schematic of the PIV setup. (a) Definition of the coordinate system, location of the laser sheet and the field of view, (b) creation of pseudo laser sheet by sweeping laser beam optics.

Still images were captured using a camera with a resolution of 532x516 pixels (DALSA CA-D6-0512, maximum of 262 frames per second) for low flow rates and 260x260 pixels (DALSA CA-D6-0256, maximum of 955 frames per second) for high flow rates. The signal from a photo diode, mounted at the top of the parabolic mirror, was used to trigger the camera. The size of the image was (**x** x **y**) = 5.0 x 5.0 cm and calibrated by recording a pre-defined scale. Particle displacement was analyzed using commercial PIV software "DAVIS 7.0" from recorded images after subtraction of a time averaged background. Local velocities were calculated in 32 x 32 and 16 x 16 pixels interrogation windows for 532 x 516 and 260 x 260 pixels resolution cameras, respectively, with 50% window overlap. Reported velocity field consists of 32 x 33 velocity vectors.

The PIV measurements for R-3 are a repetition of a similar study carried out by Lexmond *et al.*[16]. For R-3, the center of the PIV measurement plane needs to be located at z=0, i.e., 1.5 mm from the near gap outer wall. To approximate the maximum streamwise velocity in the PIV measurement plane, found at (x/D, y/D, z/D)=(1.0, 0.0, 0.0), we make

use of the so called Blasius seventh root law for turbulent velocity distribution in a pipe flow[31], given by Equation (2-2):

$$\frac{v}{v^{CL}} = \left(\frac{z}{r}\right)^{\frac{1}{7}} \tag{2-2}$$

where v is velocity at a distance z from the wall, r is the radius of the pipe and v^{CL} is the centerline velocity approximated from Equation (2-3):

$$\frac{V_{bulk}}{v^{CL}} = \frac{2}{[(m+1)(m+2)]} \tag{2-3}$$

with m=1/7. Figure 2-8 shows a comparison of Lexmond *et al.*[16] and current results with the Blasius approximation for turbulent flow ($Re_{ch} > 2000$).

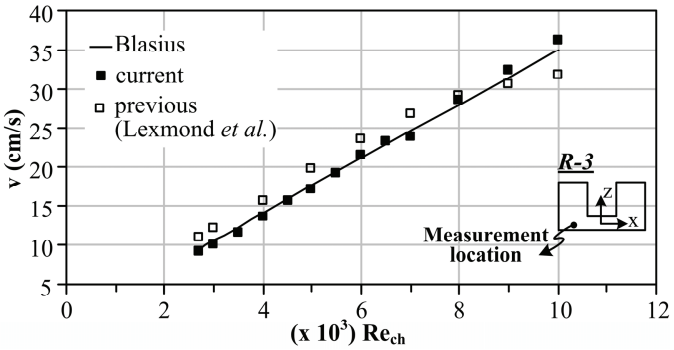

Figure 2-8: Comparison of streamwise velocity in the main channel region at (x/D, z)=(1.0, 0.0), obtained from the current study, by Lexmond *et al.*[16] and from the Blasius approximation, for R-3.

The current results match very well with the Blasius results, confirming the location of the PIV measurement plane located at z=0.0. The higher values of the streamwise velocity obtained by Lexmond *et al.* [16] for $2000 < Re_{ch} \leq 7000$ indicate that the position of the PIV measurement plane is located at z > 1.5 mm from the near gap main outer wall. The plausible reason for the decrease in the streamwise velocity for $Re_{ch} > 7000$ could be the choice of inappropriate PIV operational parameters. For example, Lexmond *et al.* [16] reported the use of a mirror frequency of 240±10 Hz for all Re_{ch}. For $Re_{ch} > 7000$, however, a higher mirror frequency is required in order to minimize the uncertainties in correlating the particle images in two subsequent frames - during the post processing.

2.3. Numerical setup

Numerical work for R-3, at $Re_{ch} = 2690$ ($V_{bulk} = 11.1$ cm/s), was initiated after the experimental results were obtained. Water, at ambient conditions, was considered as the

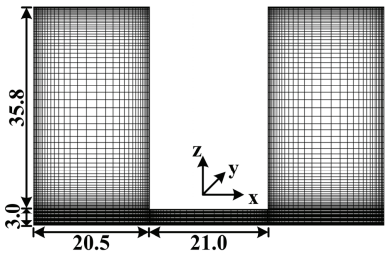

Figure 2-9: Cross sectional view of grid scheme 3 used for LES computations. Along the streamwise (y-direction) grid points are uniformly distributed.

working fluid. The generic commercial CFD code FLUENT, version 6.2 based on the finite volume method, was used to perform the unsteady simulations. The flow domain dimensions in the x and z direction were kept the same as of the experimental setup shown in Figure 2-5(b). For grid generation the pre-processing code GAMBIT was used. A structured grid was generated with a uniform distribution of mesh points in the streamwise, y-direction, while a non-equidistant mesh was used in the x and z directions in order to be able to model the gap and near wall regions by a relatively fine mesh. Three different mesh schemes were used (see Table 2-2) to study the effect of grid resolution on the parameters of interest. To resolve the steep velocity gradient in all near wall regions without using wall functions, five grid points were placed in the region (X^+ and Z^+) < 10, with the first grid element located at (X^+ and Z^+) = 1. Figure 2-9 presents the distribution of mesh points in the xz-plane for grid type-3. No-slip conditions were applied at all solid walls.

Table 2-2 Grids used for computations.

Grid	Number of mesh points (x × y × z)
Type-1	91 × 117 × 50
Type-2	91 × 501 × 50
Type-3	127 × 117 × 76

At first stage, using the boundary conditions of velocity inlet (plug flow) and constant pressure outlet, the computations were carried out for the complete experimental domain using the RANS (k-ω model) method. The use of the k-ω model [32] was motivated by the fact that the k-ω model incorporates a low Reynolds number correction to the turbulent viscosity and the production term of ω, required to calculate both low velocity (gap) and high velocity regions (channels). With these conditions and for all mesh sizes, the k-ω model was able to resolve the structures (for the definition of a structure see §2.5.1) near the gap region. However, the streamwise structure length, in the gap region, was over predicted nearly 2.5 time the experimental results.

Since the experimental results had shown existence of large-scale vortices near the gap region, the next choice was LES [33]. The intention was to increase accuracy in the prediction of the near gap streamwise structure length by using the potential of LES to

simulate the large-scale vortices with a coarser mesh size as compared to the mesh requirements for DNS. Additionally, periodicity was applied in the streamwise direction to get a fully developed velocity profile at the inlet over a shorter length of the flow domain. The streamwise length of the flow domain selected as 28.0 cm equaling to nearly four times the experimentally found streamwise structure length. Based on the numerical studies carried out by Biemüllcr *et al.*[22] and Merzari *et al.*[23], this domain length was assumed sufficient to produce results free of periodicity length effects. The streamwise structure length in the gap region obtained with LES and revised boundary condition for grid type-3 become comparable to the experimental findings. Therefore, the results of the grid type-3 using LES with periodic conditions at Re_{ch} = 2690 will be presented.

The results of the steady k-ω turbulent simulation were used as an initial condition for the LES simulations. The time step was selected such that the Courant-Friedrichs-Lewy number-CFL < 0.5 holds in the whole flow domain. A constant mass flow rate condition, corresponding to V_{bulk} and the cross-sectional area of the flow geometry, was imposed to drive the flow through the domain. A second order implicit scheme was used and central differencing for the spatial discretization. For pressure-velocity coupling the PISO (Pressure Implicit with Splitting of Operators) algorithm was used. From the experimental results, the existence of laminar and turbulent flow regions in the setup was anticipated. Therefore, dynamic Smagorinsky-Lilly model was used to calculate the sub-grid scale viscosity field, since this model predicts zero sub-grid scale viscosity in laminar regions of the flow. The cross velocity pulsations at the origin, located at the center of the gap region and halfway in the streamwise direction, were monitored to check the steady state solution. After attaining steady state solution the turbulence statistics was collected for three average flow turn over times, defined as streamwise length of the computational domain divided by V_{bulk}.

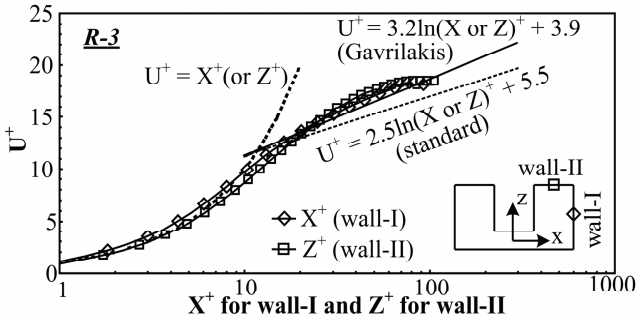

Figure 2-10: Calculated time averaged velocity distribution for two walls of channel 1 in the x and z direction at y = 0.0. Re_{ch}=2690

To check the quality of the near wall mesh resolution, the "law of the wall" relation was compared with the mean velocity profile along the x and z directions for channel-I at y = 0.0 (see Figure 2-10). Comparison shows that a good agreement exists in the viscous sub-layer, whereas in the logarithmic layer the results compares well with the modified law of the wall for a square duct proposed by Gavrilakis [34]. Hence, the mesh resolution sufficed to resolve the near wall velocity gradients.

2.4. Data processing

Several authors have proposed methods of extracting vortices from velocity fields based on the analysis of the local velocity gradient tensor (∇V) and its corresponding eigenvalues, see [35] for a summary of these methods. The studies have shown that the imaginary part of the complex eigenvalues of the velocity gradient tensor, denoted by λ_{ci}, is a useful indicator to localize the vortices in 2-D planes in 3-D flows. If the flow is a pure shear flow, particles would orbit in infinitely long ellipses and the orbit period (represented by $(\lambda_{ci})^{-1}$) would be infinite, corresponding to $\lambda_{ci} = 0$. Shorter, more circular ellipses (vortices) correspond to $\lambda_{ci} > 0$. Hence, the strength of any local swirling motion, representing the center of a vortex, can be quantified by the value of λ_{ci} [36]. For the present study, we choose λ^2_{ci} (s^{-2}), known as swirling strength, to quantify the strength of a swirling motion. To identify a vortex core, λ^2_{ci} is selected according to the criterion given in Equation (2-4):

$$\lambda^2_{ci} = \max\left(0, -\frac{1}{4} D_{dt}\right) \tag{2-4}$$

where D_{dt} is the discriminant of the characteristic equation of the 2D velocity gradient tensor.

The propagation velocity of the large-scale vortices in a flow field can be obtained by cross correlating the time-dependent velocity signals at two points (v_1 and v_2) separated by a streamwise distance of Δy_{12} [16]. The normalized cross correlation between two velocity signals is found using Equation (2-5):

$$C^R_{12}(\tau) = \frac{\sum_n v_1(t) \cdot v_2(t-\tau)}{\sqrt{\sum_n v_1^2(t) \cdot \sum_n v_2^2(t-\tau)}} \tag{2-5}$$

The time shift τ_{12} between the two signals is then estimated from Equation (2-6) as the value of the argument (τ) for which C^R_{12} in Equation (2-5) has a maximum value:

$$\tau_{12} = \arg_{\tau}\left[\max\left(C_{12}^{R}(\tau)\right)\right] \tag{2-6}$$

The vortex propagation velocity is calculated using a weighted average, as given in Equation (2-7):

$$v^{str} = \frac{\sum_{n}\left(C_{1n}^{R}\right)^{\alpha}\Delta y_{1n}}{\sum_{n}\left(C_{1n}^{R}\right)^{\alpha}\tau_{1n}} \tag{2-7}$$

with α=4 to give a high weighting factor to well correlated signals ($C\approx 1$).

2.5. Experimental results

This section presents the dependence of measured, time-averaged velocity profiles and large-scale coherent vortices characteristics on the Re_{ch}, gap spacing and gap shape. Before moving further, remind the coordinate system, x, y and z being the spanwise, axial and transverse directions, respectively. The corresponding x, y and z-velocity components are u, v and w, respectively. Table 2-3 shows the parameters used to calculate the Re_{ch}.

Table 2-3 Operational parameters for the three test sections

Test section	V_{bulk} range (cm/s)	D_h^{ch} (cm)	Re_{ch} range
R-3	4.1 – 41.3	2.42	1000 – 10,000
C-2	3.6 – 87.0	2.37	859 – 20,617
C-3	3.6 – 86.0	2.42	865 – 20,767

The large-scale vortices and the corresponding crossflow exist near/inside the narrow gap joining the two channels. In an attempt to correlate the gap related parameters with the channel parameters, we also investigated new definitions of gap Reynolds numbers ($Re_{g\text{-}app}$) for all three test sections. The $Re_{g\text{-}app}$ here is underestimated as compared to the true gap Reynolds number, because the velocity based on the total flow area of the gap region would be somewhat higher than the one approximated from the PIV measurements. Table 2-4 shows different combinations of near gap geometric and measured velocity scales used in defining $Re_{g\text{-}app}$.

Table 2-4 Geometric and velocity scales used in defining approximate gap Reynolds numbers

Scales	Re-I	Re-II	Re-III	Re-IV	Re-V	Re-VI	Re-VII	Re-VIII
Geometric	D_h^{gap}	D_h^{gap}	S	S	D	D	δ	δ
Velocity	v_{gap}^{avg}	Δv^{avg}	v_{gap}^{avg}	Δv^{avg}	v_{gap}^{avg}	Δv^{avg}	v_{gap}^{avg}	Δv^{avg}

where

D_h^{gap} = Gap hydraulic diameter. For C-2 and C-3, D_h^{gap} is calculated based on the flow area bounded by [D x (S+D/2)], see Figure 2-5
= 6.0 mm (R-3), 6.6 mm (C-2), 8.2 mm (C-3)

S = Gap spacing. For C-2 and C-3 minimum gap spacing
= 3.0 mm (R-3), 2.0 mm (C-2), 3.0 mm (C-3)

D = Gap depth
= 21.0 mm for R-3, C-2 and C-3

δ = Distance between the center of main channels, along x-axis
= 41.5 mm (R-3), 39.6 mm (C-2, C-3)

v_{gap}^{avg} = Time and space averaged streamwise velocity in the gap region that extends from x=±D/2

Δv^{avg} = Average of maxima and minima on the space and time averaged streamwise velocity profile (see § 2.5.2.).

All definitions of $Re_{g\text{-}app}$ are found to be a linear function of Re_{ch} for all three test sections, as shown in Figure 2-11. These trends suggest a linear dependence of the maximum velocity, in the channel region, and the minimum velocity, in the gap region, on V_{bulk}. Furthermore, from the Re-I trend we can conclude that up to Re_{ch}≈6000 laminar flow exist in the gap region for all three test sections since Re-I < 2000. These findings will be helpful during the modeling phase, Chapter 5. Based on these results, for the rest of the chapter we will present different measured and calculated quantities as a function of Re_{ch}.

2.5.1. Vortex visualization and identification

The flow field in the gap region is characterized by large-scale coherent vortices near both sides of the gap-channel interface. Some representative results are shown in Figures 2-12, 2-13 and 2-14 for the set up R-3, C-2 and C-3, respectively. Figure 2-12(a) shows three examples of such a field for R-3 with a time interval of 0.25s for Re_{ch}=2690.

The vortices in the flow field are made visible by subtracting the local, time-averaged velocity from the instantaneous velocity field. Several alternating rotating vortices can be observed, with their center regions (indicated by geometric shapes) approximately located near the left and right gap edges. The time difference between the frames is small enough to follow the individual vortices as they are being transported through the observation window. The width of the vortex partly covers the gap and partly the sub-channel region. An effort is also made to verify the center regions of the vortices by the method of swirling strength, described in §2.4. Figure 2-12(a) is reproduced in Figure 2-12(b) that shows the swirling strength times the vorticity, to indicate the direction

of rotation of the vortices. Figure 2-12(b) verifies the location of the vortices center region near ±D/2.

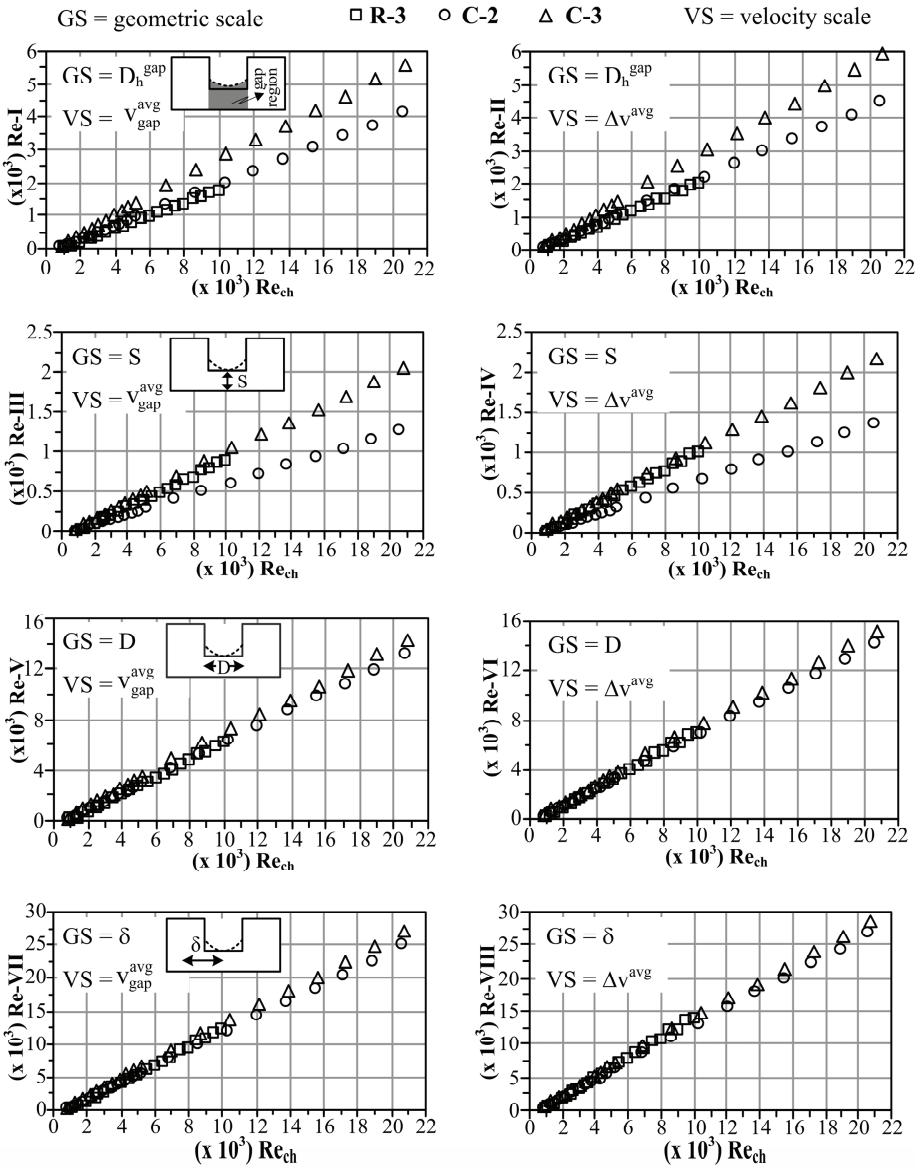

Figure 2-11: $Re_{g\text{-}app}$ as a function of Re_{ch} for different combinations of near gap geometric and velocity scales.

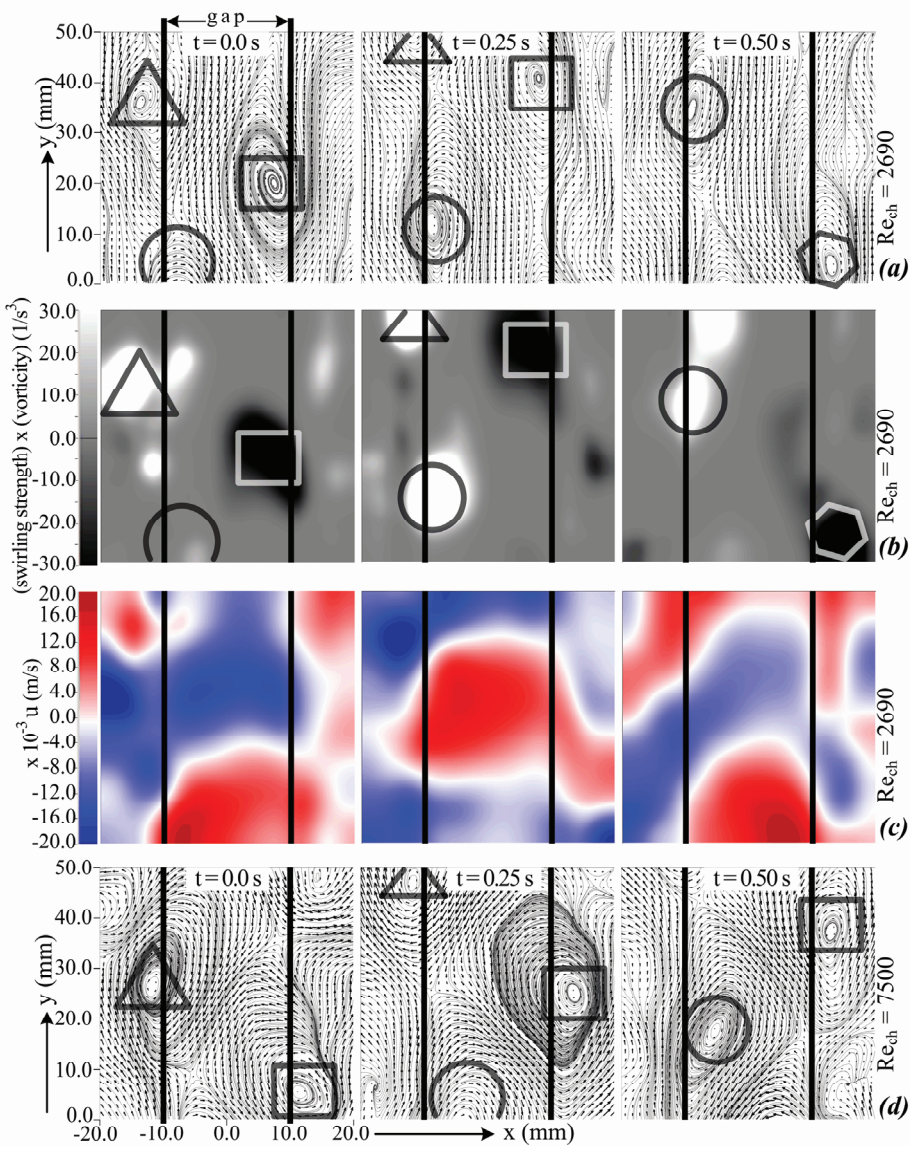

Figure 2-12: Measured fluid flow field relative to the average fluid velocity for R-3 at (a) Re_{ch}=2690 and (d) Re_{ch}=7500, (b) Measured swirling strength multiplied by vorticity identifying vortex cores at Re_{ch}=2690, (c) crossflow zones Re_{ch}=2690. Geometric shapes trace the center regions of the vortices.

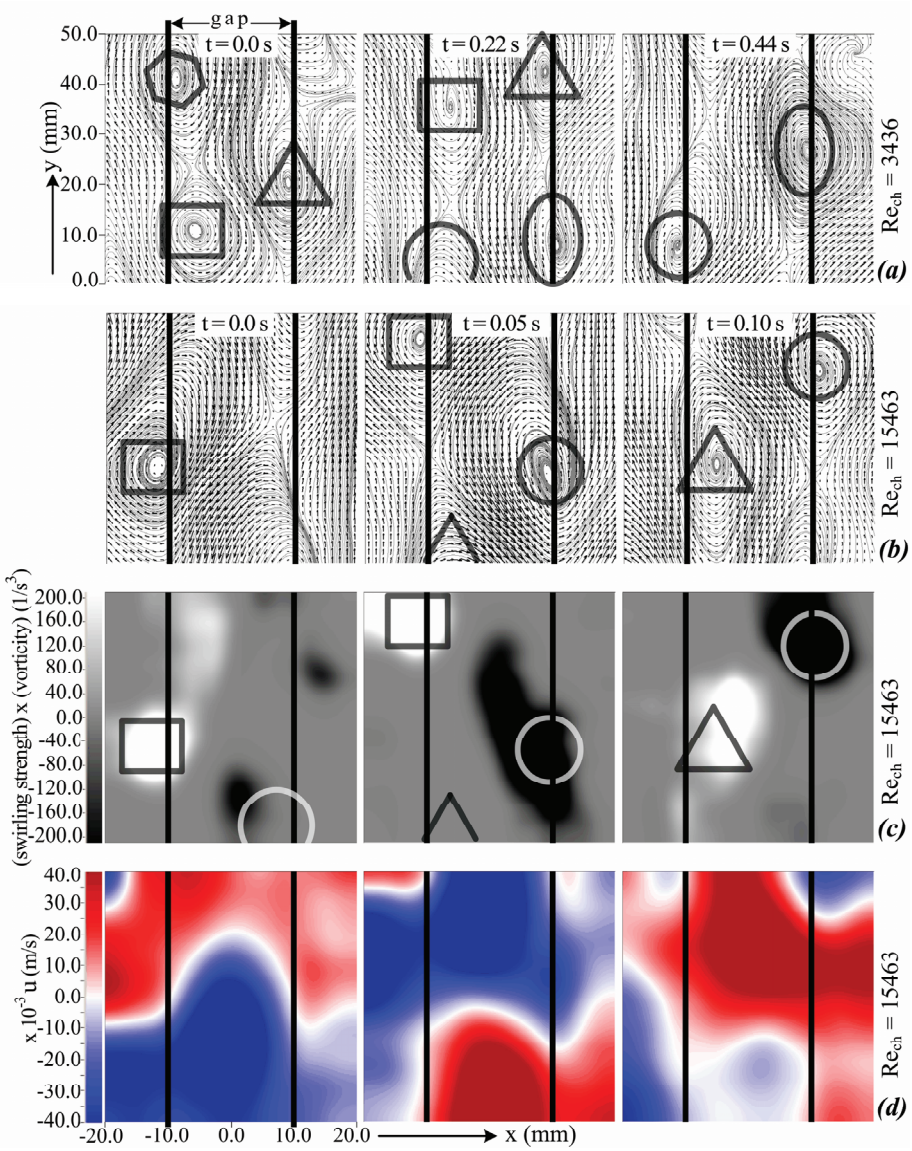

Figure 2-13: Measured fluid flow field relative to the average fluid velocity for C-2 at (a) Re_{ch}=3436 and (b) Re_{ch}=15463, (c) Measured swirling strength multiplied by vorticity identifying vortex cores at Re_{ch}=15463, (d) crossflow zones at Re_{ch}=15463. Geometric shapes trace vortices center region.

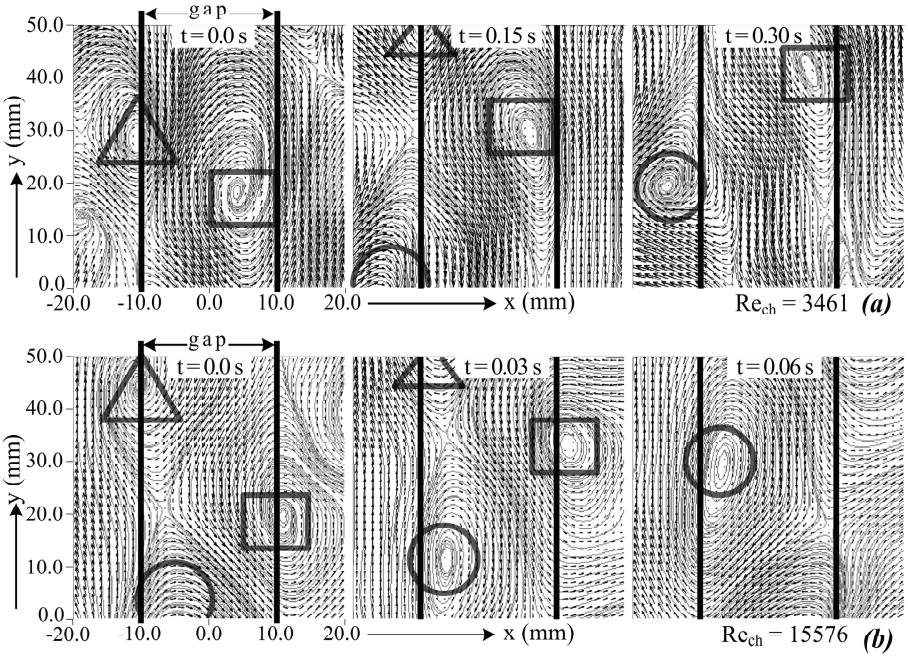

Figure 2-14: Measured fluid flow field relative to the average fluid velocity for C-3 at (a) Re_{ch}=3461 and (b) Re_{ch}=15576. Geometric shapes trace vortices center region.

The vortices, shown in Figure 2-12(a), result in alternating crossflow zones spanning over the full length of the gap, see Figure 2-12 (c). The red or blue color indicates the magnitude and direction of the fluid velocity in the gap parallel (x) direction; the darker the color, the larger the velocity magnitude. Comparison of the three frames in Figure 2-12(c) also suggests the transport of crossflow zones in the streamwise direction without any major distortions. This leads to the conclusion that the vortices retain their identity while moving in the streamwise direction. Figure 2-12(d) depicts the coherent vortices for R-3 at Re_{ch}=7500. Comparison of Figure 2-12(a) and Figure 2-12(d) reveals an important difference between the flow pattern in the gap region at Re_{ch}=2,690 and Re_{ch}=7,500: at higher Re_{ch}, streamlines extend from one channel to the other. We expect that this might lead to higher mass transfer rates (further examined in Chapter 4). Flow patterns for C-2 and C-3 are presented in Figures 2-13(a)-(d) and Figures 2-14(a)-(b), respectively. Similar visual behavior, as explained above for R-3, can be observed from these figures at low and high Re_{ch}.

The measurements have shown the existence of near gap large-scale coherent vortices with their center regions close to ±D/2. These vortices results in periodic cross

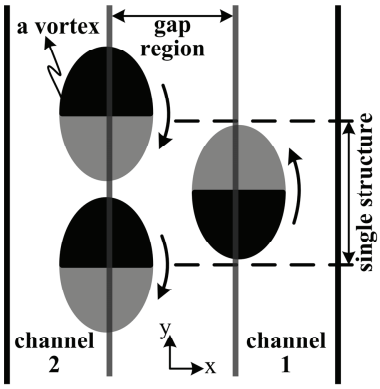

Figure 2-15: Definition of a structure. Black and grey color indicates the fluid movement from left to right and right to left, respectively

flow zones in the gap region, transported in the streamwise direction, for R-3, C-2 and C-3 for the range of Re_{ch} given in Table 2-3. An interesting finding is the location of the center regions of the vortices near ±D/2 for rectangular (R-3) as well as curved gap geometry (C-2 and C-3). This shows that the vortices are located independent of the gap geometry. Based on these observations we define a single flow structure given by two consecutive crossflow zones, one in each direction. In Figure 2-12(c) and Figure 2-13(d), a red zone and adjacent blue zone represent a structure element. In other words, a structure element consists of a pair of vortices located on either side of the gap-channel interface. Figure 2-15 shows the conceptual picture of a structure.

2.5.2. Fluid and structure propagation velocity profiles

The propagation velocity of the flow structures is obtained by cross correlating the time-dependent velocity signals (u and v) at two points separated by a streamwise distance of Δy_{12}=2.0 cm, as given in §2.4. The time shift τ is found to be a linear function of the streamwise distance between the two monitoring points. An example of measured cross and streamwise velocities, for Re_{ch}=2690 (R-3), is presented in Figures 2-16(a) and 2-16(b), respectively. The lines in the graph give the output of 3x3x3 point (x, y, t) median filtered velocities. In both these figures, the velocity signals at the two points differ by a time shift of about 0.25 s.

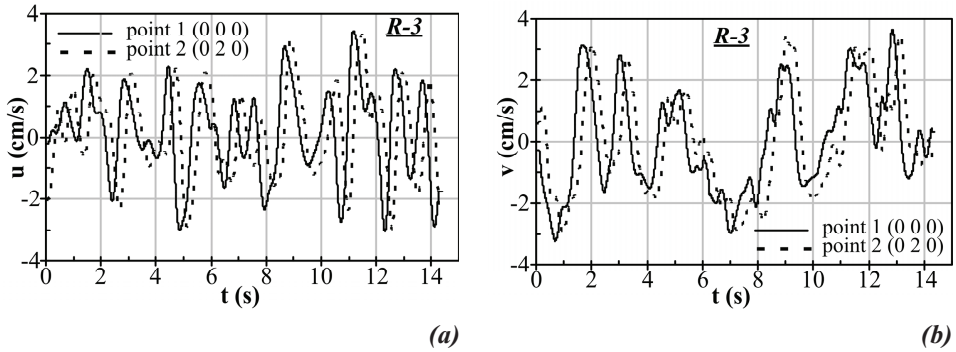

Figure 2-16: Measured velocity signal at two points at the center of the gap. Point 1 is 2 cm upstream of point 2. (a) x/spanwise component, (b) y/streamwise component displayed as ($v-v^{avg}$). Re_{ch}=2690.

In Figure 2-17, the normalized streamwise average fluid velocity (v^{avg}) and the structure propagation velocity (v^{str}) for R-3, C-2 and C-3 are shown. The Re_{ch} selected for each case are the same as used for visualization examples of the coherent structures, §2.5.1. The abscissa is the distance on a line passing through the origin in the x-direction, see Figure 2-17(d), and the ordinate shows the streamwise velocities, normalized to the gap depth (D) and the V_{bulk}, respectively. The fluid velocity is averaged in time and space for 0<y<5 cm. The structure propagation velocity is found according to the method mentioned in the preceding paragraph. The difference between the velocities of both the channels in Figures 2-17(a)-(c) could be due to the non-uniform inlet flow conditions, uncertainty in the positioning of the PIV measurement plane at exactly z=0 and the inherent geometric irregularities of the test sections. The profound difference in channel velocities for R-3 is mainly due to the use of one inlet, since shifting to two inlets for C-2 and C-3 shows a significant improvement in the channels flow symmetry.

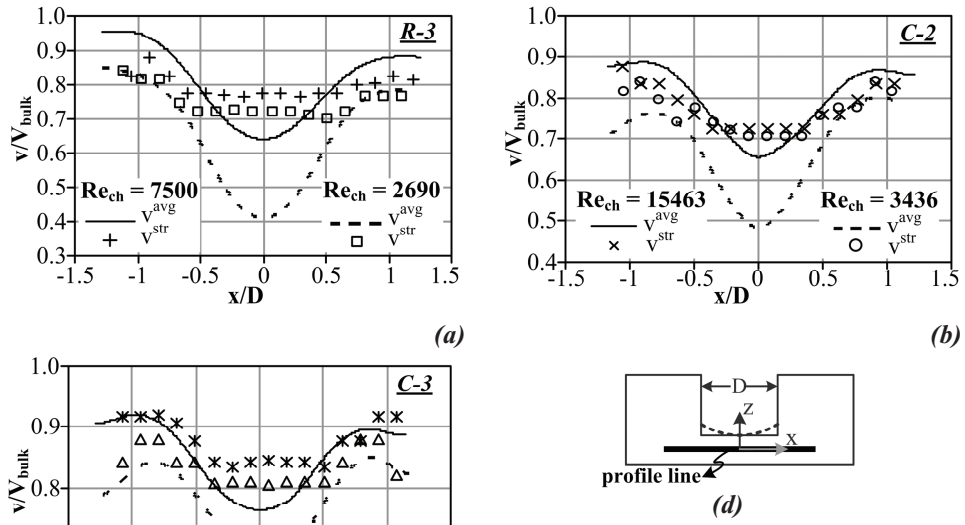

Figure 2-17: Streamwise fluid and structure velocity profile, averaged over time and y for (a) R-3, (b) C-2, (c) C-3, (d) location of profile measuring line.

Because all measurements were performed as close as z=1.0 mm from the near gap main outer wall (wall-B), at all positions the time averaged fluid velocity in Figure 2-17 is smaller than the V_{bulk}. The origin of large-scale coherent structures, Figures 2-12, 2-13, 2-14, could be understood from the streamwise fluid velocity profile. The points of the lowest and highest fluid velocities are located approximately at the gap and the channel mid

points, respectively. From the origin to x/D ≈ ± 1.0, the time averaged fluid velocity profile resembles a typical mixing layer profile. Two distinct regions can be identified: a low flow zone in the gap region, between x/D ≈ ±0.5 and a high flow zone extending beyond x/D = ±0.5 approximately up to the center of the channel (x/D ≈ ±1.0). The shear layer originates when two streams of different relative velocities first meet at a location upstream within the test section. Introduction of small instabilities at this stage result in unsteady developing waves. These waves cause a rollup of fluid, resulting in discrete vortices. These vortices further interact, by the process of rolling, to form a single large vortical structure [37].

The structure propagation velocity in Figures 2-17 is almost constant in the gap. As we move towards the main channel regions, the structure propagation velocity slightly increases towards higher values, being comparable to the streamwise fluid velocity. As suggested in § 2.5.1., constant structure propagation velocity in the gap region also confirms that the structures in the streamwise direction are preserved. Note that the structure propagation velocity is higher than the velocity of the fluid in the gap. Remind that the structures as defined here are not material structures. In fact, these structures symbolize a traveling wave influencing the transfer of momentum and matter in the gap region. The sub-channels streamwise fluid flow mainly influences the streamwise movement of the vortices and hence the streamwise structure propagation velocity in the gap region can be higher than the gap fluid velocity.

2.5.3. Dependence of flow and structure characteristics on Re_{ch}

In this section, we will have a look at the variation of the fluid and structure characteristics as a function of Re_{ch} for each test section. Figure 2-18 shows the span wise positions, in the z=0-plane, where the time-averaged streamwise fluid velocity profile has maxima, minima and points of inflection ($\partial^2 v/\partial x^2=0$). On a curve comprising of upper and lower concave segments, the inflection point is a turning point between these two parts. In our case, the inflection points in Figure 2-17 represent the shift from a low flow region to a high flow region.

From the trend of Re-I vs. Re_{ch}, see Figure 2-11, we can approximately classify the flow regimes in the gap and the channel region, as shown in Table 2-5. Keeping in view this classification, Figures 2-18 depicts that the change in the shape of the streamwise velocity profile is dependent on the flow condition in the channel region. For all cases, the point of minimum velocity is located at the centre of the gap (i.e., x=y=z=0).

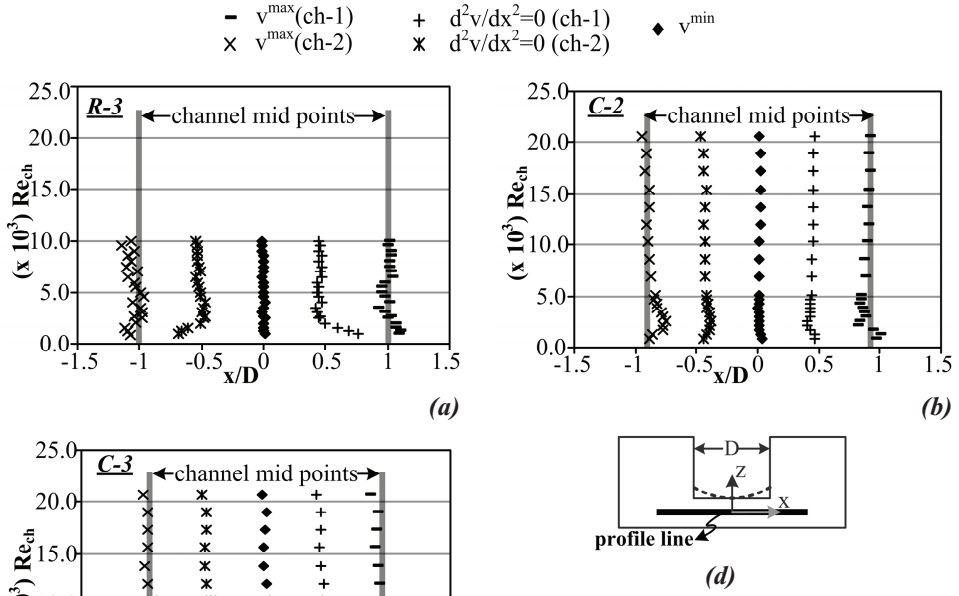

Figure 2-18: Change in the shape of the velocity profile with Re_{ch}. The position where the time averaged velocity profile has the highest and the lowest value and points of inflection are displayed for (a) R-3, (b) C-2, (c) C-3, (d) profile line.

Table 2-5 Flow regimes in the channel and the gap region deduced from the channel (Re_{ch}) and the approximate gap (Re-I) Reynolds numbers.

Re_{ch}	Re-I	Channel region	Gap region
$Re_{ch} \leq 2000$	Re-I < 2000	laminar	laminar
$2000 < Re_{ch} \leq 4000$	Re-I < 2000	transition	laminar
$Re_{ch} > 4000$	Re-I < 2000	turbulent	laminar

$Re_{ch} \leq 2000$

For R-3, see Figure 2-18(a), the location of the maximum and the inflection points show a shift away from the origin. This shows an extension of the laminar flow zone in the gap region towards the channel. The laminar velocity profile in the channel region is the most probable cause of this extension. In a curved gap geometry (C-2 and C-3), it is difficult to define a gap-channel interface since there is no sharp, well-defined boundary, as we have in the case of a rectangular gap. The choice of a gap-channel interface location, at

±D/2, is therefore a bit arbitrary. Nevertheless, due to curvature of the gap, we would expect the main channel fluid extending further into the gap region for C-2 and C-3 as compared to R-3. This effect is apparent in Figure 2-18 (b) and (c) as a shift in the maxima and inflection points towards the origin is found, for Re_{ch}<2000.

2000 < Re_{ch} ≤ 4000

With the increase of the Re_{ch} turbulent flow approaches in the channel region, resulting in the flattening of the velocity profile and steepening of the streamwise velocity in the direction perpendicular to the near gap outer wall-B. This causes the corresponding shift of the maxima and the inflection points towards x/D≈±1.0 and x/D≈±0.5, respectively, for all test sections.

Re_{ch} > 4000

Figure 2-18 shows that for turbulent channel flow, Re_{ch}>4000, the shape of the streamwise velocity profile become independent of Reynolds numbers for all the test sections. This shows that, for Re_{ch}>4000, the curvature of the duct G, in C-2 and C-3, has no influence on the shape of the near-gap streamwise velocity profile, since it follows the same trend as found for a rectangular gap, R-3. Keeping in view the distance of the PIV measurement plane from the near-gap outer wall, 1.5 mm for S=3.0 mm and 1.0 mm for S=2.0 mm, probably the gap depth and the near-gap outer wall-B have a dominant influence on the trend of the streamwise velocity profile rather than the shape of the duct wall, facing the gap. Furthermore, comparing Figures 2-12, 2-13. 2-14 with Figures 2-18, the location of the center regions of the coherent vortices matches the location of the inflection points, particularly for higher Re_{ch}.

In Figure 2-19, the magnitude of the time averaged velocities at the points of maxima (v^{max}), minima (v^{min}) and inflection ($v^{inflec.pt.}$) are reported. Figure 2-19 also shows the structure propagation velocity (v^{str}) averaged along x/D=±1 and the mean of v^{max} and v^{min} (v^{avg}). All values are non-dimensionalized by V_{bulk}. At all conditions, the velocity profile qualitatively resembled the profile presented in Figure 2-17, although quantitatively the fluid velocity inside and outside of the gap differs considerably. For Re_{ch}>5000 all the velocities linearly scale with the V_{bulk} (and thus with Re_{ch}). For all Re_{ch}, $v^{inflec.pt.}$ is almost the same as v^{avg}. For Re_{ch}>5000 v^{str} approaches $v^{inflec.pt.}$, and in turn v^{avg}. Although R-3 and C-3 have the same S/D, the velocities for R-3 and C-2, presented in Figure 2-19, are in better agreement. The agreement of near gap velocities for R-3 and C-2 is probably due to the influence of the gap hydraulic diameter, which is comparable for the R-3 and C-2, see Table 2-3.

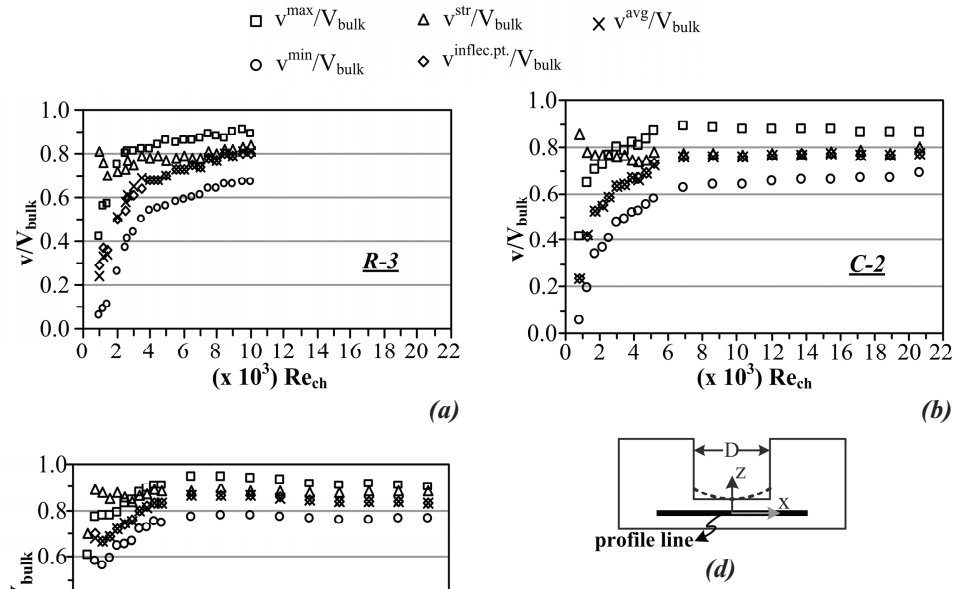

Figure 2-19: Change of the shape of the velocity profile as a function of Re_{ch}. The highest and lowest velocity, the structure propagation velocity and the velocity at the point of inflection normalized by V_{bulk} are presented for (a) R-3, (b) C-2, (c) C-3, (d) profile line.

The standard deviation of the velocity pulsations in the span wise and the streamwise directions in the channel (x/D=±1, y/D=z/D=0) and in the gap region (x/D=y/D=z/D=0), are shown in Figure 2-20 as a percentage of V_{bulk}. The velocity pulsations in the span wise direction in the gap region (u^{rms}) are of particular interest since these are a measure of crossflow. At Re_{ch} less than 2000, the normalized cross velocity pulsations in the gap are small, indicating the presence of weak crossflow. With increasing Re_{ch}, the normalized velocity pulsations increase to a maximum at Re_{ch}=2500, and then decrease to almost a constant value. From Figure 2-20 we can conclude that for Re>6000 the crossflow linearly scales with the V_{bulk} and in turn with the Re_{ch}. An interesting thing to note is that (u^{rms}/V_{bulk}) for C-2 are distinctly higher than for R-3 and C-3 for all Re_{ch}. This finding suggests that higher crossflows exists for smaller gap spacings. Although, we also know that as gap spacing approaches zero, the crossflow must get lower again. Apparently there is a gap spacing at which the crossflow is maximum (further discussed in Chapter-4).

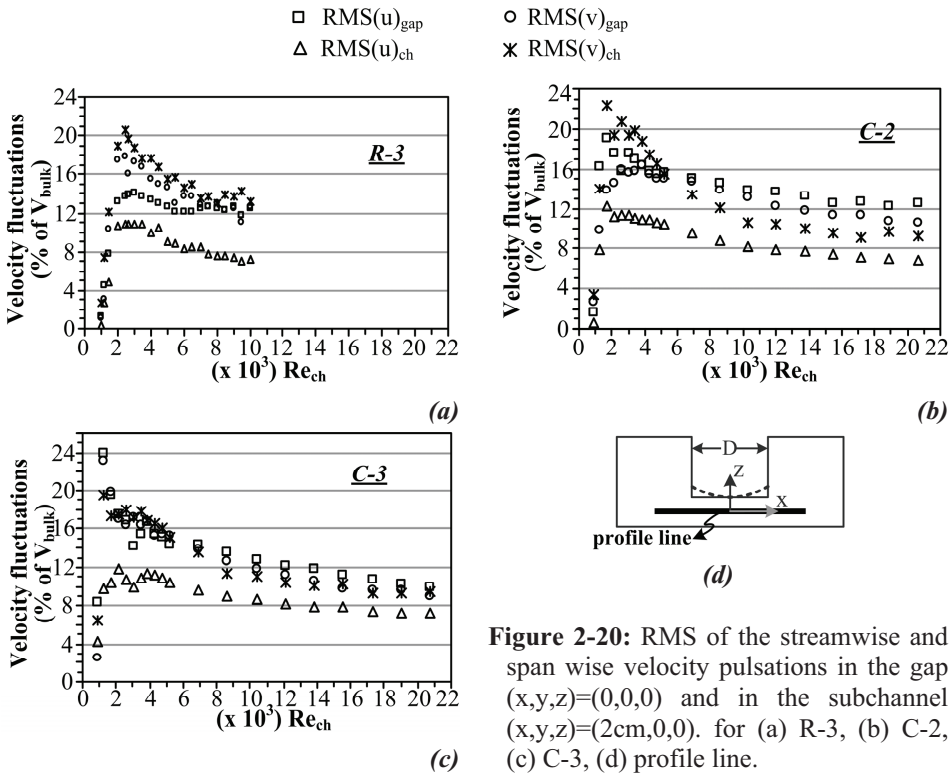

Figure 2-20: RMS of the streamwise and span wise velocity pulsations in the gap (x,y,z)=(0,0,0) and in the subchannel (x,y,z)=(2cm,0,0). for (a) R-3, (b) C-2, (c) C-3, (d) profile line.

A single structure element consists of two crossflow zones, as defined in §2.5.1. In Figure 2-12(c) and 2-13(d), the white lines, indicating u=0, separates the two consecutive crossflow zones. The streamwise length of a structure can be estimated from the time between the passing of two zones of zero crossflow (the white lines in Figure 2-12(c) and 2-13(d)) and using Equation (2-8):

$$L^{str} = v^{str}.2\overline{\Delta t}_{u=0} \qquad (2\text{-}8)$$

The streamwise structure length is measured at different points along the x-axis in the measurement plane. At any given Re_{ch}, the streamwise structure length at a particular location varies, and two consecutive structures can easily differ in length by a factor of two. The average streamwise structure length at one location is determined by averaging the streamwise length of all observed structures during the flow measurement time. The streamwise structure length averaged along x=±D/2 at 8 monitoring points for a particular Re_{ch} is presented in Figure 2-21 for the three test sections. Large coherent structures of at least 17 times larger than the gap depth have been observed at Re_{ch}=1000. With increasing Reynolds numbers the streamwise structure length decreases up to Re_{ch}≈2000, above which

the average streamwise structure length is almost constant. The constant streamwise structure length is approximately 7.3 cm, 7.2 cm and 9.0 cm for R-3, C-2 and C-3, respectively.

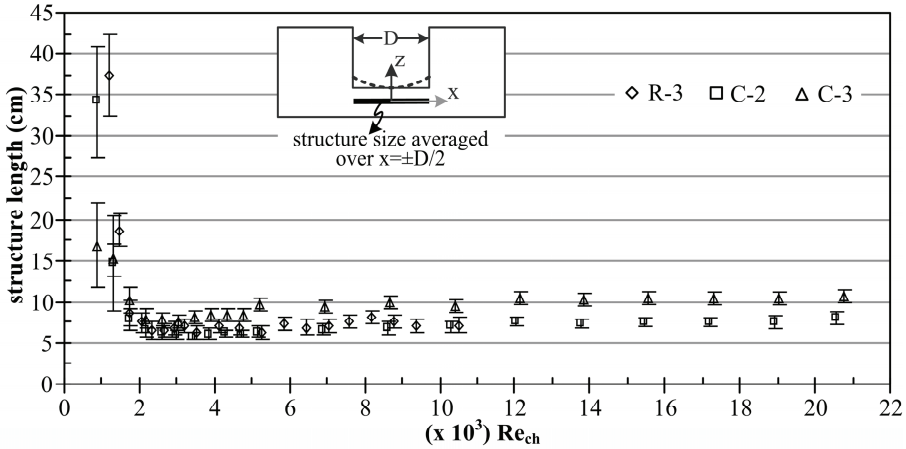

Figure 2-21: Average streamwise structure length vs. Re_{ch} for (a) R-3, (b) C-2, (c) C-3.

Keeping in view the mixing layer concept, the source of the coherent structures is the streamwise velocity difference ($\Delta v = v^{max} - v^{min}$) between two parallel adjacent flow streams. Figure 2-22(a) and (b) shows a plot of absolute values of Δv and u^{rms} in thegap region, respectively, for the test sections R-3, C-2, C-3 as a function of Re_{ch}. The dependency of Δv on D_h^{gap} is apparent since Δv decreases with increasing D_h^{gap}.

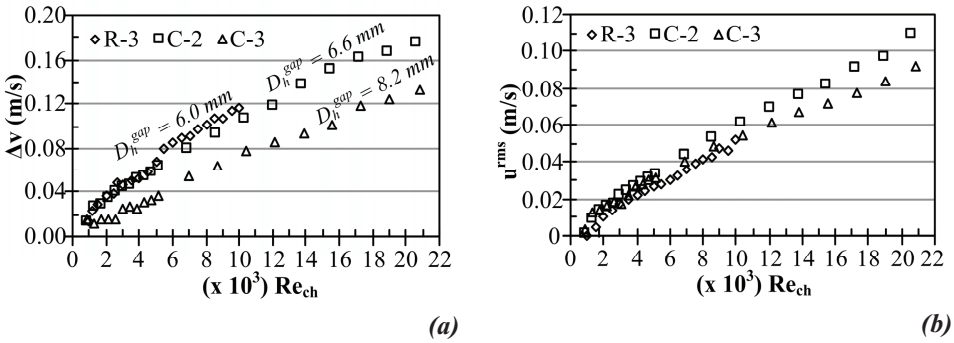

Figure 2-22: Absolute values of (a).Δv and (b) u^{rms} in the gap region for test section R-3, C-2 and C-3 as a function of Re_{ch}.

Comparison of Figures 2-19(a) and (c) reveals that the decrease in Δv for test sections with same PIV plane location, i.e., R-3 and C-3, is mainly due to the gap geometry since normalized v^{max} has comparable values whereas v^{min} is significantly higher for C-3. By comparing Figures 2-21 and 2-22(a), it can be concluded that, for each Re_{ch}, a decrease

in Δv (due to an increase in S/D_h^{gap}) results in a relatively large streamwise structure length. Furthermore, comparison of Figures 2-21 and Figure 2-22(b) shows that for each Re_{ch} low and high values of u^{rms} are associated with relatively large and small streamwise structure lengths, respectively. An additional study carried out over a broader range of S/D^h_{gap}, presented in Chapter 4, also verified these conclusions. From comparison of Figures 2-21 and 2-22 the above-mentioned conclusions are also valid for $Re_{ch} \leq 2000$, for a fixed S, i.e., in a single test section. For $Re_{ch} > 2000$, Δv and u^{rms} increases but the streamwise structure length becomes almost constant, i.e., independent of V_{bulk} and probably becomes a function of gap geometry only. This finding is consistent with the experimental results of Meyer and Rehme [14].

A typical plane mixing layer belongs to a category of free shear flows, i.e., there is no influence of a wall. The downstream evolution of a free mixing layer is characterized by an increase in the spanwise width of the layer. The dimensions of the coherent structures in free mixing layers are consistent with this width [38]. Therefore, the downstream spanwise spreading of the layer corresponds to the growth rate of the large-scale structures. The compound channels although exhibit a mixing layer type streamwise velocity profile but it belongs to the wall bounded shear flow category rather than a free shear flow. It appears that in compound channels, although the origin of the structures is similar to the one in a mixing layer, but at a certain flow threshold ($Re_{ch} \approx 2000$ in present cases), the mixing layer width becomes constant, resulting in a constant streamwise structure length. Meyer and Rehme [14] used gap depth (D) as a possible geometric parameter to define the constant streamwise structure length. From the present study, however, the effect of S on the streamwise structure length is apparent (Figure 2-21). Both findings seems to indicate that D_h^{gap} is a more appropriate geometric parameter since the effect of both S and D are included in D_h^{gap}.

2.6. Numerical Results

In this section LES results will be presented for R-3 at $Re_{ch} = 2690$. The major aim is to look at the shear layer properties, existing near $x = \pm D/2$, being the channel-gap interface. Additionally, the secondary flows near the gap region and their contribution to crossflow are also investigated. Figure 2-23(a) shows the calculated crossflow zones similar to the measured one shown in Figures 2-12(c) and 2-13(d), indicative of the existence of large-scale coherent structures. The calculated and measured structure propagation velocity and the streamwise fluid velocity, similar to the Figure 2-17(a), are compared in Figure 2-23(b). Qualitatively the computed profile resembles very well the measurements. The quantitative difference could be due to insufficient statistical data collection from the computations. The

profile shift at the origin and a slight distortion at the middle of the channel also show the need for further collection of statistical data for calculations. Another plausible reason could be the sensitivity of the measured profile to the positioning of the PIV measurement plane along the z-axis, as discussed in § 2.5.2.

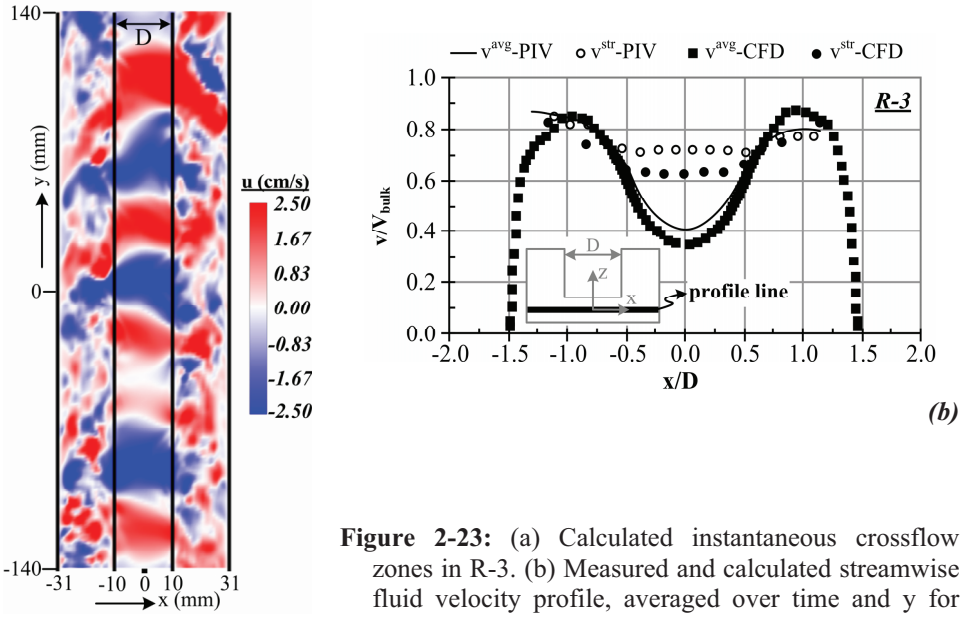

Figure 2-23: (a) Calculated instantaneous crossflow zones in R-3. (b) Measured and calculated streamwise fluid velocity profile, averaged over time and y for R-3. Re_{ch}=2690.

The computed time-averaged streamwise velocity profile along the line extending from z=±1.5 mm and passing through the origin is shown in Figure 2-24. The parabolic shape of the profile indicates the existence of laminar flow in the gap region.

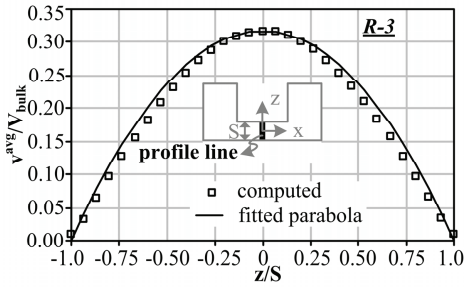

Figure 2-24: Computed streamwise-time-averaged velocity profile in the gap, at origin along the z direction for R-3. Re_{ch}=2690.

Figure 2-25(a) shows the measured and calculated time averaged turbulence intensities in the streamwise and the lateral direction. Figure 2-25(b), 2-25(c) and 2-25(d) present the contours of calculated turbulence intensities. Figures 2-25(a) shows that the maximum streamwise turbulence intensities occur at x/D ≈ ± 0.5, the gap-channel interface, and decrease to a minimum towards the gap center, whereas the gap parallel (x-direction) turbulence intensities have a maximum value at x/D ≈ ± 0.4 and remain nearly constant within the gap. The calculated contours in Figure 2-25(b), 2-25(c) and 2-25(d) show

turbulence intensities in the xz-plane which are missing in the experimental results. It is shown that the maximum, for all directions, is located at or near the gap-channel interface region. This also implies that the maxima of turbulent kinetic energy are also located near the gap region.

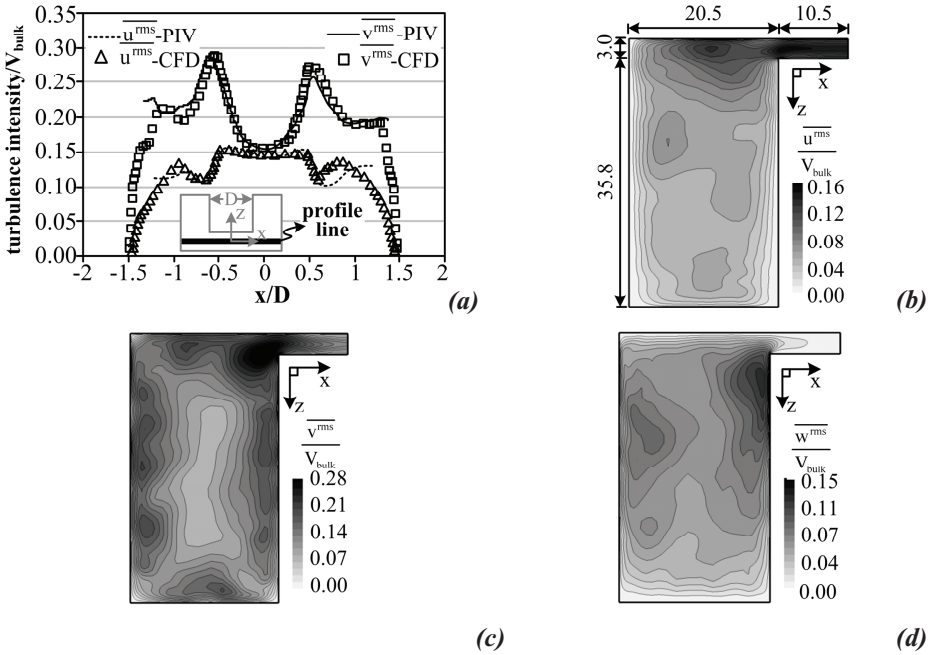

Figure 2-25: Turbulence intensities quantified as RMS values of the velocities and normalized by the V_{bulk}. (a) Measured and computed profiles along the x-axis at the origin. Computed contours in the xz-plane at the origin, (b) gap parallel/x-direction, (c) streamwise/y-direction, (d) transverse/z-direction. Re=2690.

The normalized Re shear stresses are presented in Figure 2-26(a) to 2-26(d). For 2D measurements, the peak value of $\overline{u'v'}$ occurs at the gap-channel interface, Figure 2-26(a). The measured contour profiles, Figure 2-26(b), 2-26(c) and 2-26(d), depicts that the maximum of $\overline{u'v'}$, $\overline{u'w'}$ and $\overline{v'w'}$ are located near the gap-channel interface as well. Quantitatively the measured and calculated results also show a good agreement. These results confirm the existence of a shear layer at x=±D/2, the channel-gap interface.

Although the gap region has been identified as a laminar zone, see Figure 2-24, still normal and shear stresses are eminent in this region from Figures 2-25 and 2-26, respectively. The normal and shear stresses shown in these figures are based on double

decomposition of the instantaneous velocity field. A fluctuating velocity signal j can be decomposed according to Equation (2-9):

$$j(x, t) = J + j'(x, t) \tag{2-9}$$

where J is the ensemble averaged and j'(x, t) the fluctuating part. The fluctuating part here consists of contributions from both the coherent and incoherent structures. To recognize the individual contributions from coherent and incoherent structures, j'(x, t) can be further divided in a coherent part j_c' related to the coherent structures and an incoherent part j_r' associated with the random turbulences, the so-called triple decomposition:

$$j(x, t) = J + j_c'(x, t) + j_r'(x, t) \tag{2-10}$$

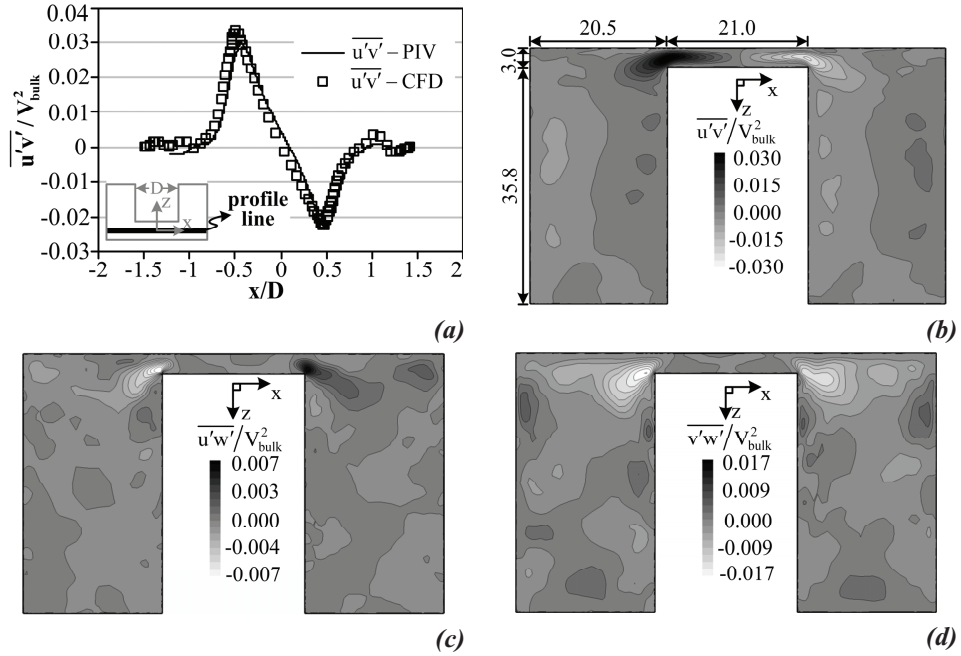

Figure 2-26: Re shear stresses normalized by the V_{bulk}, (a) Measured and computed profile along x-axis at the origin. Computed contours in the xz-plane at origin, (b) $\overline{u'v'}$, (c) $\overline{u'w'}$, (d) $\overline{v'w'}$. Re_{ch}=2690

The triple decomposition of experimental or numerical flow data can be performed by using e.g., (i) phase averaging methods, (ii) turbulence filtering [39], (iii) wavelet decomposition [40], or (iv) Proper Orthogonal Decomposition (POD) [41]. Here, we apply the POD filtering technique on measured data, for R-3 at Re_{ch}=2690, to show that the coherent structures are the major contributor towards the normal and shear stresses shown in Figures 2-25 and 2-26, respectively. The Proper Orthogonal Decomposition provides a

mathematically rigorous procedure for extracting the most energetic modes from a fluctuating velocity field that define the coherent structure of the flow. Based on energy considerations, the POD captures the most energetic and hence largest structures of the flow in the first modes. Using this concept, we can define a cut off mode number separating the contribution of both coherent and incoherent velocity fields. In next step, each fluctuating velocity field is reconstructed using the corresponding modes. From these velocity fields we can then estimate the individual contributions of coherent and incoherent parts to the normal and shear stresses.

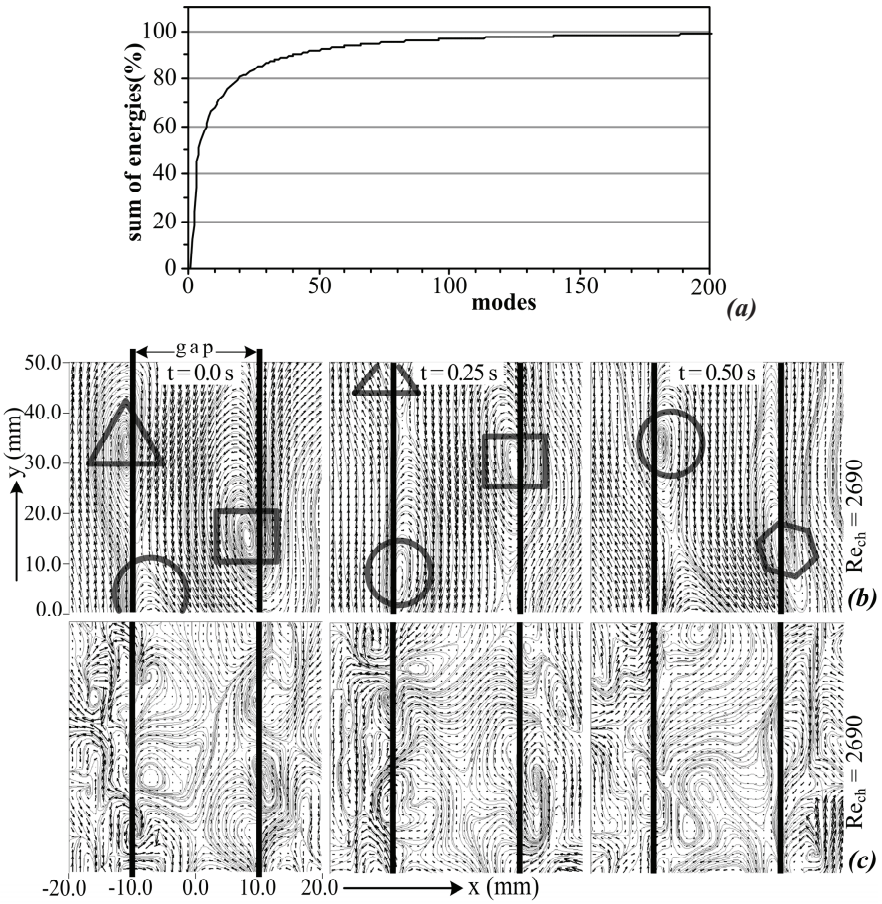

Figure 2-27: (a) POD energy convergence, (b) reconstructed velocity field from the first five modes, representing the coherent part of the flow field, (c) the residual/incoherent part of the flow field.

The POD energy convergence is shown in Figure 2-27(a). The five first POD modes contain more than 50% of the fluctuating kinetic energy. Although detailed methods are

reported to select the cut-off mode number [42], for this study we have assumed the cut-off POD number at five. The coherent velocity field is then reconstructed from the first five POD modes and the remaining POD modes are used to provide the incoherent background velocity field. Figure 2-27(b) and (c) shows these reconstructed velocity fields for the same frames as depicted in Figure 2-12(a). Comparison of Figures 2-27(b) and 2-12(a) confirms that large-scale coherent structures can be extracted from the first five POD modes.

Figure 2-28 shows the contributions of the coherent and incoherent normal and shear stresses along with the corresponding Reynolds averaged stresses. In the gap region coherent normal stresses dominate over the incoherent stresses, see Figure 2-28 (a) and (b). However, the incoherent normal stresses approach the Reynolds averaged stresses as we move from the gap towards the main channel, indicating a transition from a laminar to a turbulent region. The shear stress, $\overline{u'v'}$, appears to be fully dominated by the coherent component of the velocity pulsations, see Figure 2-28(c). With the help of the POD analysis we have shown that the gap region of R-3, at Re_{ch}=2690, is essentially a laminar zone. The existence of normal and shear stresses in the gap region is due to the coherent part of the velocity pulsations rather than the incoherent/turbulent part.

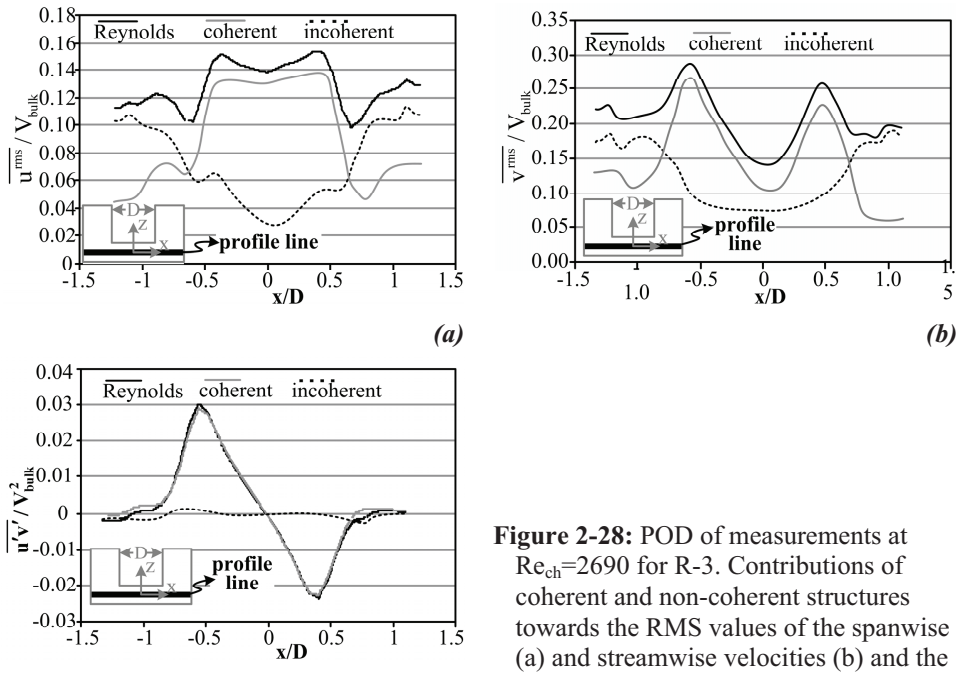

Figure 2-28: POD of measurements at Re_{ch}=2690 for R-3. Contributions of coherent and non-coherent structures towards the RMS values of the spanwise (a) and streamwise velocities (b) and the shear stress (c), normalized by V_{bulk}.

Figure 2-29(a) and 2-29(b) present computed contours of the time averaged axial velocity contours and vectors of the secondary flows, in the xz-plane, respectively. The skewness in the mean velocity contours near the channel edges and center is due to the characteristic secondary flows for a rectangular duct. Additionally the secondary flow existence near the channel-gap interface is also visible. These secondary flows are expected to contribute towards the flow mixing in the sub-channels. Quantitatively, however, the secondary flow is approximately 2.5% of the V_{bulk}, whereas the cross velocity pulsations in the gap region are nearly 13% of the V_{bulk}.

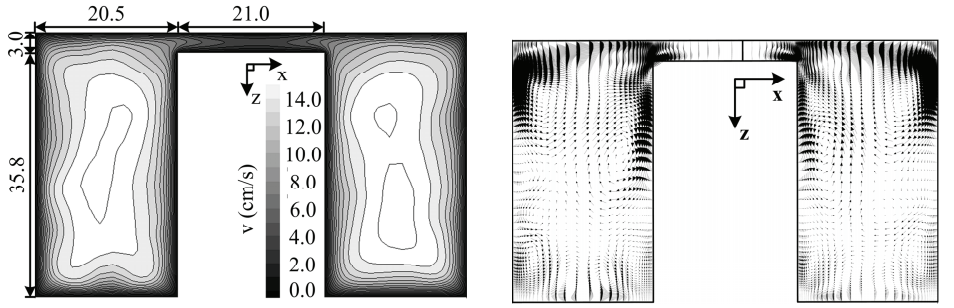

Figure 2-29: (a) Mean axial velocity contours normalized with V_{bulk}, (b) secondary flows in the xz-plane at origin. Re=2690.

From numerical results, we can conclude that the distributions of the turbulent intensities and the shear stresses near the gap region are incompatible with the sole effects of secondary flows. In fact, the present simulations show no evidence of strong secondary flows near the gap region and the turbulent intensities and the shear stresses near the gap region are primarily due to the presence coherent structures.

2.7. Conclusions

The velocity field in the near wall, rectangular and curved gap region of a setup, representing two interconnected subchannels of a vertical tube bundle geometry, has been studied. Two gap spacing of 2.0 mm and 3.0 mm are considered for a curved gap region. Experiments have been performed by using 2D-PIV for full range of Reynolds numbers. Large Eddy Simulation at Re=2690 have also been carried out, thereby using periodic boundary conditions along the streamwise direction to extend the study to the third dimension. This study leads to the following conclusions:

- Counter rotating vortices at both sides of the channel-gap interface have been identified. These vortices results in periodic crossflow zones in the gap region. The

crossflow zones are transported in the streamwise direction retaining their identity. A structure element consisting of two periodic crossflow zones has been defined. These structures occur for laminar, transitional and turbulent flow regimes.

- The time averaged velocity profile resembles a typical mixing layer profile showing a region of low (gap) and high (subchannels) velocities. The coherent structures are likely due to the strong mean velocity differences between the channel and the gap region for full range of Re_{ch}.
- The change in the shape of the streamwise velocity profile is observed with changing gap geometry for laminar flow regime ($Re_{ch}<2000$).
- For turbulent flow, $Re_{ch}>4000$, the location of the maxima, the minima and the inflection point of the mean streamwise velocity profile become independent of Re_{ch} irrespective of the gap geometry. This shows the dominant effect of the gap depth and the near gap main outer wall-B on the velocity profile rather than the shape of the gap. The application of these results to two inter-connected sub-channels of a tube bundle needs further considerations due to non-existence of any near gap plane wall in such geometry.
- Large-scale coherent structures are identified as major contributor towards the span wise velocity pulsations in the gap, even in the presence of a laminar flow gap region. It is anticipated that these coherent structures have a dominant role in the inter-channel crossflow mixing. Furthermore, a decrease in the gap spacing results in higher values of span wise velocity pulsations, indicating higher inter-channel mass transfer rate for smaller gap spacings.
- For $Re_{ch}>5000$ the structures propagation velocity is found to have a value equal to the mean of the maximum and minimum streamwise velocities in the channel and the gap region, respectively. The maximum and minimum streamwise velocities seem to be function of gap hydraulic diameter.
- The instantaneous cross velocity pulsations resulting from counter rotating vortices at gap-channel interface, being nearly 13% of the V_{bulk}, dominate over the secondary flow.

3

Flow patterns in a tube bundle geometry

3.1. Introduction

Chapter 2 presented the results of a crossflow study in compound channels, being the first step in our methodology to comprehend the crossflow in tube bundle geometry. In this chapter, the results of flow field investigations in a geometry very close to the real tube bundle geometry will be presented.

Earlier attempts to explain the flow characteristics in a rod bundle were concentrated mainly on the Reynolds stress driven secondary flows. Skinner *et al.* [43] were the first who attributed the higher rate of diffusivity in the gap to secondary flow since the mixing rates they measured were higher than could be accounted for by turbulent diffusion alone. Later, following the ideas of Skinner *et al.* [43] Singh and Pierre [44], Trupp and Azad [45] and Vonka [27, 28] emphasized the role of secondary flows in inter-sub-channel scalar transport.

In 1973-1974, Rowe *et al.* [7, 8] published their two component LDA measurements in rod bundles arranged in a square array shown in Figure 3-1(a). Their results clearly show that there exists an additional macroscopic flow process in the regions adjacent to the gaps, resulting in periodic flow pulsations across the gaps. The macroscopic flow pulsations observed by Rowe [7] have been confirmed by Hooper, Rehme and Wood [9, 10, 11, 12]. Hot wire measurements in air flow were conducted in a configuration with P/D = 1.07 and 1.107 as depicted in Figure 3-1(b). Their results showed that there exists an energetic and

almost periodic azimuthal turbulent velocity component directed through the gap. They found that the azimuthal turbulent velocity component cannot be associated with mean secondary-flow velocities driven by Reynolds-stress gradients.

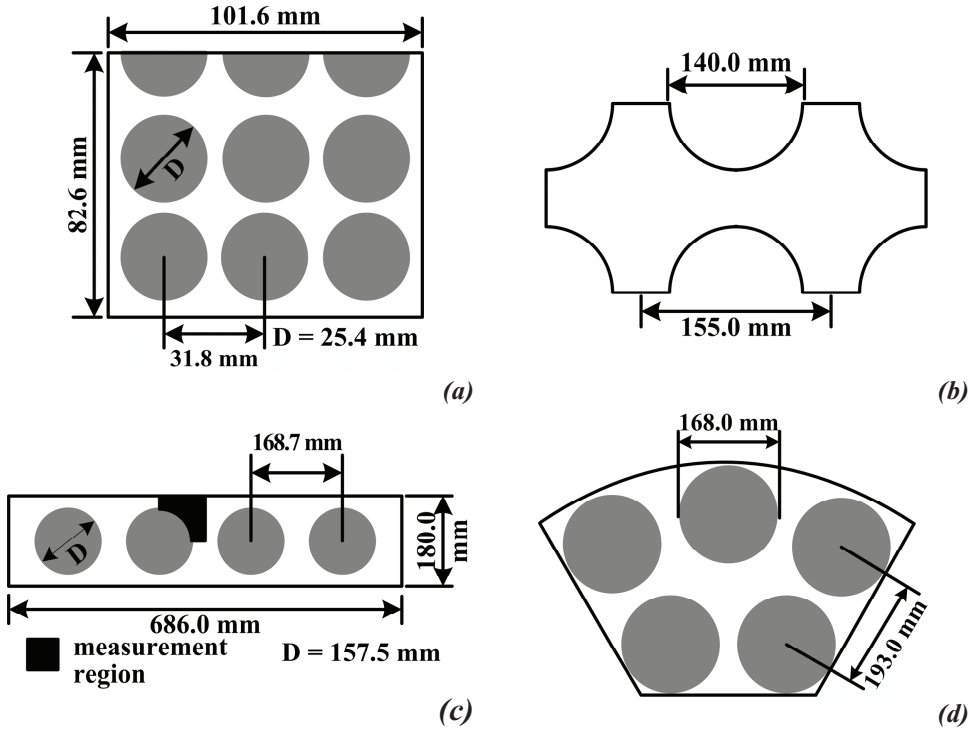

Figure 3-1: Cross sectional view of (a) setup used by Rowe [7, 8], (b) symmetrical square-pitch rod-cluster test section of Hooper, Rehme and Wood [10, 12], (c) 4 rod bundle investigated by Rehme [9] and (d) Baratto *et al.* [17] five rod test section.

In 1991, Möller [3] investigated the macroscopic flow pulsations in Rehme's 4-rod facility, Figure 3-1(c), as a function of gap width and channel Reynolds number with the help of hot wire anemometry. He proposed a flow model of a street of vortices moving in the center of the gap rotating alternately in opposite direction. Their axis would be perpendicular to the rod surface in the gap and would move in the axial direction. These macroscopic flow pulsations, caused by such large-scale vortices, cover almost the full cross-section of the sub-channel as shown by cross-correlation of the point measurements.

In 2006, Baratto *et al.* [17] published their experimental results obtained in a five rod test section, see Figure 3-1(d). The aim of this study was to determine heat transfer characteristics by using the hot wire anemometry technique. They found that coherent

structures in adjacent gap regions are highly correlated and interfere with each other to the point that a change in frequency in one gap, following a rod displacement, results in the same change in the frequency in the other gap.

In Chapter 2 the existence and influence of near gap large-scale vortices on the inter-channel crossflow was shown. In this chapter, a plane/curved surface on one side and a flat, main outer wall on the other side bounded the gap region. In a tube bundle geometry, however, two curved surfaces define the gap region with no near gap plane surface. Since the PIV measurement plane in compound channels was located as close as 1.0 mm from the near gap main outer wall, a certain influence of this flat outer wall on the mean flow properties is to be expected. The present study is intended to resolve this issue by investigating the near gap mean flow properties in a tube bundle geometry for a large range of Reynolds numbers as well. Furthermore, comparison of crossflow measurements in tube bundle geometry with compound channels (Chapter 2) helps in verifying whether the compound channels can mimic the flow behavior of tube bundle or not. Another aim of this study is to investigate the contribution of secondary flows to crossflow in a tube bundle geometry.

Tube bundle is a complex geometry, as compared to compound channels, and practically it is very difficult to access the lateral and streamwise planes of a tube bundle sub-channel by using PIV. Keeping in view this, non-intrusive, point measurement optical technique Laser Doppler Anemometry (LDA) was selected for measurements. However, due to the presence of curved surfaces in the path of light beams, use of LDA in tube bundle is subject to solution of refractive index matching (RIM) problem. An introduction to LDA and resolution to RIM problem are therefore addressed first in § 3.2 and 3.3, respectively.

3.2. Laser Doppler Anemometry (LDA)

The non-intrusive point measurement optical LDA technique is based on determining the frequency shift that light waves undergo when scattered by moving particles, i.e. the Doppler shift. A brief description of the method follows, detailed information can be found in e.g., Durst *et al.* [46] and Tummers [47]. An LDA system consists of a laser (typically a continuous wave Ar-Ion-laser), fiber optics, a frequency shifter, a signal processor, a traversing system and a computer to control the measurement and save the data. The velocity time series is measured at a point after which the probe is moved to next position. Moving the probe point by point, spatial velocity profiles can be determined. The principle of the velocity measurement can be explained with the so-called Fringe model. Figure 3-2 shows a typical dual beam LDA setup. The laser beam is first

divided into two beams with equal intensities. These beams are then led to the LDA probe using optical fibers. The focal length of the probe's front convex lens determines both the size and position of the crossing point of the two beams. The LDA probe optics guides the two laser beams into the measurement point where the beams cross each other and form an ellipsoidal measurement volume. In the fringe model, the crossing beams form bright and dark interference fringes, resulting in alternative high and low intensity planes perpendicular to the laser beam plane. The spacing between the fringes (d_f) is determined by the optical parameters of the setup, namely the laser light wavelength (λ), and the angle between the beams (α):

$$d_f = \frac{\lambda}{2\sin\left(\frac{\alpha}{2}\right)} \tag{3-1}$$

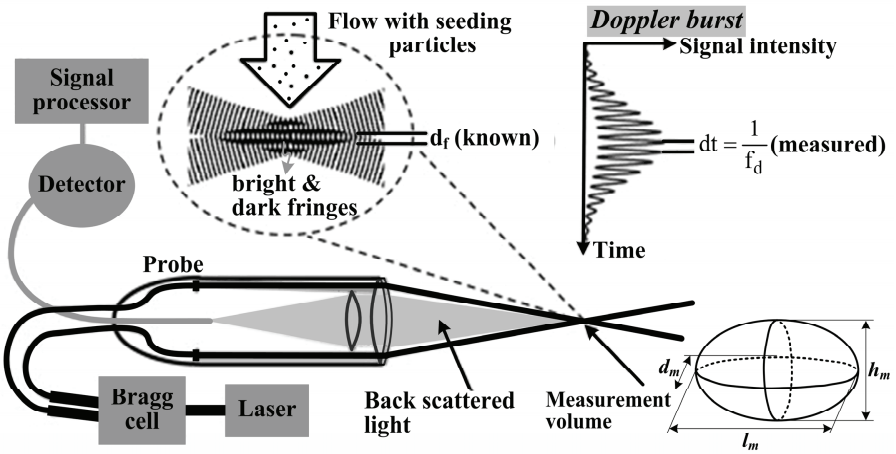

Figure 3-2: A typical dual beam LDA setup. d_f is the fringe spacing and f_d is the frequency of the Doppler burst from the seeding particles. h_m, d_m and l_m are the height, width and length of the ellipsoidal measurement volume, respectively.

The flow is seeded with reflecting particles, small enough to follow the motion of the fluid and validating the assumption that the velocity of the particles represents the velocity of the fluid. While passing through bright and dark fringes of the measurement volume, seeding particles scatter light of high and low intensity, respectively. The Doppler burst thus generated by the passage of a seeding particle from the measurement volume represents a time signal of high and low intensity light as shown in Figure 3-2. The frequency of the detected Doppler burst (f_d) is then related to the fringe spacing (d_f) to form the corresponding velocity component as:

$$v = d_f \,.\, f_d \qquad (3\text{-}2)$$

The velocity data for the present study was obtained with a two-component LDA setup. The laser used was a water cooled Ar-laser (by Spectra-Physics-Stabilite 2016) with a maximum power of 4.0 W. The laser light was separated into different wavelengths (λ_i), i.e., colored pairs of laser beams, using a TSI Colorburst 9201, with one beam of each pair shifted in frequency by the acousto-optic modulator, a Bragg cell. Three beam pairs were obtained: green (λ_g = 514.5 nm), blue (λ_b = 488.0 nm) and violet (λ_v = 476.5 nm). For the present study, the first two wavelengths were used, i.e., the blue pair for the streamwise velocity component and the green pair for the flow in the spanwise direction, see Figure 3-3.

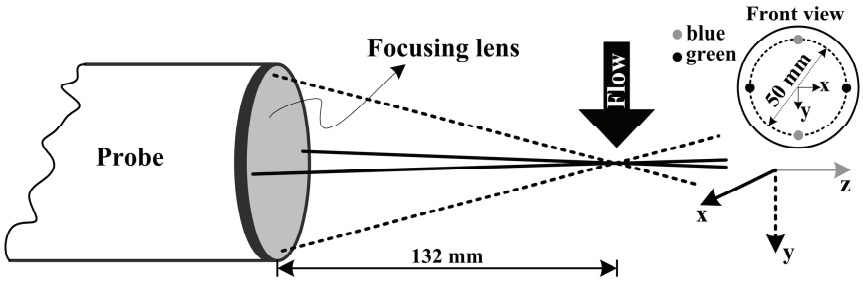

Figure 3-3: LDA probe setup for two components measurement, used in the present study. The focal length of the probe-focusing lens is 132.0 mm. The system of coordinates used for the measurements is also shown.

By using an optical fiber, each beam was then guided to the LDA probe mounted on a traverse system. The TSI 9832 probe, with a diameter of 83.0 mm, consists of a lens for focusing the laser beams onto a measurement point and receiving optics to collect the light reflected from seeding particles. The dimensions of the measurement volume are given in Table 3-1.

Table 3-1: Dimensions of measurement volume corresponding to laser wavelengths (λ) used in the present study.

λ (nm)	$^*h_m$ (x 10^{-6} m)	$^*d_m$ (x 10^{-6} m)	$^*l_m$(mm)
λ_g=514.5 (green colored)	28.8	29.1	0.216
λ_b=488.0 (blue colored)	27.3	27.6	0.205

**For explanation of these symbols see Figure 3-2*

The multicolor receiver (TSI Colorlink 9230) further splits the light scattered from seeding particles, collected at the probe, into different colors and measures the intensity of each color by using a photo multiplier. The seeding particles used have a diameter of 8-12 (x10^{-6}) m, a density of 1.05 - 1.15 kg/m^3 and a refractive index of 1.5. The maximum

amount of seeding during the experiment did not exceed 10^{-4}% of the volume of fluid, assuring that the fluid properties remained unchanged by this small amount of the seeding particles.

Dantec Dynamics BSA flow software and MatLab were used for online and offline data handling/processing, respectively. The BSA flow software also controlled the probe traversing system. Post processing of the velocity time series, received from the BSA flow software, was carried out by using in-house software for the following corrections/tasks:

- Removal of the velocity bias
- Implementation of coincidence criteria
- Checking for multiple validation
- Application of a slotting technique for the determination of the autocorrelation function and auto power spectral density (APSD).

For details of these LDA data treatments see [47, 48, 49].

3.3. Refractive index matching

One of the disadvantages of LDA is the requirement of optical access to the measurement region. The use of transparent, solid and curved/skewed walls, having a refractive index mismatched fluid around them, poses problems due to the refraction of the light beams. For example, misalignment of the measurement volume with the probe axis and in some cases even non-existence of the measurement volume since the light beams have such different paths that they no longer cross. The misalignment of the measurement volume introduces an unwanted uncertainty in the measurement location and the measured velocity components. In theory, by using optics laws and adjusting the orientation of the LDA probe this misalignment problem can be resolved. Such a procedure, however, is very cumbersome since the probe adjustment process needs to be repeated for each measurement location.

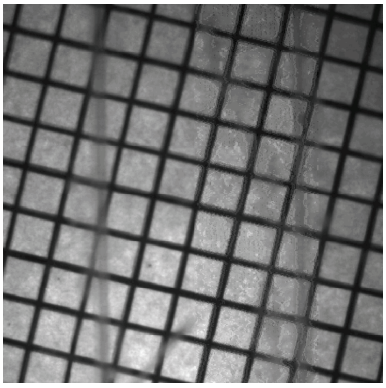

Figure 3-4: A FEP tube, having outer diameter=25.0 mm and wall thickness=0.25 mm, inserted in a box of water. Seemingly, the non-distorted background grid shows good RIM between water and FEP.

An alternative solution to the above-mentioned problems is the so-called refractive index matching (RIM) technique. By matching the refractive indices (η) of the fluid and the solid transparent walls, the latter optically "disappears" in the former. This phenomenon is caused by the fact that refraction at the solid walls is governed

by the ratio of the refractive indices of the walls and the fluid (Snell's law), being equal to unity in the case both refraction indices match. In general, two methods of RIM are being used [50, 51]:

(i) matching the fluid refractive index with the solid surface's one;

(ii) matching the solid surface refractive index with the fluid's one.

For the present study, the second option was chosen since fluids with refractive index similar to solids are often expensive, toxic, flammable, and/or very viscous. Moreover, use of these fluids in a large-scale flow facility with stringent safety measurements proves to be too expensive. With water as the working fluid, Fluorinated Ethylene Propylene (FEP) was selected as the solid material. At 20 ^{o}C, the refractive index of FEP ($\eta \approx 1.338$) is very close to the refractive index of water ($\eta \approx 1.333$). Figure 3-4 shows an initial test of the applicability of FEP as a refractive index matched material. A FEP tube inserted in water hardly causes any visual distortion of a grid in the background.

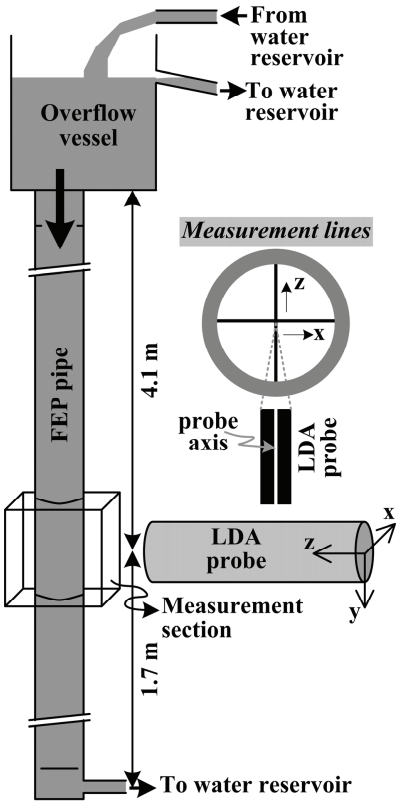

Figure 3-5: Flow loop along with measurement lines and the coordinate system used for LDA measurements in a FEP pipe flow.

3.3.1. Single-phase turbulent pipe flow

The applicability of FEP as refractive index matched material for our purposes was further verified by using the well-known case of single-phase turbulent pipe flow. The velocities were measured along two straight lines passing through the center, one parallel and other perpendicular to the laser probe axis corresponding to the z and x directions, respectively. The latter case is not possible without refractive index matching since the pair of laser beams passes through a curved pipe wall during the laser probe traversing. Figure 3-5 shows the flow loop, the measurement lines and the coordinate system used for this study. The inner diameter of the pipe (D_p) was 50.0 mm with a wall thickness of 1.0 mm. The fluid, being ordinary tap water at ambient conditions, flows in a vertically aligned FEP pipe under gravity from an overflow vessel placed at the top. Water from the bottom exit was first collected in a reservoir tank

and then pumped back to the overflow vessel by a centrifugal pump. Water was pumped around such that the Reynolds number of 5500 was reached, which corresponds to a volumetric flow rate of 0.72 m^3/hr. The measurement section consisted of a square box of Poly Methyl Methacrylate (PMMA) around the pipe filled with water at atmospheric pressure (see Figure 3-5). This ensured an equal refraction on either side of the FEP pipe walls and resulted in a negligible net change in the paths of the laser beams across the FEP walls.

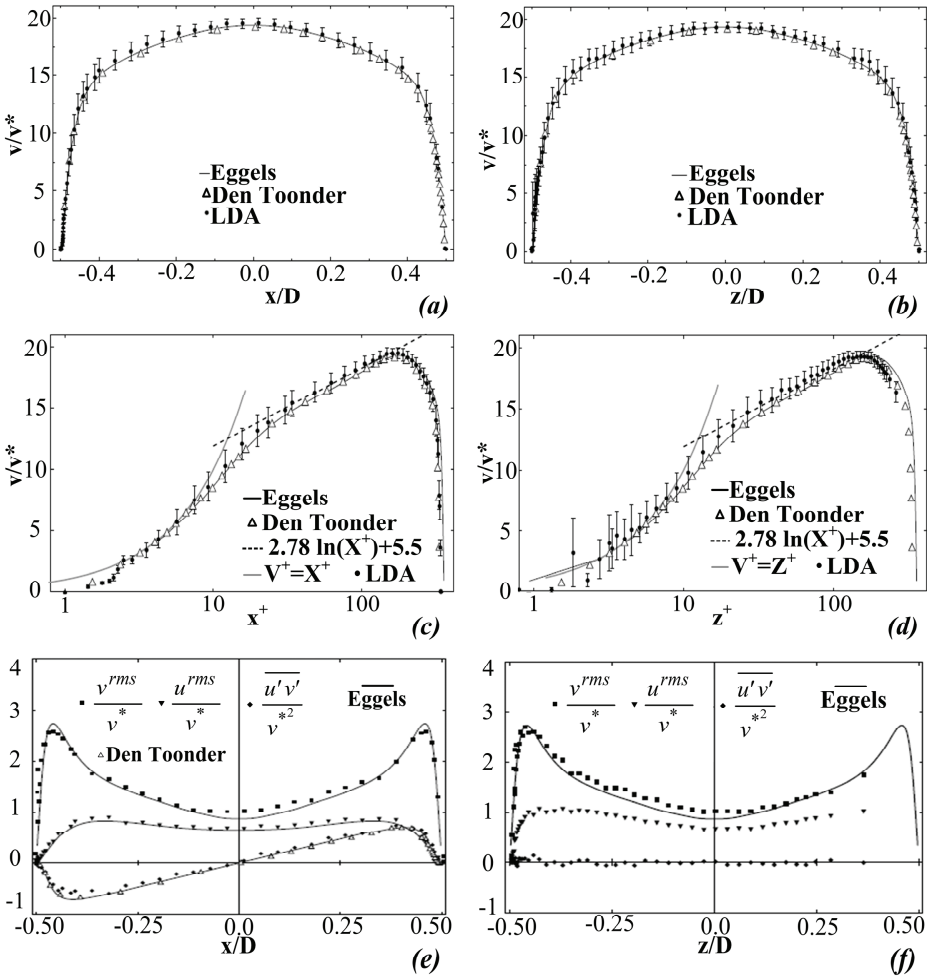

Figure 3-6: Results of LDA measurements in pipe flow, compared with the reference data. The left and right columns show results along the perpendicular and the parallel axes, respectively. Velocities are normalized by the friction velocity (v*). (a), (b) mean streamwise velocity profile across the pipe diameter (D_p). (c), (d) mean streamwise velocity as a function of non-dimensional wall distance y^+. (e), (f) RMS averaged velocities and turbulent stresses across D_p.

LDA measurements were carried out in the xz-plane, located 4.1 m downstream to the overflow vessel. The entrance length (L_e) for a pipe of diameter D_p can be estimated from Equation (3-3) [52].

$$\frac{L_e}{D_p} = 4.4(Re)^{\frac{1}{6}} \qquad (3\text{-}3)$$

As compared to the $L_e \approx 1.0$ m estimated from Equation (3-3), the streamwise distance of 4.1 m was more than enough to result in a fully developed turbulent flow at the measurements position.

The results of the velocity measurements carried out along the lines parallel and perpendicular to the probe axis are shown in Figures 3-6, together with the data of a direct numerical simulation (DNS) from Eggels *et al.* [53] and LDA data from Den Toonder [54]. Figures 3-6 show a very good agreement of our experimental data with the reference data, proving FEP to be a feasible refractive index matching material in a tube bundle geometry.

3.3.2. Transmittance of FEP

In order to quantify the attenuation of light by the FEP material, the LDA signal strength/data rate was determined as a function of FEP thickness. By using the turbulent pipe flow (Re=5500) case, as mentioned in the preceding section, the data rate at the center of the pipe was monitored while placing thin FEP sheets of variable thicknesses between the LDA probe and the PMMA box/measurement volume. Figure 3-7 shows the LDA data rate as a function of FEP layer thickness for green (λ_g = 514.5 nm) and blue (λ_b = 488.0 nm) light. An increase in FEP layer thickness results in an exponential decay of the data rate. The blue light clearly suffers more from attenuation due to the FEP material as compared to the green one. The FEP attenuation coefficient, determined from a linear fit to the data shown in Figure 3-7, is found to be -2.6 m^{-1} and -3.5 m^{-1} for the green and the blue light, respectively. Keeping in view the minimum sampling frequency requirement (≈ 2.0 Hz), estimated from compound channels measurements in Chapter 2, it is suggested that the total thickness of FEP between the LDA probe and the measurement volume should not exceed 2.4 mm.

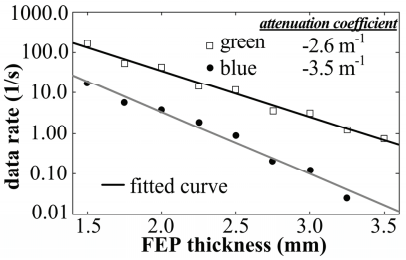

Figure 3-7: Transmittance of green and blue laser beams through FEP material. The data rate, obtained from LDA measurements in a pipe flow (Re=5500), is plotted as a function of FEP thickness.

3.4. Tube bundle setup and experimental flow loop

Figure 3-8 shows the tube bundle test section in flow loop and the LDA measurement section. Looking at the cross sectional view, the test section consists of eight near wall and one central sub-channels formed by setup of 4 x 4 tubes (4 quarter tubes, 8 half tubes and 4 full tubes).

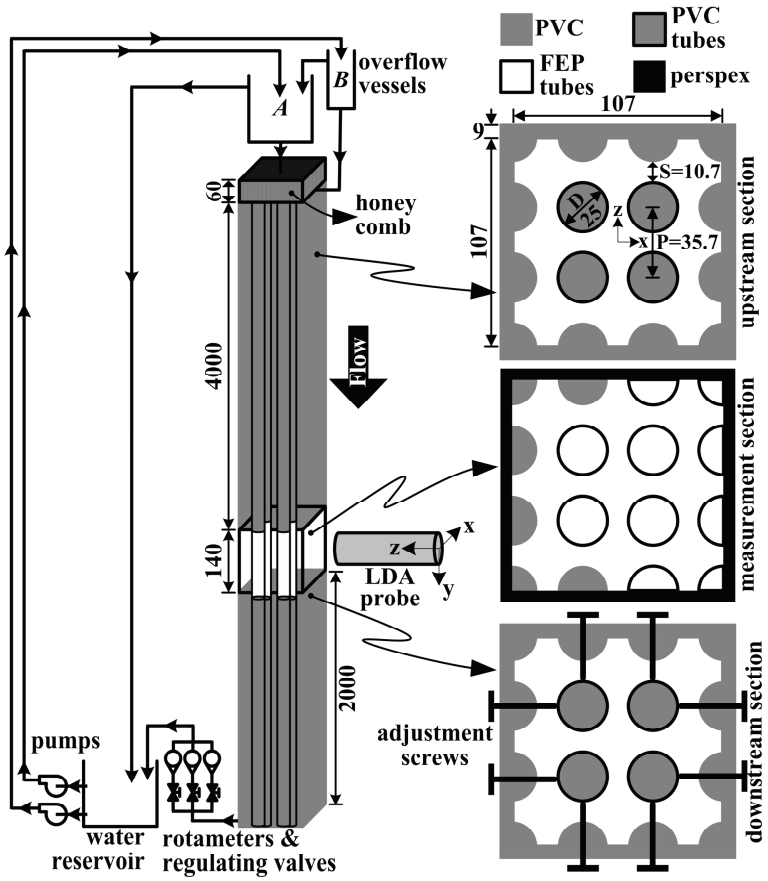

Figure 3-8: Experimental flow loop used for LDA measurements in a tube bundle. The figure also shows the cross sectional view of three segments of the test section along with the system of coordinates used. All dimensions are in mm and the figure is not to scale.

The diameter (D) to pitch (P) ratio in most of LWR fuel assemblies ranges from 0.77 to 0.70. The D/P of the tubes in the current setup had been chosen to be 0.7, for comparison reasons with the numerical work of Ikeno and Kajishima [29]. The outer diameter of the tubes, being 25.0 mm, was based on commercially available FEP tubes with a wall thickness of 0.3 mm that fulfills the data rate criteria, as discussed in the previous section.

Two separate centrifugal pumps lead water from the reservoir tank to overflow vessels A and B. Vessel A was meant to feed the main flow through the test section and vessel B was used to over-pressurize (and thus strengthen) the thin FEP tubes in the measurement section. The flow in the test section was gravity driven and had 4.0 m of developing length (≈ 100 times the cross sectional hydraulic diameter) before it entered the measurement section.

Flow straightening, i.e., removal of any swirl and cross stream movement of the fluid, was achieved by placing a honeycomb structure of 60.0 mm height and a mesh size of 6.0 mm at the inlet of the test section. The fluid flow was regulated by a set of valves and rotameters located between the outlet of the test section and the water reservoir tank. Figure 3-8 also shows the cross sectional view of different segments of the test section. The test section casing upstream and downstream of the measurement section consisted of 4 and 2 segments, each of length 1.0 m, respectively. The measurement section had a length of 0.14 m with a casing made of Perspex to facilitate the LDA optics. The half and the quarter tubes in path of the laser beams were shaped from 0.25 mm thick FEP sheet, whereas, the others were made from PVC rods. Flanges joined all the pieces of the test section casings as smooth as possible.

Each of four central tubes consisted of three parts in the streamwise direction; PVC tubes in the upstream and downstream section and a steel pipe in between with an optical access window located at the height of the measurement section, see Figure 3-9 (a). The optical access window in a pipe was made first by cutting out a part of steel pipe and then covering the opening with a 0.30 mm thick heat shrinkable FEP sleeve, as shown in Figure 3-9(b). This setting resulted in firm, vertically aligned FEP tubes with the drawback that some regions of the measurement section became inaccessible for LDA measurements. However, by optimally positioning the intact steel portions of the optical access windows, the central sub-channel region remained fully accessible for LDA measurements, as shown in Figure 3-9(c).

Spacers were placed at all flanges, except the one joining the measurement and the upstream section, to restrict the lateral movement of the four central tubes hanging from the top of the test section. Spacers were made out of a single 3.0 mm thick metallic plate by the method of spark eroding which resulted in a smooth strip-like tube support structure, see Figure 3-9(d). From the measurement section, the closest upstream spacer was located at a distance of 1.0 m. Placement and smoothness of the spacer ensured that the measurement section remains free from wake disturbances of the spacer structure.

To determine the four central tubes position, LDA measurements for laminar flow were performed along lines defining the gaps minimum spacing (S). A parabola fitted to

laminar measurements and extrapolated to zero velocity near the tube walls gave an accurate estimate of tube positions. Adjustment screws located just downstream of the measurement section (see Figure 3-8) were used to fine-tune the four central tubes positions. The maximum error in the tube positions was found to be ±0.8 mm, which is 7.5% of minimum gap spacing S.

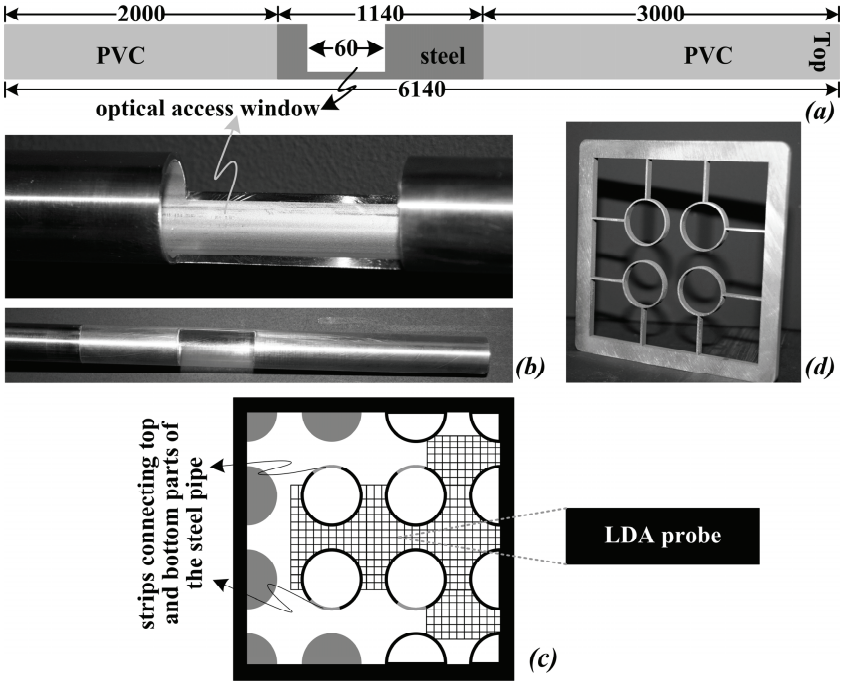

Figure 3-9: (a) Three sections of one of the tubes defining the central sub-channel. (b) Optical access window in the steel pipe without (upper) and with (lower) FEP sleeve. (c) Cross sectional view of the tube bundle setup depicting the region accessible for LDA measurements (highlighted by a checker pattern). (d) Spacer used at the flanges to restrict the lateral movement of the four central tubes.

3.5. Experimental results

This section presents the LDA results depicting the mean flow properties and the flow patterns in the tube bundle geometry under consideration. Being a representative of the actual sub-channel in a tube bundle geometry, the target region for the present study was the central sub-channel. The results presented in this section are for Re_{ch} ranging from 631 to 11037. The upper limit was based on the maximum flow possible. The results will be presented analogous to the presentation pattern followed in Chapter 2 for compound channels.

Due to the presence of low flow (gap) and high flow (sub-channel) regions, the results of the tube bundle geometry are expected to be in qualitative agreement with the compound channels findings. In this section the focus, therefore, will be on answering the question:

How does the gap location and geometric parameters variation affect the quantitative similarity between the tube bundle and the compound channels results?

Table 3-2: Comparison of tube bundle geometric parameters with compound channels.

Test section	S (mm)	D (mm)	S/D	D_h^{ch} (mm)	D_h^{gap} (mm)
Tube bundle	10.7	25.0	0.428	39.9	20.5
R-3	3.0	21.0	0.143	24.2	6.0
C-2	2.0	21.0	0.095	23.7	6.6
C-3	3.0	21.0	0.143	24.2	8.2

For comparison purposes, Table 3-2 shows total (D_h^{ch}) and gap (D_h^{gap}) hydraulic diameters for all the test sections. All values are based on the lateral cross sectional projection of the test sections. D_h^{gap} is based on the flow area and the wetted perimeter bounded by the gap of depth D and minimum gap spacing S. Remind the coordinate system, x, y and z being the spanwise, streamwise and the transverse directions, respectively. The corresponding x, y and z-velocity components are u, v and w, respectively

3.5.1. Time averaged streamwise velocity profiles

The measurements were carried out along three straight lines A, B and C, see Figure 3-10. Line A, located at z=0.0 and extending from x=0.0 to x=P/2, covers half of the gap region and half of the central sub-channels. Line B, located at x=0.0, extends from z=0.0 to z=P and covers the full gap region and half of the adjacent sub-channels. Line C at z=P/2 extends from x=±S/2 and covers the minimum gap spacing. The center and near wall sub-channels covered by the line B are designated as Ch-1 and Ch-2, respectively. Figure 3-11 shows examples of four streamwise velocity profiles measured along lines B and C normalized by V_{bulk}. The unsymmetrical behavior of the profile along line B is due to the presence of the outer casing wall near Ch-2. In the case of compound channels, the streamwise velocity was less than V_{bulk} due to the location of the gap region near

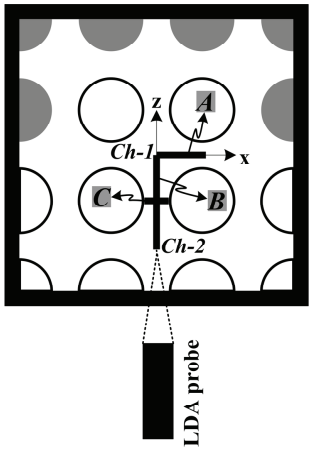

Figure 3-10: LDA measurement lines A, B and C (Grey colored). Center and near-wall sub-channels are identified as Ch-1 and Ch-2, respectively.

the main outer wall. In the present case, however, the streamwise velocity at all locations is greater than V_{bulk} for all values of Re_{ch}.

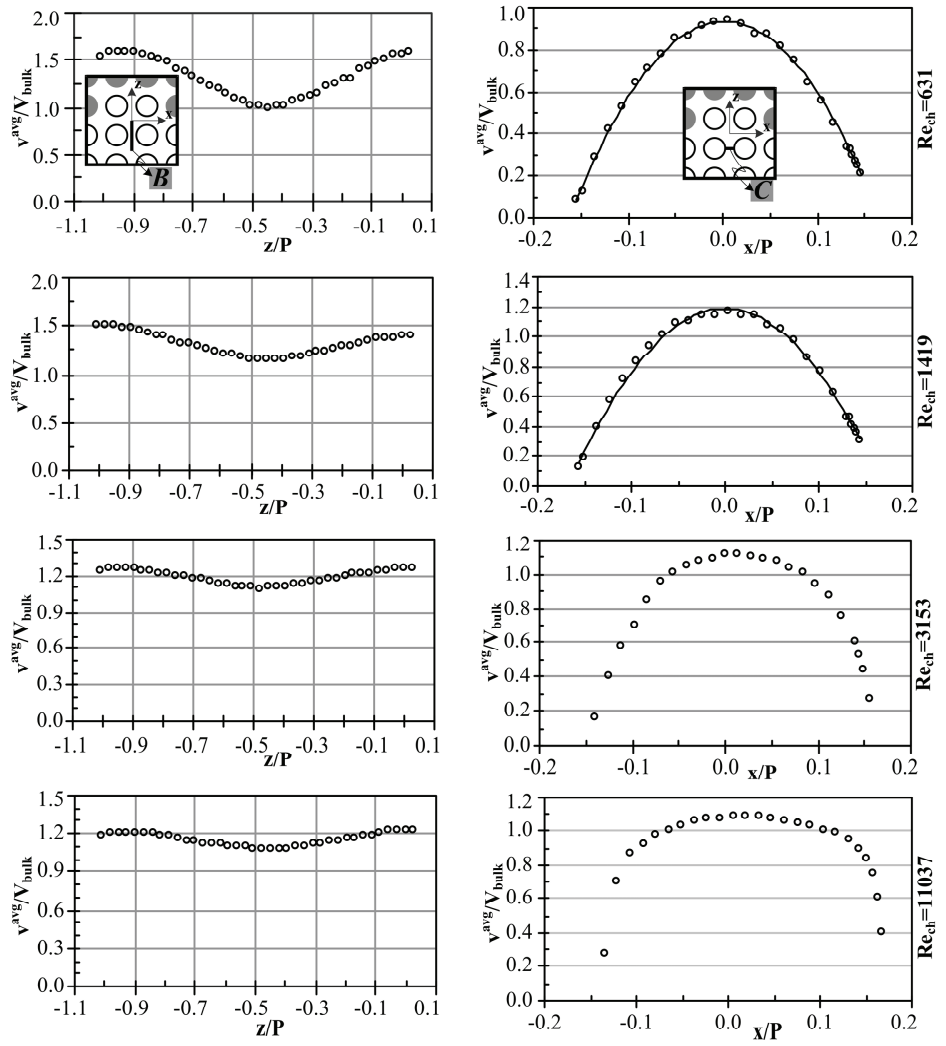

Figure 3-11: Streamwise velocity profiles along line B (1st column) and line C (2nd column). Line B and C are shown as insets in top figures. The distances and velocities are normalized by the pitch (P) and the $^{*}V_{bulk}$, respectively. Open bullets: experimental results and solid lines: fitted parabolic curve.

The streamwise velocity profile along the line C clearly identifies whether the flow in the gap region is laminar or turbulent. For Re_{ch}=631 and 1419, the flow in the gap region

* V_{bulk}, = (total flow rate) / (the lateral cross sectional flow area of the tube bundle).

is laminar, confirmed by fitting a parabolic curve to the measurements. At Re_{ch}=3153, a transition from laminar to turbulent flow in the gap is depicted by the results. At Re_{ch}=11037 a fully turbulent streamwise velocity profile in the gap region is visible.

As shown in Chapter 2, to estimate the flow type in the gap region from Re_{ch}, a plot of the approximate gap Reynolds numbers ($Re_{g\text{-}app}$) vs. the channel Reynolds number (Re_{ch}) can be used, see Figure 3-12. $Re_{g\text{-}app}$ is based on the D_h^{gap} and streamwise velocity averaged in time and space between z=±D/2 along the line B, i.e., the gap region. Therefore, the real gap Reynolds numbers calculated from the streamwise velocity based on the total cross sectional gap region flow area (between z=±D/2) would be somewhat higher than the $Re_{g\text{-}app}$ Assuming a Reynolds number of 2000 roughly as an upper limit for the existence of laminar flow, the flow in the gap region is laminar up to Re_{ch}≈3200, which is significantly lower than what was found in case of compound channels, i.e., Re_{ch}≈6000. As predicted and discussed in Chapter 2, a gap region formed by two curved surfaces in the tube bundle allows extension of high velocity channel fluid into the low velocity gap region across z=±D/2. This expansion of the channel flow towards the middle of the gap region results in a gap flow regime transition at low Re_{ch} in the tube bundle as compared to the compound channels.

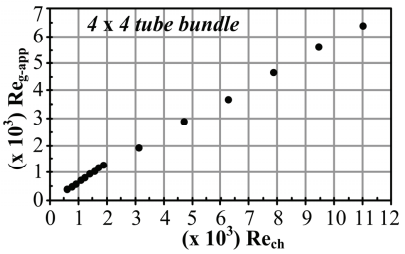

Figure 3-12: Approximate gap Reynolds numbers as a function of channel Reynolds numbers.

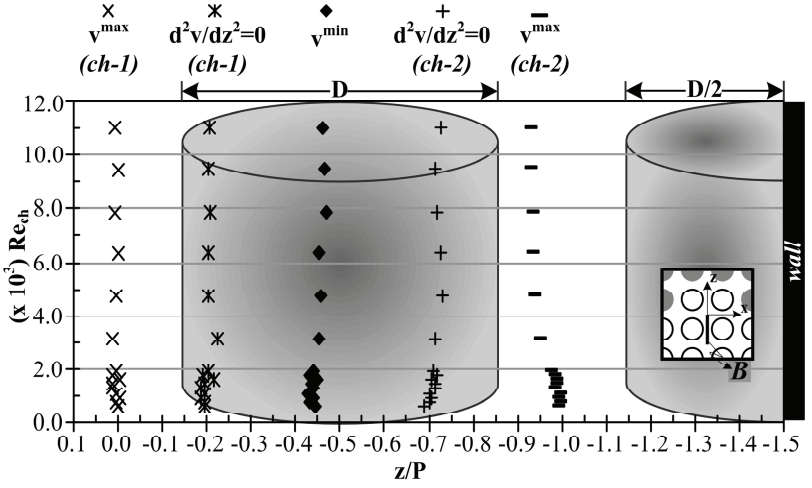

Figure 3-13: Location of points of maxima, minima and inflection on the time-averaged streamwise velocity profile measured along line B in the tube bundle.

Figure 3-13 indeed shows a shift of the location of the inflection points (being indicative of the boundary between the channel's high flow and gap's low flow regions) towards the center of the gap region. The inflection point between the near-wall sub-channel (Ch-2) and the gap region shows a larger shift as compared to the one between the center sub-channel (Ch-1) and the gap region due to the outer casing wall effect. For compound channels (with rectangular as well as curved gap regions), the inflection points were located at x=±D/2. These findings suggest a need for a new definition of the gap region in a tube bundle geometry. This issue is further discussed in Chapter 4. A shift in the streamwise velocity profile towards the origin of the tube bundle due to the outer casing wall is also visible in Figure 3-13. The maxima and minima are, instead of being located at z/P=-1.0 and z/P=-0.5, respectively, shifted leftwards, i.e., to higher values of z/P.

3.5.2. Dependence of flow characteristics on Re_{ch}

Figure 3-14(a) shows the magnitude of the time averaged velocities at the points of maxima (v^{max}), minima (v^{min}) and inflection ($v^{inflec.pt.}$) as a function of Re_{ch}. Figure 3-14(a) also shows the average of v^{max} and v^{min} (v^{avg}). All values of velocities are non-dimensionalized by V_{bulk}. For Re_{ch}>3000 (marking the transition from laminar to turbulent flow in the gap region) all the velocities linearly scale with the V_{bulk} (and thus with Re_{ch}). For compound channels, since the PIV measurements were performed approximately in the buffer layer, the increasing trend of (v^{max} /V_{bulk}) is consistent with the changing shape of the channel's streamwise velocity profile. In a tube bundle geometry, however, v^{max} is practically the sub-channels center line velocity (v^{CL}), free from any near wall effect, and hence scales linearly with V_{bulk}.

A comparison of Figure 3-14(a) and Figure 2-19 yields the following observations:

- For the tube bundle geometry both v^{max} and v^{min} are larger than V_{bulk}. On the other hand in the compound channels v^{max} and v^{min} are both smaller than V_{bulk} The main reason for this difference is that the PIV measurement plane in the compound channels is located in the buffer layer near the main outer wall.
- The difference between v^{max} and v^{min}, Δv, is lower in a tube bundle geometry than the velocity difference in the compound channels. Figure 3-14(b) shows the dependency of Δv on D_h^{gap}, since Δv decreases with increasing D_h^{gap}. Furthermore, Figure 3-14(c) shows that Δv scales approximately linearly with V_{bulk} for Re_{ch}>3000.
- The sub-channels center line velocity (v^{CL}) in compound channels is larger than v^{max} since the PIV measurement plane is located near/in the buffer layer. The slope of Δv in Figure 3-14(b) for compound channels would therefore increase if we

consider the centerline velocity as the maximum velocity. By doing so, the dependency of Δv on D_h^{gap} remains preserved, i.e. the larger D_h^{gap}, the smaller Δv.

- The quantitative differences in Δv for compound channels and the tube bundle are due to the combined effect of the gap shape/geometry and the location of the gap region, as discussed in § 2.5.3. Hence, a quantitative agreement in compound channels (R-3, C-2, C-3) and tube bundle results is unlikely. The implications of Δv on the streamwise structure length and cross velocity pulsations in the gap region for different test sections will be further discussed in § 3.5.3.

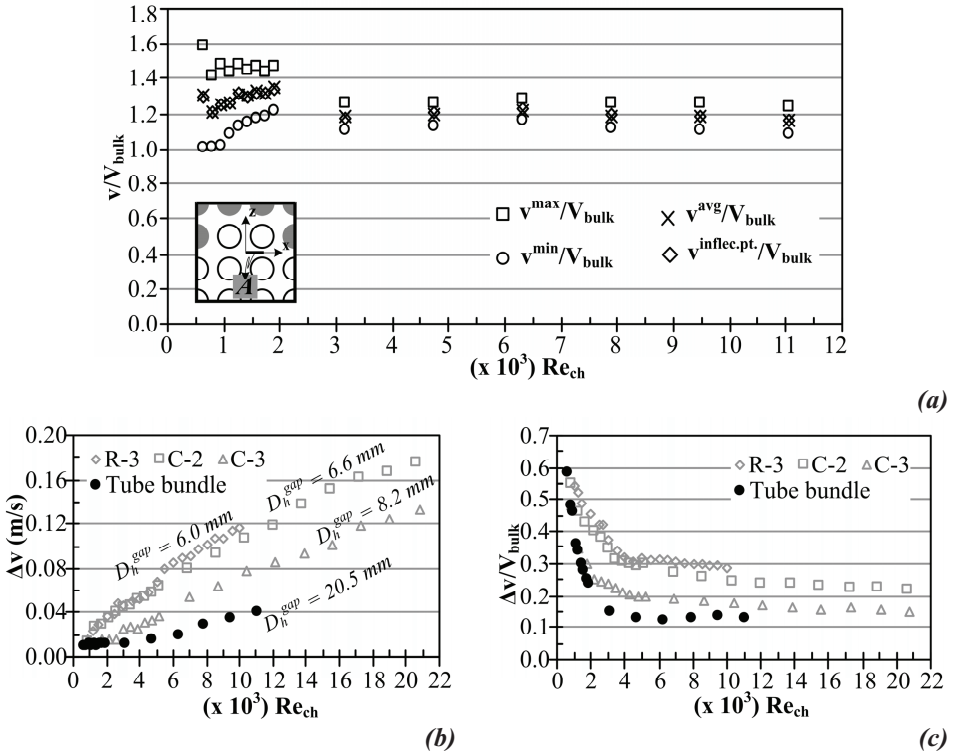

Figure 3-14: (a) Normalized magnitude of velocities at points of maxima, minima and inflection on the streamwise velocity profile. (b) Absolute and (c) normalized difference of the maximum (v_{max}) and the minimum (v_{min}) time averaged streamwise velocity (Δv) as a function of Re_{ch} for compound channels and the tube bundle geometry. All measurements carried out along a line in the spanwise direction passing through the center of the gap region (line A in the case of tube bundle).

The root mean square of the spanwise velocity pulsations (u^{rms}) in the gap region, a measure of crossflow, is shown in Figure 3-15. The measurements were performed along

line A (see Figure 3-10). All values of u^{rms} are presented in absolute values, Figure 3-15(a), and as a percentage of V_{bulk}, Figure 3-15(b). For comparison purposes, u^{rms} in the gap regions of compound channels (R-3, C-2, C-3) are also plotted. Figure 3-15, reveals a weaker crossflow in a tube bundle geometry (≈5% of V_{bulk}) compared to the crossflow in compound channels(≈11% of V_{bulk}). Clarification of this difference requires knowledge on the coherent structures in the bundle geometry. Therefore, the coherent structures need to be investigated first, which will be done in the next section.

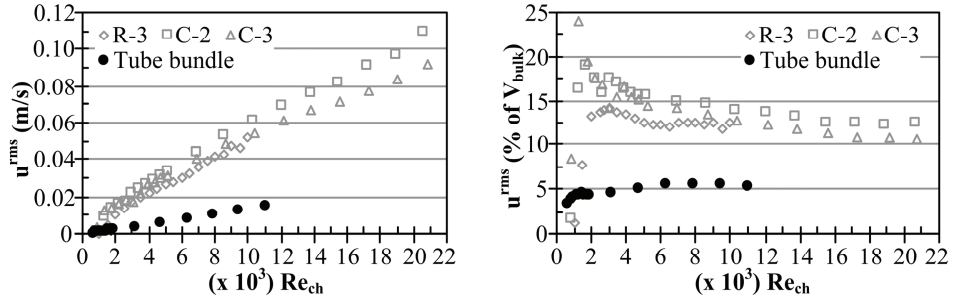

(a) *(b)*

Figure 3-15: A comparison between the (a) absolute and (b) normalized RMS of the spanwise velocity pulsations in the gap region of the tube bundle and the compound channels as a function of Re_{ch}. For the tube bundle the u^{rms} of the velocity signal measured at (x/P, y/P, z/P)=(0.5, 0.0, 0.0) is presented.

3.5.3. Coherent structures

In Chapter 2, the streamwise length of the near gap coherent vortices was estimated from Taylor's frozen flow hypothesis by using Equation (2-8), i.e.:

$$L^{str} = v^{str} \cdot t \qquad (3\text{-}4)$$

where L^{str} = the streamwise length of the vortex
v^{str} = the streamwise structure velocity
t = characteristic time scale of coherent vortices.

For compound channels the cross correlation of the spanwise/streamwise velocity component could be determined from the two-dimensional PIV results, leading to the estimate of the structure velocity. With LDA, however, being a single point measurement technique, it is not possible to obtain such a cross correlation. Based on the results of compound channels (Chapter 2) it is therefore assumed that in the tube bundle $v^{str} \approx v^{inflec.pt.}$. The presence of coherent vortices appears as a peak in the one-dimensional auto power spectral density (APSD) plot [55] of a cross velocity time signal measured at a point in the flow field, as shown in Figure 3-16(a). The time lag Δt in Equation (3-4) is estimated from the frequency of the peak in the APSD plot of the gap spanwise velocity signal. Figure 3-16

depicts the streamwise structure length estimated from Equation (3-4), averaged along the x-axis (line A) at 10 measurement points as a function of Re_{ch}. For comparison purposes the streamwise structure length is presented in centimeters, Figure 3-16(b), and normalized by the gap hydraulic diameter, Figure 3-16(c).

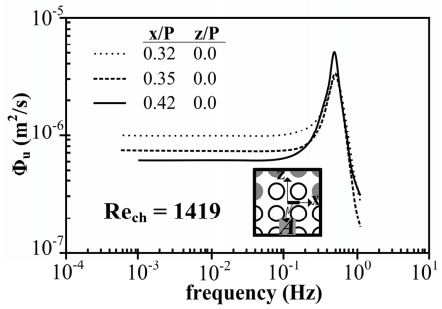

(a)

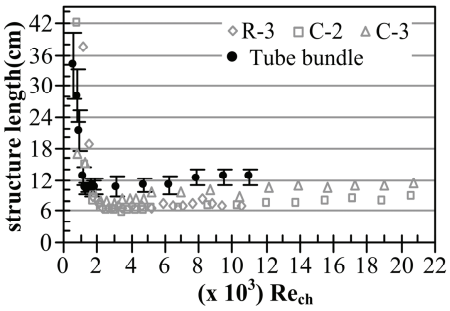

(b)

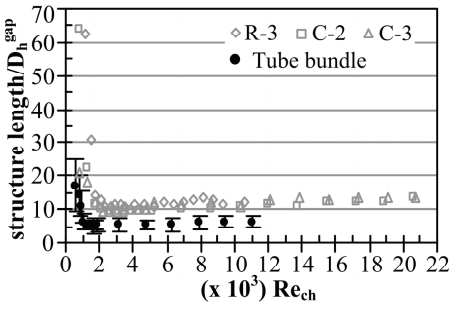

(c)

Figure 3-16: (a) An example of APSD of the cross velocity component measured along the line A at locations (x/P=0.32, z/P=0.0), (x/P=0.35, z/P=0.0) and (x/P=0.42, z/P=0.0) for Rech=1419. Peaks in the plot indicate presence of coherent vortices. Streamwise structure length (b) in cm and (c) normalized by gap hydraulic diameter as a function of Re_{ch} in a tube bundle geometry and compound channels (R-3, C-2 and C-3).

Since the gap geometry of C-2 and C-3 is comparable to the one in the tube bundle, it is appropriate to compare the results of these two cases. Main conclusions are as follows:

- from comparison of Figures 3-14(b) and 3-16(b); for each Re_{ch}, a decrease in Δv, due to an increase in D_h^{gap}, results in a relatively longer structures in the streamwise direction;
- comparing Figures 3-15(a) and 3-16(b), for each Re_{ch}, low and high values of u^{rms} are associated with relatively large and small streamwise structure lengths, respectively;
- for Re_{ch}>2000 the streamwise structure length for all the test sections becomes independent of flow properties due to the wall bounded shear flow effect (see § 2.5.3.);
- due to the location and the geometry of the gap region, quantitative differences exist between the coherent structures and the corresponding crossflow in the tube bundle geometry and the compound channels.

This leads to the conclusion that qualitatively, the crossflow mixing phenomenon in both the geometries is expected to be alike.

3.6. Secondary flows

This section presents the results of measurements carried out to investigate secondary flows at Re_{ch}=9130 in the tube bundle geometry. The aim is to find out ***whether in a tube bundle the large-scale structures contribution towards the crossflow dominates over the secondary flows or not?*** LDA measurements were performed in a quarter of the central sub-channel on a grid with dx=dz=1.0 mm within the flow area bounded between x/P=z/P=0.0 to x/P=z/P=0.5, see Figure 3-17(a). The choice of this measurement region was based on the experimentally determined tube positions, which revealed that tubes 2, 3 and 4 have a minimum positioning error. The experimental findings presented in this section are compared with CFD simulation (LES) results of Ikeno [29]. The simulation domain size used was 6P×2P×2P in streamwise, spanwise and transverse directions. By using periodic boundary condition in each direction, an infinitely long and wide rod bundle was simulated. The 2D-LDA measurement gives only the spanwise velocity component (u) in the xz plane. An estimate of secondary flows on the other hand also requires the transverse velocity component (w). Using symmetry line, the measurement region can be subdivided into Region-I and Region-II, as shown in Figure 3-17(b). To estimate w, the u measured at a point in Region-I was projected across the symmetry line to obtain w at a point (equidistant from the symmetry line) in Region-II and vice versa, see Figure 3-17(b).

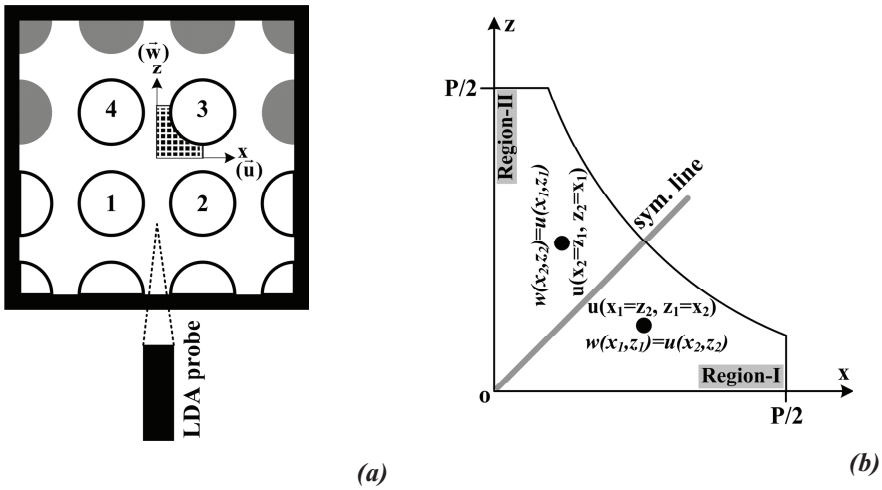

Figure 3-17: (a) Secondary flows measurement region in xz-plane, (b) Estimation of the transverse velocity component (w) from the measured spanwise component (u) using the symmetry line.

From Figure 3-18, showing the numerical and experimental secondary flow results in the form of vectors and stream traces plots, it can be deduced that:

- secondary flow patterns are resolved by using the LDA measurements;
- ignoring the spurious vectors at x/P=z/P≈0.5, the maximum magnitude of the measured secondary flow vector is found to be 0.9% of the maximum average streamwise velocity at the origin (v^{max}). This value is higher than the 0.7% found in the CFD results.

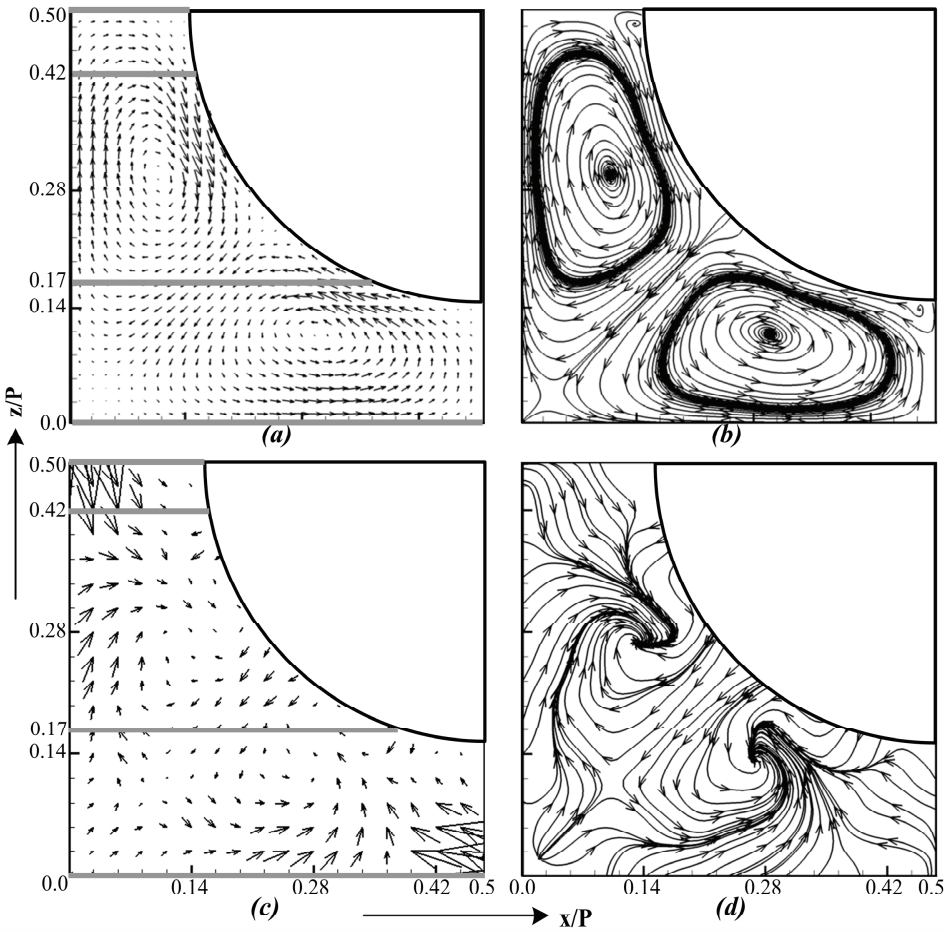

Figure 3-18: Secondary flow vectors from (a) CFD and (c) LDA measurements. Plot of the stream traces for (b) CFD and (d) LDA measurements. Re_{ch}=9130.

Figure 3-19 depicts a quantitative comparison in the form of mean spanwise velocity profiles at different transverse, z/P, positions (the grey lines in Figure 3-18(a) and (c)).

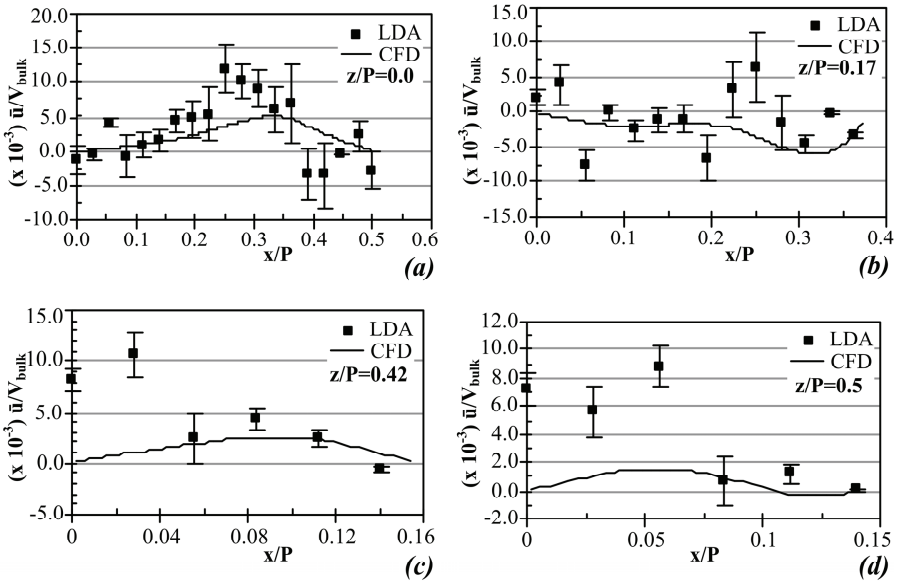

Figure 3-19: Mean spanwise velocity profiles at Re_{ch}=9130 along the lines at (a) z/P=0.0, (b) z/P=0.17, (c) z/P=0.42 and (d) z/P=0.5. Re_{ch}=9130.

Although a qualitative agreement with the simulations is present, most of the measured values are on the higher side compared to the reference CFD results. The maximum spanwise velocity component reported in the CFD results is nearly 0.5% of the V_{bulk}. It is very difficult to measure such small velocities keeping in view the following factors contributing to the uncertainties in the measurements:

- instrumentation noise;
- attenuation of the laser beams by the FEP resulting in a weaker LDA signal. This becomes increasingly important as the number of FEP layers in between the measurement volume and the laser probe increases, i.e., for measurement points located relatively far away from the probe in the transverse (z) direction. Furthermore, for some measurement locations the en route laser beam pairs (or single beam of the pair) traverse the maximum distance through the FEP curved wall resulting in a further increase in the attenuation;
- reflection of laser light from FEP surface, decreasing the validation of the LDA burst;
- the measurement volume misalignment that could be caused by a misaligned LDA probe and/or a refractive index mismatch (although small in our case) between FEP and water.

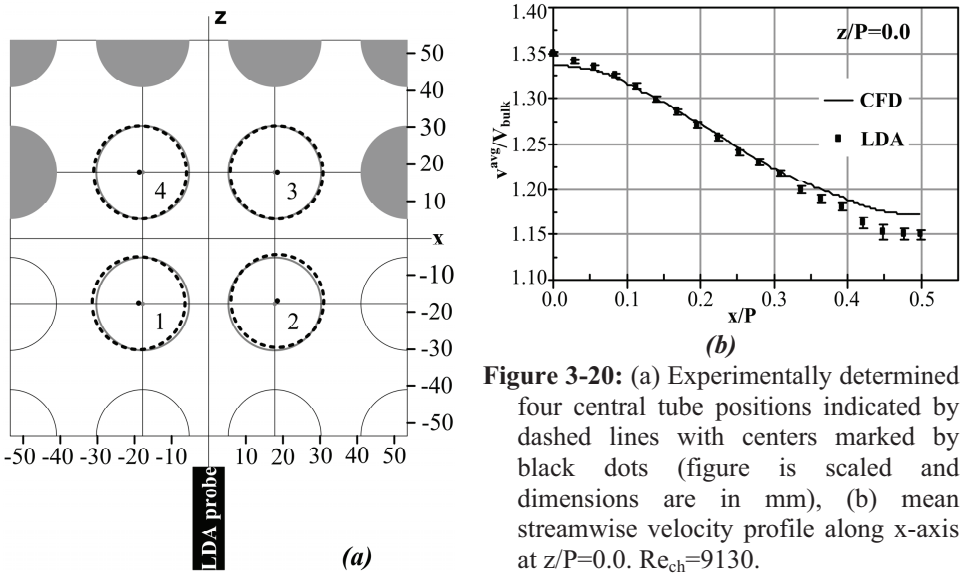

Figure 3-20: (a) Experimentally determined four central tube positions indicated by dashed lines with centers marked by black dots (figure is scaled and dimensions are in mm), (b) mean streamwise velocity profile along x-axis at z/P=0.0. Re_{ch}=9130.

The spurious vectors in Figure 3-18, located near x/P=z/P≈0.5, are due to the noisy LDA signal resulting from the above-mentioned effects. In addition to these factors, the differences in the CFD and experimental results might also be due to the following dissimilarities between the simulation and the experimental setup:

- geometric irregularities in the experimental setup, particularly due to the thin walled water filled FEP tubes in the measurement section;
- asymmetry in the central sub-channel of the experimental facility due to an error in the four central tubes positioning. As shown in Figure 3-20(a) the experimentally determined tube positions are off centered as compared to the reference tube positions;
- as mentioned earlier, the CFD results were obtained for an infinitely long and wide tube bundle geometry, where periodic boundary condition in each direction were used [29]. Any influence on the streamwise direction on the measurements can be neglected since enough upstream distance is available to obtain a fully developed flow at the measurement section. The influence of walls, located in the spanwise and the transverse directions (at x/P=z/P=1.5), possibly have an influence on the experimental results. The effect of the wall is visible by comparing the measured and simulated mean streamwise velocity profile along x-axis at z/P=0.0, as depicted in Figure 3-20(b). Especially the minimum velocity within the gap region is found to be lower than the CFD results show, as the friction of the outer wall tends to decrease the average streamwise velocities. Moreover, in Figure 3-20(b) an asymmetric

streamwise velocity profile at x/P=0.0, i.e., a non-zero velocity gradient, is apparent due to the error in the four center tubes positions.

By comparing the magnitudes of the measured secondary flows (≈0.9% of V_{bulk}) and the u^{rms} (≈5.0% of V_{bulk}) in the gap region (shown in Figure 3-15) it might be concluded that the contributions of secondary flows towards the crossflow mixing is not significant. This finding is consistent with the compound channel case (R-3) as discussed in Chapter 2.

3.7. Conclusions

The velocity field in the gap region of a 4x4 vertical tube bundle has been studied. The focus of the study was to investigate the crossflow through the gap region and compare the results with the compound channels findings (Chapter 2). Experiments have been performed using the 2D-LDA technique for channel Reynolds numbers ranging from 631 to 11037. The conclusions that can be drawn from the study are as follows:

- FEP can be effectively used as a refractive index matching material. Care, however, should be taken to the attenuating and reflection effect of the material.
- Just like the compound channels in Chapter 2, the bundle geometry shows a typical mixing-layer streamwise velocity profile. This profile is required for inducing the coherent structures.
- Compared to compound channels, the gap geometry in a tube bundle allows the transition of laminar to turbulent flow at low Re_{ch} inside the gap region due to relatively large expansion of channel fluid flowing towards the middle of the gap. This effect is expected to be beneficial for mixing.
- The trend of the streamwise structure length and u^{rms} in the gap region (a measure of crossflow) in the tube bundle is found to be in accordance with the compound channels findings.
- Qualitatively, secondary flows were successfully identified in the sub-channel of a tube bundle geometry. However, due to very small magnitudes of the spanwise velocity component and the high noise level in the LDA velocity signal, a quantitative agreement with CFD results was not achieved. Nevertheless, the measured secondary flow, being 0.9% of the bulk velocity, is even lower than the spanwise velocity pulsations (due to large-scale coherent structures) in the gap region (≈5.0% of V_{bulk}). This shows a minor role of secondary flow towards the inter-sub-channel crossflow. A similar result was found for compound channels (R-3) in Chapter 2.
- Based on the similarity between the tube bundle and the compound channels results, it seems justified that the crossflow results and, in turn, the crossflow mixing results of compound channels are also applicable to the tube bundle geometry.

4

Experimental quantification of crossflow mixing

4.1. Introduction

After the flow patterns identification work, presented in Chapters 2 and 3, this chapter presents the results of an experimental study carried out to quantify the inter-channel crossflow mixing. Based on the relevance of the crossflow findings in the compound channels and the tube bundle geometry (discussed in Chapter 3), the crossflow mixing experiments has been carried out for compound channels only.

In order to numerically determine the detailed flow and temperature distributions in a tube bundle geometry including inter-channel crossflow mixing, the "lumped parameter" approach is frequently used. In this approach, the bundle is considered as a set of one dimensional, continuously interconnected, parallel flow sub-channels, coupled to each other by crossflow through the gaps. By applying the conservation equations of mass, energy and momentum to the interconnected flow channels, a set of coupled differential equations can be derived to describe the thermal transport in a rod bundle. The major drawback of this method is that it ignores the fine structures of velocity and temperature within the sub-channels. The average values of temperature, pressure and velocity defining the state of a sub-channel are used instead.

Many experimental results in rod bundles have shown much higher mixing rates than those predicted by conventional mixing/diffusion theory. This higher inter-channel mixing

results from crossflow oscillations in the gap region induced by large-scale vortices [24]. Henceforth, the term 'crossflow mixing' refers to inter-channel mixing with contributions from both coherent structures and/or turbulence. The phrase 'turbulent mixing' on the other hand, symbolizes the inter-channel mixing due to turbulence alone. The contribution of large-scale vortices towards the crossflow mixing is generally taken into account by introducing empirical mixing coefficients (β) or a mixing factor (Y) due to non-existence of any definitive model. The mixing coefficient/factor, determined experimentally, is reported in the literature as correlations by using different dimensional/non-dimensional parameters.

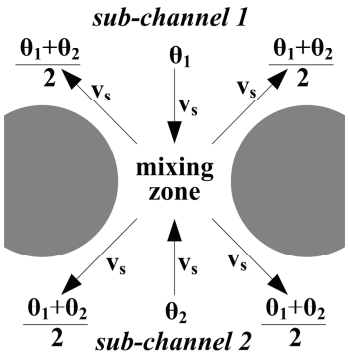

Figure 4-1: Secondary flow model of Skinner *et al.*[43], v_s is secondary velocity, θ_1 and θ_2 are sub-channels 1 and 2 temperatures, respectively.

The earlier inter-channel mixing models were based on secondary flows. Skinner *et al.* [43] suggested that in a tube bundle, the sub-channel fluids transported by secondary flows towards the gap region undergo a process of mixing there, Figure 4-1. Furthermore, due to the secondary flows this mixed fluid then flows out of the gap region towards the sub-channels. Later studies carried out by Galbraith and Knudsen [56] and Singh and St. Pierre [44] showed that the inter-channel mixing rate decreases with a decrease in the gap spacing. Surprisingly, for a certain range of P/D (1.102-1.02), this decreasing trend of mixing rate was found to deviate to higher values. This increase in the mixing rate for a range of P/D was again attributed to the secondary flows. Rowe *et al.*[7, 8] suggested in 1973 that the increase in mixing, over a range of P/D, could not merely be due to secondary flows; the contributions from crossflow pulsations in the gap region (due to large scale vortices) also need to be considered.

Later on, several experimental campaigns [20] have resulted in a number of correlations for β and Y. Nearly all of these correlations are valid only for a limited range of Re_{ch} and gap spacing (S). Consider, for example, the following correlations proposed by Rogers and Tahir [18] for the mixing flow rate from sub-channel i to j per unit length (m'_{ij}) through a gap of depth D and spacing S:

$$\frac{m'_{ij}}{\mu} = 0.0050\,Re_{ch}^{0.9}\left(\frac{S}{D}\right)^{-0.106} \quad \text{(for a square arrayed tube bundle)} \qquad (4\text{-}1)$$

$$\frac{m'_{ij}}{\mu} = 0.0018\,Re_{ch}^{0.9}\left(\frac{S}{D}\right)^{-0.4} \quad \text{(for a triangular arrayed tube bundle)} \qquad (4\text{-}2)$$

It is obvious that the correlations (4-1) and (4-2) are destined to fail when gap spacing (S) approaches to zero.

Lexmond *et al.* [16] attempted to resolve the deficiencies of those correlations. From their PIV and tracer transport measurements in compound rectangular channels, they proposed a dimensionless structure transfer number (ξ) to quantify the effect of the large-scale vortices on inter-channel mass transport (θ).

$$\theta = \frac{\xi - 1}{\xi} \tag{4-3}$$

where $$\xi = \frac{T}{\tau^{cross}} \tag{4-4}$$

with $$T = \frac{1}{2}\frac{L^{str}}{(v^{str} - v_{gap}^{avg})} \tag{4-5}$$

and $$\tau^{cross} = \frac{D}{v^{cross}} \tag{4-6}$$

where

θ = mass transfer by individual structure, (-)

ξ = structure transfer number, (-)

T = residence time of fluid in a structure, (s)

L^{str} = streamwise structure length, (m)

v^{str} = streamwise structure velocity, (m/s)

v_{gap}^{avg} = average streamwise fluid velocity in the gap region, (m/s)

v^{cross} = cross velocity in the gap region, (m/s)

τ^{cross} = time taken by fluid to cross the gap of depth D in lateral direction. (s)

Their model shows a good agreement with experimental findings for Re_{ch} ranging from 1,000 to 10,000. The shortcoming of this model, however, is that an estimate of the structure transfer number is subject to the availability of experimental data, rather than known macroscopic flow field parameters such as the flow rate and the geometry of the channel.

At present, the crossflow mixing process in rod bundles has not yet been completely explained due to the incomplete understanding of the role of large–scale coherent vortices in the mixing process and the degree by which the geometry of the gap region affects these

vortices and/or mixing. These shortcomings demand for a systematic and comprehensive study on the flow patterns in a tube bundle and their contribution to the crossflow mixing as a function of Re_{ch}, gap geometry (in particular) and channel geometry (in general). As discussed in Chapters 2 and 3, most of the flow patterns identification work in the past was for turbulent flows only. The work done on inter-channel mixing also relates to turbulent flows, since, the mixing experiments generally followed the same flow patterns identification studies. In this chapter, the results of crossflow mixing will be presented for a complete range of Re_{ch}, covering laminar as well as turbulent flows. With the help of our findings in this chapter and the preceding chapters, we will show the significance of both the gap geometry and the large-scale coherent vortices, with respect to crossflow mixing. Furthermore, we will also quantify the contribution of large-scale vortices, over turbulent mixing, towards the crossflow mixing.

4.2. Test section and experimental techniques

For the present study, the tracer injection-detection technique (discussed in detail below) had been employed to mimic the crossflow mixing of heat/scalar in a tube bundle geometry. Measurements were performed in all three setups of compound channels considered for PIV crossflow measurements in Chapter 2, i.e., R-3, C-2 and C-3. In addition, compound channels with a rectangular gap of 2.0 mm spacing, henceforth test section R-2, was also included in these experiments. Table 4-1 lists the geometric parameters and flow conditions for the test sections considered for the mixing experiments. The tracer injection technique used in compound channels is based on the concept that the change in the concentration of a tracer, injected in one of the channels at some upstream location, at both outlets gives a measure of the crossflow mixing.

Table 4-1 Geometric parameters and flow conditions for test sections used in mixing experiments

*Test section	Min. gap spacing (mm)	Total cross-sectional hydraulic diameter (mm)	Gap hydraulic diameter (mm)	Re_{ch} range
R-2	2.0	22.2	4.0	830 – 19,928
R-3	3.0	22.7	6.0	837 – 20,093
C-2	2.0	23.7	6.6	859 – 20,617
C-3	3.0	24.2	8.2	865 – 20,767

**R for rectangular and C for curved gap shapes, the digit represents the minimum gap spacing (S) in mm*

Lexmond *et al.* [16] used acetic acid as a tracer and measured the pH values of fluid at the outlets to quantify the crossflow mixing. The walls of the test section used by

Lexmond *et al.* [16] comprised of glass and a metallic base plate. In our case, the walls of the test sections were made of Perspex and PVC. Since acid has a potential of reacting with Perspex/PVC, that might cause distortion in the test section walls, this posed a limit on use of acid as a tracer. Therefore, it was decided to use a sodium chloride (NaCl) solution as a tracer material and monitor the change in the impedance, in ohms (Ω), of the fluid at the outlets in order to quantify the crossflow mixing.

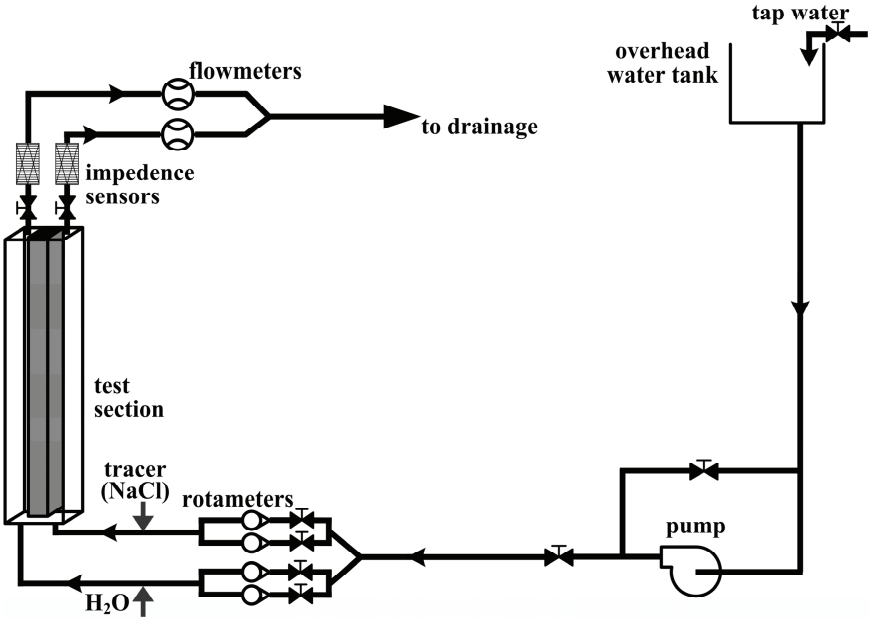

Figure 4-2: Experimental flow loop used for tracer injection experiments.

The flow loop used for PIV experiments, as shown in Figure 2-6, was modified according to Figure 4-2 in order to lead the outgoing water from the test section to the drainage instead of recirculating it. Furthermore, two tracer injection points, 500 cm upstream to the inlets, and two impedance measuring sensors, 40.0 cm downstream to the outlets, of the test section were added. The NaCl solution was injected in one channel and an equal volume flow rate of water in the other channel by using a syringe pump. Injection of same quantity of fluid in each channel minimized the inter-channel flow gradient effect on the crossflow mixing. The volume flow rates of the injected NaCl solution and water in each channel were typically 0.1% of the total flow rate in the test section.

4.2.1. Impedance measuring sensors

Figure 4-3 shows a streamwise, cross sectional view of an in-house fabricated fluid impedance measuring sensor. The sensor was made from a commercial plumbing brass

T-junction of 22.0 mm in diameter. The walls of the T-junction acted as one electrode while a 15.0 mm diameter brass bar, fixed in middle of the straight leg of the T-junction, acted as a second electrode. The brass bar was kept in place by an electrically insulated lead through the cross leg of the T-junction. The tubing to and from the sensor was made of non-conducting PVC. The impedance of the fluid was measured in the concentric region formed in the straight leg of the T-junction due to the presence of the brass bar. The average response time of the sensor estimated from the change in the impedance during the passage of air bubbles between the sensor electrodes was found to be 60.0 ms. This time is sufficient to record the change in the tracer concentration due to crossflow mixing over the effective length of the sensors for all Re_{ch}. The data rate varies over a range of 4.0 – 13.0 Hz, depending upon the Re_{ch}. For injection of tracer from a 60.0 ml syringe, the minimum and maximum integration time was 30 to 1000 sec. for high and low flow rates, respectively. Within this integration time, the standard deviation for all set of measurements was found to be less than ± 1.0 m Ω.

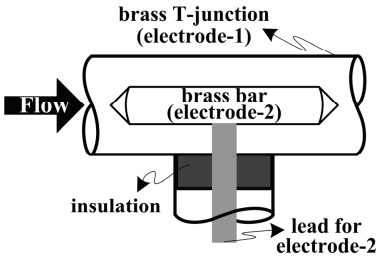

Figure 4-3: Streamwise cross sectional view of the impedance measuring sensor.

Calibration curves shown in Figure 4-4(a) was used to relate the NaCl concentration (C) in water with the measured impedance (Z). A well-behaved function having a non-linear correlation between Z and C can be noticed from this figure. A fourth order polynomial was found to be the best-fitted curve. The non-linearity can be attributed to the chemical composition of the water, temperature variations and depositing of scales on the surface of the electrodes due to the electrolysis. These factors also cause lack of reproducibility of measurements, since the experiments spans over a number of days. To overcome this problem prior to the mixing measurements, a calibration curve of the impedance versus the NaCl concentration was determined on a daily basis.

The tracer transfer across the channels through the gap region, θ^{exp}, was determined using Equation (4-7):

$$\theta^{exp} = \frac{C_2^{out}}{C_1^{out} + C_2^{out}} \tag{4-7}$$

where the subscript 1 refers to channel-1, in which the tracer was injected, and the subscript 2 refers to channel-2 being the one without the tracer injection. All the experiments were carried out at ambient conditions assuming that the water properties remain unchanged by

the addition of the tracer. Figure 4-4(b) shows an example of impedance measurements carried out for R-3 at bulk and tracer flow rate of 2.0 m^3/hr and 0.002 m^3/hr, respectively.

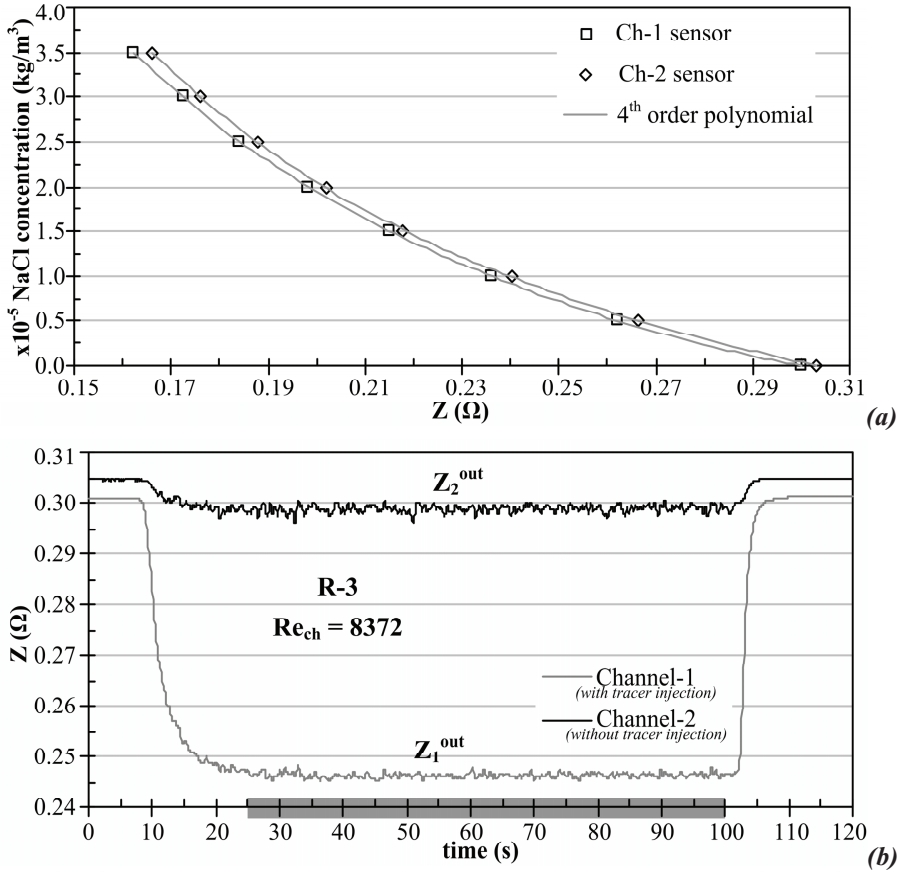

Figure 4-4: (a) Calibration curves for impedance sensors at channel 1 and 2 outlets. Solid grey line is the 4th order fitted polynomial. (b) An example of change in the impedance (Z) of fluid at the outlets of R-3 due to crossflow mixing of tracer injected in channel-1. Grey bar on the abscissa represents the integration time.

4.3. Experimental results

Based on the crossflow findings for compound channels in Chapter 2 some of the observations are as follows:

- the region influenced by the gap is bounded between x=±D/2 (Figure 2-5);

- the flow in the gap region consists of a crossflow (u^{rms}) and a streamwise flow;
- based on the mixing layer theory, the physics of the structures is governed by the streamwise flow in the gap and the channel region;
- the coherent structures, being a source of u^{rms}, contribute towards the crossflow mixing (θ^{exp}), e.g., by the process of entrainment.

From these observations, the dependence of crossflow mixing on the following parameters is envisaged:

(a) Transport time of tracer in the gap and the channel regions

Considering the entrainment of tracer in one structure, there are two possibilities:

- Tracer leaves the structure and is transported ("pushed") from one channel to the other by the cross velocity pulsations through a gap of depth D. The time taken by this uni-direction movement of tracer from one channel to the other (T^{cross}) can be estimated as:

$$T^{cross} = \frac{D}{u^{rms}} \tag{4-8}$$

where u^{rms} = root mean square of cross velocity pulsations in the gap region (a measure of crossflow)

- Tracer remains trapped within the structure and leaves the channel without being transported to the other channel. In this case, the exit time of the tracer to leave the channel (T^{ex}) without undergoing the inter-channel transport can be estimated as:

$$T^{ex} = \frac{L}{v^{str}} \tag{4-9}$$

where L = streamwise length of the active gap region
v^{str} = streamwise structure velocity

In other words T^{ex} is the time available for tracer to undergo crossflow mixing by structures. For $T^{cross} << T^{ex}$, the crossflow mixing of a tracer by structures is highly probable and can be considered as independent of the exit time of tracer.

(b) Gap hydraulic diameter

Based on the mixing layer concept, in compound channels the adjacent high velocity and low velocity streams in the channels and the gap regions, respectively, govern the physics of the coherent structures. Therefore, the dynamics of the coherent structures also depend upon the geometric parameters affecting the flow behavior in the gap/channel

region. The flow area and the wall friction determined by a gap region to the streamwise flow constitute the gap geometry effect on the coherent structures and in turn on the crossflow mixing. Keeping in view these, gap hydraulic diameter (D_h^{gap}) seems to be a plausible geometric parameter affecting the crossflow mixing, since, by definition the hydraulic diameter reflects the cumulative wall friction and flow area effect on fluid flow.

(c) Gap shape

The gap shape defines the change in gap cross sectional flow area between $x \leq \pm D/2$ and x=0.0. For example, rectangular and curved shaped gaps represent a uniform and gradually changing flow area regions, respectively. A curved shaped gap, compared to a rectangular one, allows a deeper access of tracer from the channel region into the gap region. In other words, a gap shape determines the location of the boundary between the high velocity (channels) and the low velocity (gap) regions. Consequently, there is a decrease in the effective depth of the gap (D) which further leads to a decrease in T^{cross} and an increase in crossflow mixing, for a gap having finite streamwise length. The inflection point on a time averaged streamwise velocity profile could be a good measure to see the 'intrusion' of the channel fluid into the gap region. The selection of a higher and/or lower value for S and D, respectively, might be a solution to include the gap shape effect on crossflow mixing. For example, instead of defining S as a minimum gap spacing, a value of S between x=0.0 and x=D/2 could be a good choice.

(d) Turbulent mixing

For a turbulent flow in the gap region, the turbulent mixing contribution towards crossflow mixing (besides coherent structures) cannot be neglected. This issue is further discussed in §4.4.

Figure 4-5 presents the dependence of tracer transfer (θ^{exp}) from channel-1 to channel-2 on Re_{ch} for test sections R-2, R-3, C-2 and C-3. The inter-channel tracer transfer, calculated using Equation (4-7), is plotted as a percentage of the total amount of tracer injected in channel-1. For comparison, the results of Lexmond *et al.* [16] for R-3 are also plotted. For all test sections, the crossflow mixing, i.e., inter-channel tracer transfer (θ^{exp}), shows an increasing trend from Re_{ch} = 1000 up to 6000 and then becomes almost constant for higher Re_{ch}.

Re_{ch}>6000

For each test section, crossflow mixing tends to flatten for Re_{ch}>6000, a trend that is comparable with the streamwise structure length and cross velocity pulsations (u^{rms}) behavior for this range of Re_{ch} as shown in Figure 2-20 and 2-21, respectively. Based on the

cross velocity pulsations (u^{rms}) in the gap region in Figure 2-21, we would expect a higher crossflow mixing for C-2 than for C-3, because of the higher values of u^{rms} in C-2 than in C-3. Figure 4-5, however, shows the opposite, indicating that not merely the cross velocity pulsations in the gap region, but other parameters, as discussed in the preceding paragraph, also effect crossflow mixing.

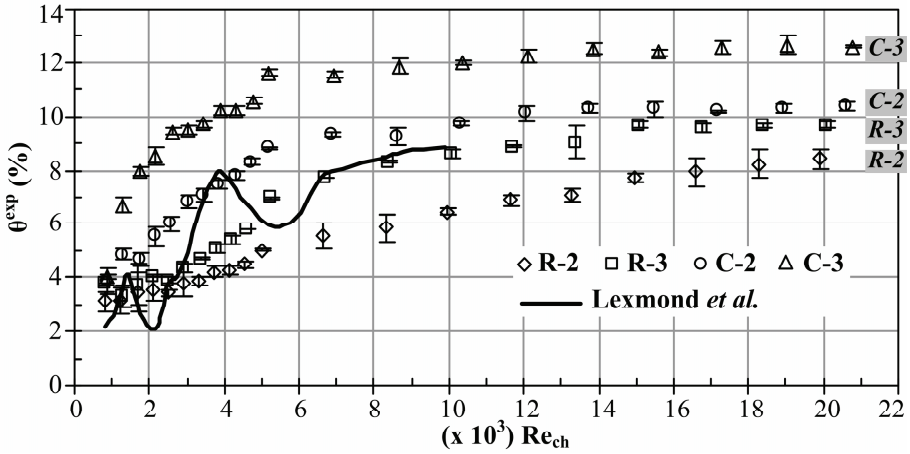

Figure 4-5: Tracer transfer, in percentage of total injected, from channel 1 to channel 2 for test sections R-2, R-3, C-2 and C-3. The plot also shows the results of Lexmond *et al.* [16].

For Re_{ch}>6000, the influence of other parameters, beside u^{rms}, on crossflow mixing (θ^{exp}) is as follows:

- It is found that $T^{cross} << T^{ex}$ (T^{cross}≈10-17 % of T^{ex}) for all gap geometries, indicating a high probability of inter-channel tracer transfer once entrained into a structure. This shows a weak dependence of crossflow mixing on T^{cross} for this range of Re_{ch}.

- The dependence of crossflow mixing on D_h^{gap} is eminent from Figure-4-5, i.e., θ^{exp} increases with increasing D_h^{gap}. Furthermore, comparable values of D_h^{gap} for a rectangular gap (6.0 mm for R-3) and a curved gap (6.6 mm for C-2) give comparable values of θ^{exp}, as shown in Figure 4-5.

- The gap shape effect on the crossflow mixing is not significant for this range of Re_{ch}, since, for all cases the inflection point was found to be located at x≈±D/2 (Figure 2-18). As discussed in Chapter-2, for Re_{ch}>6000, the flow in the gap region for all gap shapes is mainly influenced by the near gap flat wall resulting in a negligible gap shape effect. However, in a tube bundle geometry (Chapter 3) the

gap shape effect is clearly indicated by the inflection points located at $x<\pm D/2$. Therefore, for a tube bundle geometry the gap shape effect on crossflow mixing might be substantial as compared to C-2/C-3.

- From approximated gap Reynolds numbers (Re-I in Figure 2-11) the contribution from turbulent mixing towards the crossflow mixing is anticipated. An additional study to quantify this contribution will be presented in §4.4.

$Re_{ch}<6000$

- For this range of Re_{ch} the T^{cross} is also found to be less than the tracer exit time (T^{ex}); $T^{cross}\approx$8-14 % of T^{ex}.

- Similar to $Re_{ch}>6000$, the dependence of the crossflow mixing on D_h^{gap} is also visible from Figure 4-5 for $Re_{ch}<6000$.

- In this range of Re_{ch}, the effect of the shape of the gap region on the crossflow mixing is more prominent. For example, the values of θ^{exp} for R-3 (rectangular gap) and C-2 (curved gap) are not as comparable as found for $Re_{ch}>6000$, although D_h^{gap} in both cases is approximately the same. Higher values of θ^{exp} for C-2 are due to a larger access of the channel fluid to the gap region for C-2 than R-3, visible from the location of the inflection points on the streamwise velocity profile (Figure 2-18).

- For $Re_{ch}<6000$, the crossflow mixing is expected to be dominated by molecular diffusion, since the gap region has been identified as a laminar flow zone for $Re_{ch}<6000$ (see Re-I in Figure 2-11). The process of diffusion solely, however, cannot account for the existence of significant values of θ^{exp} found for this range of Re_{ch} (particularly for $Re_{ch}<2000$). For $Re_{ch}<2000$ the increasing behavior of θ^{exp} shown in Figure 4-5 is compatible with the trend of the cross velocity pulsations (u^{rms}) in the gap region (see Figure 2-21). The presence of coherent structures, being the source of the u^{rms}, leads to the conclusion that for $Re_{ch}<2000$ the crossflow mixing is dominated by coherent structures rather than molecular diffusion. For $2000<Re_{ch}<6000$, θ^{exp} and u^{rms} depict an increasing and a decreasing trend, respectively (see Figure 2-21 for u^{rms}), which is, at first sight, contradictory. For this range of Re_{ch}, due to transition flow in the channels, turbulent mixing contribution towards the crossflow mixing comes into play, particularly near the edges of the gap ($x=\pm D/2$). This turbulent mixing contribution from the channels probably compensates the decrease in the u^{rms} and results in a net increase of θ^{exp}.

From Figure 4-5, at low Re_{ch} crossflow mixing (θ^{exp}) follows a rather irregular behavior in case of Lexmond *et al.* [16]. This irregular behavior is due to the location of the injection points within the test section, i.e., near the wedge shape flow splitter, close to the inlet (see Figure 2-5). This setting results in a Reynolds number dependent streamwise, and consequently a cross-stream, mixing distance from the injection point before the tracer becomes well mixed with the channel fluid. Existence of these mixing distances and the location of the gap region lead to a time lag before the tracer becomes available near the gap edge (x=D/2) for crossflow mixing, see the cross-sectional view of the test section in Figure 2-5. Uncertainties associated with this time lag and the mechanism of crossflow mixing by coherent structures, i.e. entrainment, results in as an irregular behavior of θ^{exp} in Figure 4-5. The location of the tracer injection points in the current setups, i.e. 500 cm upstream to the inlets, ensured a well-mixed tracer at the entrance of the test sections. This setting eliminates the mixing distance uncertainty and results in a relative smoothening of θ^{exp} for $Re_{ch}<6000$.

4.4. Inter-channel mixing mechanisms

Once the flow in the gap region deviates from laminar to turbulent, the question arises to what extend turbulent mixing and the coherent structures contribute to the crossflow mixing. To resolve this issue an additional study was carried out over a broad range of gap hydraulic diameters (D_h^{gap}). For these experiments, the test section with a rectangular gap (R-2/R-3) was used. The rectangular gap was chosen because it results in a sharp and well-defined channel-gap interface.

From the mixing layer theory, in compound channels the near gap coherent structures are subject to the presence of adjacent low (gap) and high (channel) streamwise velocity regions. The coherent structures seize to exist when the difference between the gap and the channel streamwise velocity approaches zero. From this point of view, the presence/absence of coherent structures in compound channels can be manipulated by changing D_h^{gap}, i.e., by changing the flow conditions in the gap region. For the present study, the change in D_h^{gap} was implemented by changing the gap spacing (S). Turbulent mixing in the gap region was ensured by selecting Re_{ch}=10,000 for all D_h^{gap}. This selection of Re_{ch} was based on Figure-2-11, which showed that for R-3 (S=3.0 mm) at Re_{ch}=10,000 the approximate gap Reynolds number (Re-I) had a value of 2000.

Table 4-2 lists the operational parameters for various gap spacing considered. The study was performed in two steps:

- PIV measurements – for verifying the presence or the absence of coherent structures at a particular D_h^{gap},

- Crossflow mixing experiments using the tracer injection method – to observe a change in crossflow mixing (θ^{exp}), if any, due to presence/absence of coherent structures.

In §4.3., D_h^{gap} has been identified as the most important parameter influencing crossflow mixing for high Re_{ch}. For this reason, the results in the following sections will be presented as a function of both S and D_h^{gap}.

Table 4-2 Operational parameters for various gap spacing (Re_{ch} = 10,000).

Gap spacing (mm)	Gap hydraulic diameter (mm)	Channel cross sectional area (cm^2)	Channel hydraulic diameter (cm)	V_{bulk} (cm/s)
23.4	46.8	19.35	3.44	28.71
21.4	42.8	18.93	3.31	29.35
19.4	38.8	18.51	3.18	30.02
17.4	34.8	18.09	3.06	32.73
15.4	30.8	17.67	2.93	34.07
13.4	26.8	17.25	2.82	35.48
9.4	18.8	16.41	2.6	38.52
8.4	16.8	16.20	2.54	39.33
7.4	14.8	15.99	2.49	40.16
6.4	12.8	15.78	2.44	41.01
5.4	10.8	15.57	2.39	41.88
4.4	8.8	15.36	2.34	42.78
3.0	6.0	15.06	2.27	44.26
2.0	4.0	14.85	2.22	44.88
1.0	2.0	14.64	2.17	46.03

4.4.1. Gap spacing variation - PIV measurements

Coherent vortices in a mixing layer result in low frequency cross velocity oscillations. The presence of coherent vortices appears as a peak in the one dimensional energy spectrum [55] of a cross velocity time signal measured at a point in the flow filed. For the present study, the same concept has been applied to the cross velocity time signal at the center of the gap, obtained from PIV, to verify the presence of coherent structures at different S. The PIV sampling rate ranges from 250 to 360 Hz. for different V_{bulk}.

Figure 4-6(a) shows the APSD plot of the gap cross velocity signal for S=5.4 mm, 8.4 mm and 9.4 mm. Coherent structures first appear at S=8.4 mm, indicated by a peak in the APSD plot persists for S<8.4mm. No peak is observed for S=9.4 mm, so there are no

coherent structures at this gap spacing. Apparently, coherent structures are generated for gap spacing smaller than 9.4 mm.

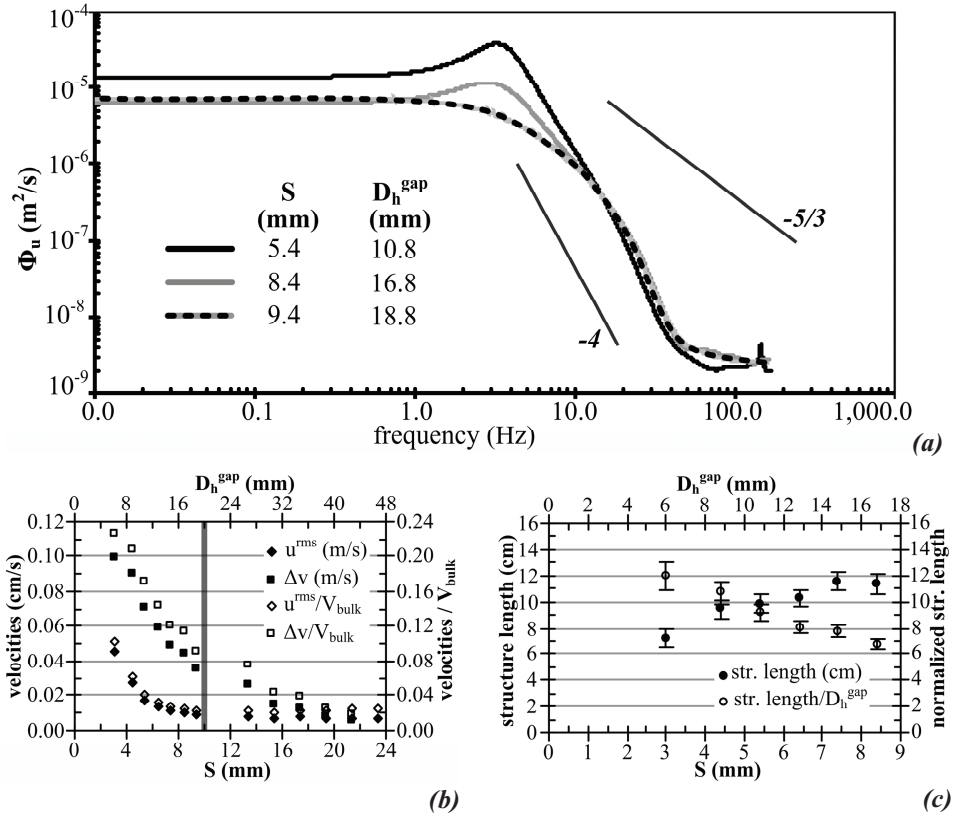

Figure 4-6: (a) APSD of the cross velocity component at the center of the gap (x=0, y=0, z=0) for gap spacing of S=5.4 mm, 8.4 mm and 9.4 mm. (b) Absolute and normalized RMS of the cross velocity pulsations (at origin) and Δv versus gap spacing and gap hydraulic diameter. Moving from high to low S, the thick vertical line marks the first appearance of the coherent structures. (c) Absolute and normalized streamwise structure length. Re_{ch} = 10,000.

Visual PIV data has shown the appearance of large-scale vortices even at gap spacing greater than 8.4 mm. These structures, however, lack coherence since no dominant frequency appears in the APSD plot of cross velocity signal. Hence, we may conclude that at a certain gap spacing the coherence of the structures clearly disappears (in our case S>9.0mm). An interesting thing to note is the slope of -4 in the inertial range of the APSD plot for S=5.5 mm, indicating a two-dimensional nature of the coherent structures [57]. The slope of the curve in the inertial range seems to approach -5/3 for S≥8.4 mm, signifying a

dominance of turbulent mixing. An increase in cross velocity pulsations (u^{rms}), at the middle point in the gap (x=0, y=0, z=0), also confirms the appearance of coherent structures at S≈9.0 mm as shown in Figure 4-6(b). Figure 4-6(b) also depicts plot of the difference between the minimum (in the gap region) and the maximum (in the channel region) stream wise velocity, i.e., Δv, as a function of S/D_h^{gap}. Figure 4-6(c) shows the change in absolute and normalized streamwise structure length with changing S/D_h^{gap}. Comparing Figure 4-6(b) and Figure 4-6(c) it is apparent that with increasing S/D_h^{gap}, Δv decreases causing a corresponding increase in the absolute streamwise structure length and a decrease in the u^{rms}. This finding supplements the results of the compound channels (R-3, C-2, C-3) and the tube bundle geometry, discussed in Chapter 2 and 3.

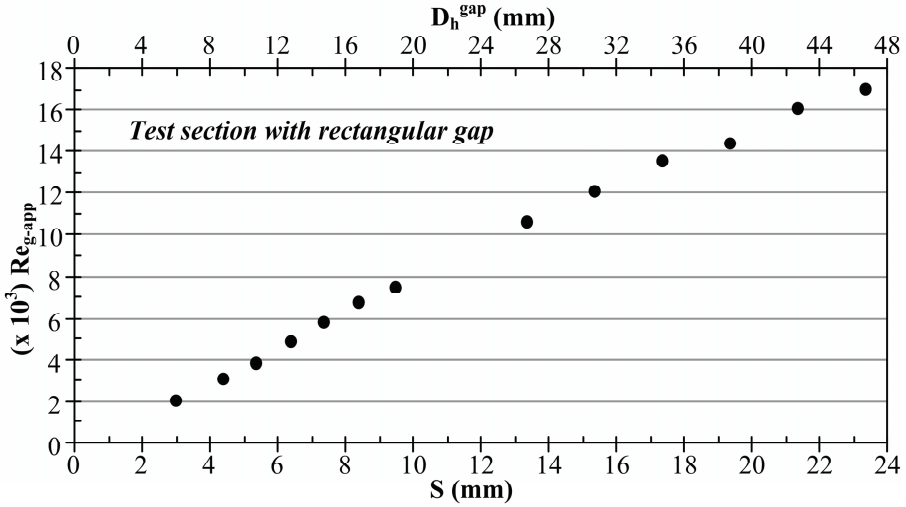

Figure 4-7: Approximate gap Reynolds numbers ($Re_{g\text{-}app}$) as a function of gap spacing and gap hydraulic diameter. $Re_{g\text{-}app}$ is based on the gap hydraulic diameter and the streamwise gap average velocity obtained from PIV measurements. For all measurements, Re_{ch} = 10,000.

Figure 4-7 depicts a plot of the approximate gap Reynolds numbers, henceforth $Re_{g\text{-}app}$, as a function of gap spacing (S) and gap hydraulic diameter (D_h^{gap}). $Re_{g\text{-}app}$ is based on the gap hydraulic diameter and the streamwise gap average velocity along a line extending from x=-D/2 to x=D/2 in a PIV measurement plane. The $Re_{g\text{-}app}$ here is underestimated as compared to the true gap Reynolds number, because the velocity based on the total flow area of the gap region would be somewhat higher than the one approximated from the PIV measurements. For S=3.0 mm, however, $Re_{g\text{-}app}$≈2000 is quite close to the true gap Reynolds number, since the 1.0 mm thick laser sheet covers most of the near laminar velocity profile in the gap region. Assuming $Re_{g\text{-}app}$=2000 as an upper limit

for existence of laminar flow, for S>3.0 mm a transition from laminar to turbulent flow is expected in the gap region.

4.4.2. Tracer injection experiments

The contribution of the coherent structures towards the crossflow mixing over the turbulent mixing has been investigated by the tracer injection method for the gap spacings (or D_h^{gap}) listed in Table 4-2. Figure 4-8 depicts the inter-channel tracer transfer, in percent of total injected, versus the gap spacing and the gap hydraulic diameter.

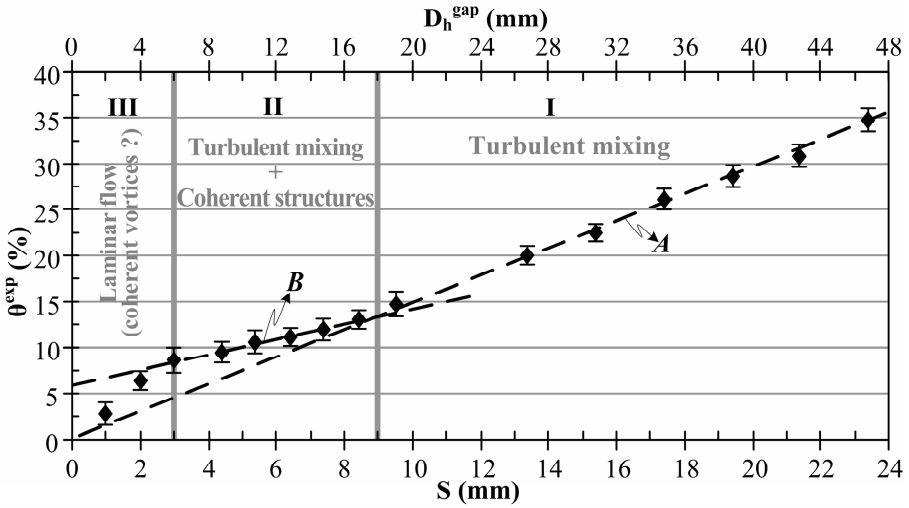

Figure 4-8 Inter-channel tracer transfer as a function of various gap spacing, for constant Re_{ch} = 10,000. For comparison purposes, gap hydraulic diameter is shown on secondary x-axis. The dashed line represents a linear fit to the data points.

S>9.0 mm (D_h^{gap}>18.0 mm)

From PIV measurements, § 4.4.1., we found the existence of turbulent flow in the gap region and the absence of near gap coherent structures for S>9.0 mm. Hence, we can assume that for S>9.0 mm, designated as Region-I in Figure 4-8, the crossflow mixing is due to turbulent mixing alone. As expected, a linear fit to the measured data in Region-I, line A, extends to zero turbulent mixing when the gap spacing approaches zero.

3.0 mm<S<9.0 mm (6.0 mm<D_h^{gap}<18.0 mm)

The appearance of coherent structures at S≈9.0 mm causes a decrease in the slope of the line A, indicating a positive contribution of coherent structures towards the crossflow mixing, in addition to turbulent mixing. In Figure 4-8, a change in the slope of the line A is made visible by a linear fit, line B, to the measured data in the range 3.0 mm≤S≤8.4 mm.

The lower limit of Region-II is selected based on the plot of $Re_{g\text{-}app}$ vs. S (Figure 4-7), depicting existence of almost a transition flow at S=3.0 mm. Region-II in Figure 4-8, therefore, spans over the gap spacing of 3.0 mm to 9.0 mm, characterized by the crossflow mixing due to the turbulent mixing and the coherent structures. For S=3.0 to 9.0 mm, the existence of coherent structures is eminent from the PIV measurements presented in §4.4.1.

As a first approximation, the contribution of coherent structures towards crossflow mixing, in the presence of turbulent mixing, is found to be nearly 48% of θ^{exp}. This value is estimated from the ordinate values of lines A and B at S=3.0 mm, see Figure 4-8. Remind that S=3.0 mm has been identified as lower and upper limit of regions II and III, respectively.

S<3.0 mm (D_h^{gap}<6.0 mm)

For S<3.0 mm, designated as Region-III in Figure 4-8, the tracer transfer decreases due to a decrease in D_h^{gap} and approaches zero, as expected. The decrease in tracer transfer corresponds to an inefficient mechanism for crossflow mixing in Region-III. Based on $Re_{g\text{-}app}$, see Figure 4-7, the expected laminarization of the flow in the gap region might be the reason behind this inefficient crossflow mixing. Due to the absence of PIV data for S<3.0 mm, the question of the existence of coherent structures and their probable role in crossflow mixing in Region-III remains unanswered. In Chapter 2 it has been shown that for a very low $Re_{g\text{-}app}$ coherent structures do exist. This condition, however, was imposed by a decrease in the inlet flow rate rather than by decreasing the D_h^{gap}, as in the current situation. Therefore, a qualitative conclusion cannot be drawn here.

4.5. Conclusions

Experimental studies have been carried out to investigate the crossflow mixing in compound rectangular channels connected by a rectangular and a curved gap region using tracer injection experiments. An additional study was performed to investigate the contribution of coherent structures and turbulent mixing towards the crossflow mixing. Based on the results of these measurements the following conclusions are drawn:

- For Re_{ch}<2000, significant values for the crossflow mixing exist even in the presence of laminar flow in the gap and the channel regions. Since the molecular diffusion alone cannot account for crossflow mixing of this magnitude, it is obvious that coherent structures dominate crossflow mixing over molecular diffusion.

- For 2000< Re_{ch}<6000, a decrease in u^{rms} in the gap region is compensated by the turbulent mixing contribution from the transition flow in the channels, resulting in a net increase of crossflow mixing.
- For Re_{ch}>6000 the flow in the gap and channel region is turbulent. The values of crossflow mixing (indicated by tracer transfer) flatten out for this range of Reynolds numbers, a trend consistent with the streamwise structure length and u^{rms} in the gap region. This finding indicates the influence of coherent structures besides turbulent mixing on crossflow mixing. An additional study verified this finding, suggesting that coherent structures contribute positively to the crossflow mixing besides turbulent mixing.
- Crossflow mixing is found to be influenced by the gap hydraulic diameter for the whole range of Reynolds numbers. Besides the gap hydraulic diameter, crossflow mixing is also found to be effected by the shape of the gap region, particularly for laminar flows in the gap region (Re_{ch}<6000). From these observations in the gap regions defined by a rectangular (R-3) and a curved duct (C-2/C-3), effect of gap shape in a tube bundle (formed by two curved surfaces) on crossflow mixing is anticipated.
- For small values of gap spacing, S<3.0 mm and Re_{ch}=10,000, crossflow mixing decreases and tends to zero due to a decrease in gap hydraulic diameter. Laminarization of the flow in the gap region has been identified as a probable reason for this inefficient mixing mechanism. Under these conditions, the crossflow mixing is supposed to be only due to coherent structures, if they exist.

These results, along with the findings of the flow pattern studies, will be used during the modeling phase of the crossflow mixing (Chapter 5).

5

A model for crossflow mixing

As mentioned in Chapter 1, the objective of this work is to describe and predict the crossflow mixing in a tube bundle geometry. Keeping in view the relevancy of flow phenomena in compound channels and a tube bundle as described in Chapter 3, in this chapter a model of crossflow mixing in compound channels, based on the concept of coupled continuous stirred tanks (CST), is proposed.

Most of the previous research work on the role of large-scale coherent vortices in transporting a passive scalar is related to the category of free shear layers, such as bluff body wakes and plane mixing layers [58, 59, 60, 61]. Furthermore, the emphasis is on the scalar mixing within a vortex and its transport in the streamwise direction rather than the cross-stream direction. Although the channel-gap flow field in the test sections C-2, C-3 and R-3 resembles a free, double shear layer formed in the wake behind a bluff body, some differences are eminent in the results of the measurements presented in Chapter 2. For example, in compound channels a shear layer of uniform lateral width in the streamwise direction is found resulting in coherent vortices and cross velocity pulsations of constant streamwise length and intensity, respectively. Hence, transport of passive scalar in free shear layers is not of direct relevance to the cases of compound channels. However, the following observations are relevant to both cases (free shear layer or compound channels):

- A coherent vortex acts as a ‘mixing device’ for fluids/passive scalar (if applicable) after entrainment. This is particularly valid at high Reynolds numbers due to the turbulence in a vortex.

- After the entrainment of a fluid in a coherent vortex, there is a characteristic delay time prior to release of this entrained fluid to the outer flow (the "residence time").

From these observations and the experimental results, a model for crossflow mixing in compound channels is proposed, strongly based on suggestions by Rohde [62]. A detailed description of the proposed model follows.

5.1. Modeling

Keeping in view the experimental results presented in the preceding chapters, a crossflow mixing model based on the idea of transport of a passive scalar/tracer through continuously stirred tanks (CST) is presented.

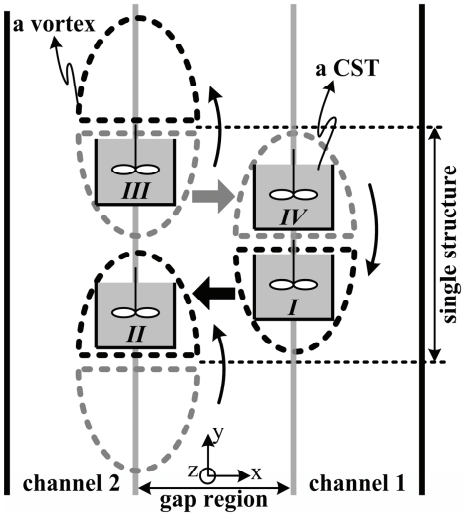

Figure 5-1: Conceptual picture of crossflow mixing model based on CST's.

It is assumed that two CST's represent a large-scale vortex, each carrying out lateral transport of tracer in alternating directions. As a result, a set of four CST's represents a coherent structure in the gap region, as shown in Figure 5-1. The spanwise tracer transport from channel 1 to 2 is through CST I and II, while tracer transport from channel 2 to 1 is through CST III and IV. The mass balance equation for this model is derived in Appendix A. The derivation is based on following assumptions:

- In both channels the tracer is perfectly mixed with the water in the xz-plane;.
- No absorption or reaction of tracer takes place;

- The streamwise velocities and flow areas of both the channels are equal.

Considering the injection of tracer in channel 1, the fraction of tracer transferred to channel 2 (θ) quantifies the inter-channel crossflow mixing in compound channels, see Chapter 4, and is given as:

$$\theta = \frac{\text{tracer concentration at outlet of channel}-2}{\text{total tracer injeced in channel}-1} \tag{5-1}$$

The CST based model for the θ, derived (see Appendix A) in terms of properties of the coherent structures and compound channels geometric parameters is:

$$\theta^{str} = \frac{1}{2}\left[1-\exp\left(-\frac{u_{eff}^{rms} S}{A_{ch} V_{bulk}}\left(L-\frac{v^{str}\tau}{2}\left(e^{\frac{-2L}{v^{str}\tau}}-4e^{\frac{-L}{v^{str}\tau}}+3\right)\right)\right)\right] \tag{5-2}$$

where

θ^{str} = θ estimated from the CST based model;

u_{eff}^{rms} = effective crossflow velocity through the gap region;

S = minimum gap spacing;

A_{ch} = one half of the total cross sectional flow area of compound channels;

V_{bulk} = bulk velocity;

L = active streamwise length of the gap region;

v^{str} = streamwise structure velocity;

τ = spanwise residence time of tracer in a coherent vortex, i.e., after entrainment the time taken by tracer to cross a coherent vortex in the spanwise direction.

The residence time τ of a CST (and thus for a structure) is estimated as:

$$\tau = \frac{\text{structure volume}}{\text{volumetric flow rate through a structure}} \approx \frac{SWL^{str}}{u_{eff}^{rms} SL^{str}} = \frac{W}{u_{eff}^{rms}} \tag{5-3}$$

where

W = lateral width of a structure taken as the spanwise distance between the center of the gap and the channel region;

L^{str} = measured streamwise structure length.

By assuming laminar flow in the spanwise direction through the gap region and thus a parabolic velocity profile in the z-direction, the effective crossflow velocity is:

$$u_{eff}^{rms} = \frac{2}{3}\ u^{rms} \tag{5-4}$$

where u^{rms} is the root mean square of the measured cross velocity pulsations in the center of the gap region. Figure 5-2 shows a comparison of the measured (θ^{exp}) and the estimated (θ^{str}) inter-channel crossflow mixing (fraction of tracer transferred from channel 1 to channel 2) for test sections C-2, C-3 and R-3 as a function of Re_{ch}. In general, when compared with the experimental values, θ^{str} is over predicted for $Re_{ch} < 6000$ and under predicted for $Re_{ch} > 6000$.

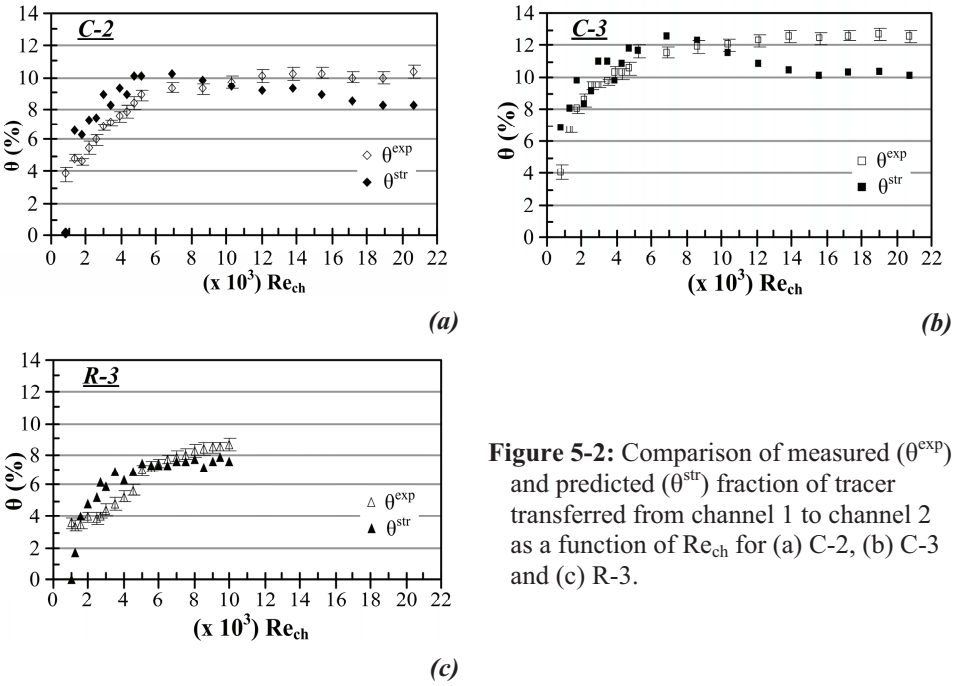

Figure 5-2: Comparison of measured (θ^{exp}) and predicted (θ^{str}) fraction of tracer transferred from channel 1 to channel 2 as a function of Re_{ch} for (a) C-2, (b) C-3 and (c) R-3.

Re_{ch}<6000

In Chapter 2, the flow in the gap region has been identified as laminar for this range of Re_{ch}. Therefore, it is plausible that the assumption of instantaneous mixing of tracer in a CST, used in the derivation of Equation (5-2), does not hold for this range of Re_{ch}. As a result, tracer within a vortex is expected to exist in the form of streaks for a longer period instead of being readily mixed with the bulk of the fluid. In other words, the mixing within a structure is less efficient than predicted by the model since it is based on the idea of coupled CST's. In this sense, Equation (5-3) under predicts τ, resulting in an over predicted θ^{str}.

Re_{ch}>6000

As shown in Chapter 2 a transition from laminar to turbulent flow occurs for this range of Re_{ch}. Experimental results in § 4.4.2. depicted that, at high Re_{ch}, the crossflow mixing is under the influence of both coherent vortices and turbulent mixing (Region II in Figure 4-8). θ^{str} estimated from Equation (5-2), on the other hand, is solely based on the structure characteristics ignoring the contribution of turbulent mixing in the gap region between the structures. It is therefore no surprise that for Re_{ch}>6000 the model under predicts θ^{str} as compared to the θ^{exp}.

Application of the model to the measurements carried out for different gap spacing (S) at a constant Re_{ch} of 10000 (Chapter 4) also verifies this finding. Figure 5-3 shows a comparison of θ^{str} and θ^{exp} for different S in Region II, see Figure 4-8. Recall that for Region II, S=9.0 mm marks the upper limit for the existence of coherent structures and S=3.0 mm marks the lower limit for the presence of turbulence.

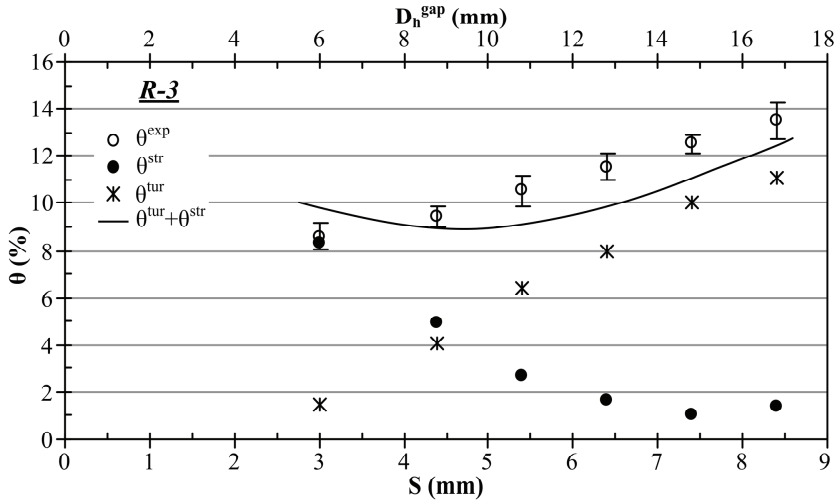

Figure 5-3: Comparison of measured and predicted θ (from structure and turbulence based models) as a function of minimum gap spacing (S) and gap hydraulic diameter (D_h^{gap}) at constant Re_{ch} of 10,000.

In Figure 5-3, as the limit for coherent structures disappearance approaches with increasing S, θ^{str} (calculated based on structure characteristics) decreases. On the other hand, the increasing trend of θ^{exp} suggests that with increasing S the turbulent mixing in the gap region compensates the diminishing contribution of coherent structures towards the crossflow mixing. To verify the contribution of turbulent mixing in θ^{exp} at different S, the

following equation has been derived (see Appendix A-3) to quantify the inter-channel exchange of tracer due to turbulent mixing (θ^{tur}) only:

$$\theta^{tur} = \frac{1}{2}\left(1 - \exp\left(-\frac{2SL\nu_t}{A_{ch}V_{bulk}D}\right)\right) \tag{5-5}$$

where

D = gap depth;

ν_t = turbulent viscosity;

The other parameters have the same definition as in Equation (5-2). The turbulent viscosity is calculated using [63]:

$$\nu_t = 0.09\frac{k^2}{\varepsilon} \tag{5-6}$$

The turbulent kinetic energy dissipation rate (ε) is approximated from the mean streamwise velocity profile obtained from the PIV measurements by using the following equation [64]:

$$\varepsilon = 7.5\nu\overline{\left(\frac{\partial v}{\partial x}\right)^2} \tag{5-7}$$

where ν is the kinematic viscosity of water. The turbulent kinetic energy (k) is estimated by applying Proper Orthogonal Decomposition (POD) to the PIV data at different gap spacing, as explained in Chapter 2. Figure 5-3 depicts the contribution of turbulent mixing towards θ^{exp} with increasing S, calculated from Equation (5-5). As expected, θ^{tur} increases with increasing S. Note that, quantitatively, θ^{tur} has a limited validity due to the estimation of ν_t based on the algebraic correlations, Equation (5-6), and 2D-PIV measurements with a relatively coarse spatial resolution. Nevertheless, the qualitative trend of θ^{tur}, calculated from Equation (5-5), in Figure 5-3 should be considered valid. The crossflow mixing resulting from the total of the structure and the turbulence based models is depicted in Figure 5-3 as a solid line. The sum of θ^{tur} and θ^{str} falls within a band of ±16 % of θ^{exp}, which is fairly good keeping in view the above-mentioned limitations of the turbulence model. For S < 4.0 mm, as the flow in the gap region starts to become laminar, the deviation of the solid line to higher value, as compared to θ^{exp}, is probably due to over predicted ν_t in the turbulence based model. Due to difficulty in predicting ν_t from available experimental data, in the following paragraphs only structure based crossflow mixing model (θ^{str}) is considered. However, with proper estimate of ν_t, the total crossflow mixing (for turbulent flows) can be predicted as sum of crossflow mixing due to structure and turbulence based models, i.e., θ^{str} and θ^{tur} from Equation (5-2) and Equation (5-5), respectively.

In Equation (5-2) two parameters remain undetermined, being the structure velocity (v^{str}) and the cross velocity pulsations in the gap region (u^{rms}). It is desirable to replace these two parameters with some known quantities, such as V_{bulk}. As shown in Figure 5-4(a), the structure velocity is almost linearly related to V_{bulk} in both the laminar and turbulent regions, independent of gap geometric parameters. The expected value of v^{str} for different gap spacing is estimated to fall within ±8.0 % of the measured v^{str}. The spread in v^{str} for different gap spacing is determined from measurements in R-3 at different values of S (Chapter 4). Keeping this in view, the structure velocity is approximated as:

$$v^{str} \approx V_{bulk} \tag{5-8}$$

The cross velocity (u^{rms}), on the other hand, shows no clear link with V_{bulk}, see Figure 5-4(b). However, taking into account the dependency of streamwise structure length and, in turn, u^{rms} on D_h^{gap} (Chapter 2) and assuming a linear relation between u^{rms} and V_{bulk} for each gap spacing, an empirical relation for u^{rms} can be derived as:

$$u^{rms} = \left[0.007\left(D_h^{gap}\right)^{-0.6} \right] V_{bulk} \tag{5-9}$$

Hence the slope of the linear relation between u^{rms} and V_{bulk} becomes smaller for larger gap sizes.

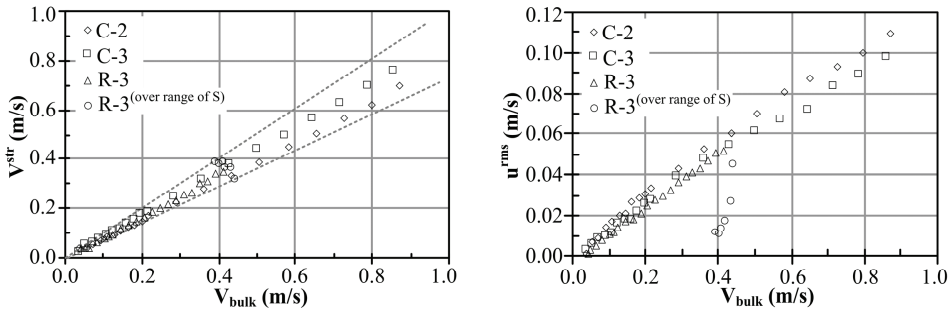

Figure 5-4: Plot of (a) v^{str} vs. V_{bulk} and (b) u^{rms} vs, V_{bulk} for test sections C-2, C-3, R-3 and R-3 with variable gap spacing. Dotted lines in (a) shows the spread in measured v^{str} over a range of S, estimated from the measurements in R-3 at a constant Re_{ch} of 10,000 (Chapter 4).

Figure 5-5 depicts θ^{str} estimated from Equation (5-2) by using these two v^{str} and u^{rms} approximations. On average, θ^{str} calculated by using the modified values of u^{rms} and v^{str} differs from θ^{str} based on the experimental values by 13 % (for Re_{ch}<6000) and 7 % for

(Re_{ch}>6000). Therefore, the use of the modified v^{str} and u^{rms} in Equations (5-8) and (5-9), respectively, seems appropriate for the estimation of θ^{str}.

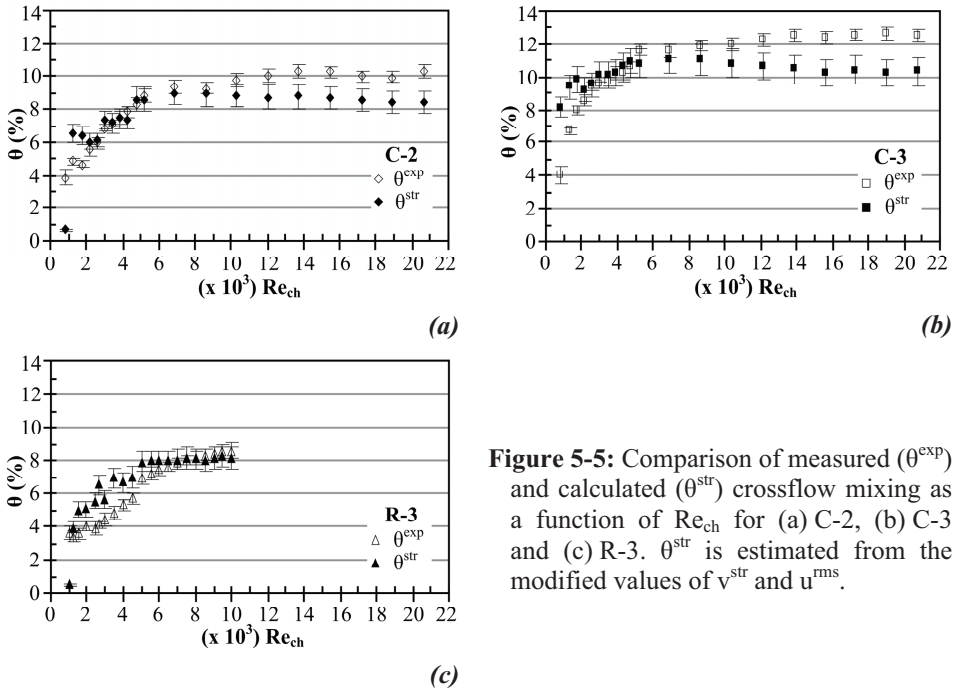

Figure 5-5: Comparison of measured (θ^{exp}) and calculated (θ^{str}) crossflow mixing as a function of Re_{ch} for (a) C-2, (b) C-3 and (c) R-3. θ^{str} is estimated from the modified values of v^{str} and u^{rms}.

As mentioned in § 5.1, the discrepancy in θ^{str} and θ^{exp} for Re_{ch}<6000 is mainly due to the use of the concept of an ideal, i.e., perfectly mixed CST. In addition, θ^{str} in Equation (5-2) is also found to be sensitive to the parameters occurring in the exponent terms, such as τ and L. In the previous, L is taken as the full active length of the gap region. In other words, θ^{str} is estimated assuming that the coherent vortices exist along the full length of the active gap region. In all compound channels test sections, however, two isolated channel inlets are created by inserting a square duct forming a geometry in the beginning of the gap region that resembles a wake behind a thick trailing edge. Unal and Rockwell [65] and Norberg [66] showed that a certain vortex formation length exists for such a wake region, which is a non-linear function of Reynolds numbers. In general, the vortex formation length decreases with increasing Reynolds numbers [64, 65]. Therefore, the effective streamwise length marked by the presence of coherent vortices (L^{coh}) should be less than the actual gap length (L), in particular for low Reynolds numbers. Keeping this in view, the use of L^{coh} (instead of L) in Equation (5-2) results in a corresponding decrease in θ^{str}, possibly improving the model predictions particularly for the laminar gap flow region (Re_{ch}<6000).

5.2. Conclusions

An inter-channel crossflow mixing model based on experimental findings for compound channels and a tube bundle has been proposed by using the concept that a pair of continuous stirred tanks can replace half of a large–scale coherent structure. The model is valid for a large range of Re_{ch}, thus covering laminar, transitional and turbulent flows in the gap region. The model predicts the inter-channel crossflow mixing using the structure characteristics, i.e., the residence time of tracer in a structure and the streamwise structure velocity. The residence time of tracer in a structure is approximated as the ratio of the structure volume to the spanwise volumetric flow rate through a structure. By using the experimental observations, the model is finally evaluated in terms of known flow and geometric parameters, such as the fluid bulk velocity and the gap hydraulic diameter.

As compared to the experimental results, the model predictions lie within a band of ±20 % of the experimental values for the range of Reynolds numbers studied here. For laminar flow in the gap region, the probable violation of the well-mixed tracer (within a structure) assumption results in an over predicted crossflow mixing as compared to the experimental findings due to an underestimated fluid residence time in a vortex. On the other hand, for turbulent flow in the gap region, although the well-mixed tracer (within a structure) assumption holds, the crossflow mixing is under-predicted since the model does not include the contribution of turbulent mixing. A simple turbulence based crossflow mixing model also verifies this. A use of more refined models for the fluid residence time in large-scale coherent structures and streamwise structure formation length is expected to improve the model predictions.

6

Conclusions and recommendations

The motivation behind this work is to explore the crossflow mixing phenomenon in the core of a nuclear power plant since that plays an important role from the nuclear safety point of view. In the core of a nuclear power plant (with a particular reference to Light Water Reactors (LWR)), the fuel rods are arranged in a square pitched vertical tube bundle geometry. This configuration causes the formation of coherent flow structures that influence crossflow mixing, i.e., the radial mixing, e.g., of heat, energy and vapors (in a boiling water reactor).

The focus of the present work was to explore, in detail, the crossflow mixing phenomenon in a vertical tube bundle geometry over a broad range of Reynolds numbers (≈900 to 22,000). Using water as the working fluid, experiments were performed at ambient conditions in different geometrical configurations to achieve the above-mentioned objective, supported by a few numerical simulations. The geometries considered were compound channels connected by a rectangular gap, compound channels connected by a curved gap and a 4 x 4 tube bundle geometry. Compound channels with a variable gap spacing mimic two interconnected sub-channels of a tube bundle geometry. Flow field measurements were carried out by using Particle Image Velocimetry (PIV) and Laser Doppler Anemometry (LDA) in compound channels and in a tube bundle geometry, respectively. In the tube bundle geometry the problem of refractive index matching, originating by the presence of curved surfaces in the path of the LDA laser beams, was also addressed. The quantification of crossflow mixing in compound channels was achieved by using a sodium chloride (NaCl) solution as a tracer material and by monitoring the change in the impedance of the fluid at the outlets.

The present study showed the existence of large-scale coherent structures in compound channels and a tube bundle geometry for laminar, transitional and turbulent flow regimes. The existence of these structures is subject to a threshold streamwise fluid velocity difference that exists between the channel and the gap regions. These structures enhance the inter-channel mixing of a scalar, such as heat, no matter whether turbulent mixing is present (in the gap region) or absent (laminar flow in the gap region). The augmentation in inter-channel transport of a scalar due to the coherent structures is, however, less than the contribution from the turbulence alone, i.e., without the coherent structures. Secondary flows in compound channels and in a tube bundle geometry do not play a significant role in crossflow mixing. Finally, it has been shown that the fluid flow phenomena occurring in compound channels occur in a tube bundle geometry as well. Furthermore, the spatial and temporal resolution of 2D PIV proved to be very well suited for capturing the large-scale coherent structures.

The more specific conclusions drawn from this study are as follows:

1. Counter rotating, large-scale, coherent structures exist on both sides of the gap region, near the gap-channel interface, for all three types of flow*, i.e., laminar, transitional and turbulent flow. The mechanism of generation of such structures is similar to the mechanism found in free shear layer flows, i.e., the streamwise velocity difference between two parallel adjacent flow streams in the gap and the channel regions. The interface of the low flow (gap) and high flow (channel) regions, however, belongs to the wall bounded shear flow category rather than a free shear flow. It appears that in such a wall bounded shear layer, at a certain flow threshold the shear layer width becomes constant, resulting in a constant structure length in the streamwise direction. As a result, the streamwise structure length decreases with increasing Re_{ch} and becomes almost constant in transitional and turbulent flow regimes.
2. For laminar flows, the average streamwise structure length is a function of
   (i) the streamwise velocity difference between the flow in the gap and the channel regions;
   (ii) the gap hydraulic diameter (defined by the gap region cross-sectional flow area and the wetted perimeter of the gap region).

   For transitional and turbulent flow, the average streamwise structure length becomes independent of this velocity difference and merely varies with the gap hydraulic

* *type of flow – based on Reynolds numbers defined by bulk fluid velocity and the cross-sectional geometric parameters of a setup - Re_{ch}*

diameter. For such flows, the streamwise fluid velocity difference is predominantly influenced by the gap streamwise velocity which, in turn, is dictated by the gap walls friction as a function of the gap hydraulic diameter.

3. Low and high values of crossflow (quantified by the root mean square values of the cross velocity pulsations in the gap region) are associated with relatively large and small streamwise structure lengths, respectively. This finding implies that the coherent structures based crossflow mixing would be less for laminar flow than for transitional and turbulent flows. In addition, crossflow increases with decreasing gap spacing/gap hydraulic diameter. Keeping in view the fact that the crossflow goes to zero as the gap spacing approaches zero, a particular value of the gap spacing exists at which the crossflow mixing is maximal.
4. The ***crossflow mixing*** (i.e., the mixing of a scalar between sub-channels) decreases with increasing streamwise structure length and vice versa. Unlike crossflow, however, crossflow mixing decreases with decreasing gap hydraulic diameter. Taking into account the inter-dependency of crossflow and crossflow mixing on streamwise structure length and the gap hydraulic diameter, logical reasoning dictates the existence of another variable affecting the crossflow mixing. During the modeling phase, this important variable was identified as the residence time of a scalar in a coherent structure. Once the scalar is entrained in a coherent structure, the residence time reflects a characteristic delay time prior to the release of this entrained scalar to the outer flow. During the entrapment of the scalar, the coherent structure acts as a 'mixing device' for a scalar with plain entrained fluid. This is particularly valid at high Reynolds numbers due to the turbulence in a vortex. The residence time of a scalar in a structure is higher for larger structures in comparison with smaller ones, due to the structure volume itself and the fact that the largest structures were found at laminar gap flow conditions. Under the assumption that the tracer is well-mixed within a structure a continuous stirred tank (CST) based crossflow mixing model has been proposed to exploit the concept of tracer residence time in a structure. For laminar flow in the gap region (large streamwise structure lengths), the probable violation of the assumption of well-mixed tracer within a structure poses a constraint on the CST based crossflow mixing model.
5. A study of crossflow and crossflow mixing as a function of gap spacing (S), at a constant channel based turbulent Reynolds number of 10,000 in compound channels with a rectangular gap, leads to the following:
   (i) For large gap spacing, i.e., $S > 9.0$ mm, the coherent structures seize to exist since the difference in the channel-gap velocities is below a certain required

threshold. Under this condition, i.e., turbulent flow in the gap region without coherent structures, crossflow mixing exists merely because of turbulent mixing.

(ii) For intermediate gap size ranges of $3.0\ \text{mm} < S < 9.0\ \text{mm}$, the coherent structures and the turbulence (in the gap region not occupied by the structures) coexist. In this case, the crossflow mixing depends on the tracer residence time in a structure (which depends on the structure volume and tracer mixing within a structure) and the turbulent mixing outside a structure in the gap region. The assumption of well-mixed tracer in a structure, used in the derivation of CST based crossflow mixing model, holds for intermediate gap sizes. Because of all the above-mentioned effects, the crossflow mixing becomes more effective in this range of gap sizes compared to the crossflow mixing due to turbulent mixing alone. In other words, the presence of large-scale structures, in the intermediate range of gap sizes, enhances the crossflow mixing on top of turbulence. As a first approximation, the contribution of coherent structures towards crossflow mixing, in the presence of turbulent mixing, is nearly 48%.

(iii) As the gap size is reduced below 3.0 mm, i.e., from intermediate to small gap sizes, coherent structures do exist but due to laminarization of the gap flow, there is no turbulence between the structures in the gap region and possibly within a structure anymore. Consequently, for small gap sizes the crossflow mixing is far less effective as compared to the case of crossflow mixing due to combination of turbulent mixing and coherent structures. Crossflow mixing, obviously, approaches to zero in case the gap size is further reduced.

6. Qualitatively the crossflow dependency on the gap hydraulic diameter, streamwise structure length and Re_{ch} are identical in both a tube bundle and compound channels. A quantitative equivalence in both the geometries is envisaged provided the gap related geometric parameters are comparable. Therefore, a crossflow mixing model based on experimental findings in compound channels is expected to be valid for a tube bundle as well.

7. For Re_{ch}=2690, a comparison of the measured crossflow and the computed (from LES) secondary flow magnitudes in compound channels, being 13% and 2.5% of the fluid bulk velocity, respectively, leads to the conclusion that the major contribution towards crossflow mixing comes from large-scale coherent structures rather than secondary flows. The same conclusion was found to be valid for the tube bundle geometry, since the magnitudes of the measured secondary flows and the crossflow in the gap region was found to be 0.9% and 5.0% of the fluid bulk velocity, respectively.

8. Fluorinated Ethylene Propylene (FEP) can be effectively used as a solid refractive index matching material with water at ambient conditions. Care, however, should be taken to the attenuating and reflection effect of the material.
9. As compared to the experimental findings, use of the Large Eddy Simulations (LES) is found adequate to compute the characteristics of large-scale coherent structures, at $Re_{ch} = 2690$, in compound channels with a rectangular gap of 3.0 mm. The triple decomposition of the numerical data (by using Proper Orthogonal Decomposition technique) can be used to distinguish the coherent structures from the incoherent part.

The present work offers a first step in characterizing the coherent structures formed in narrow gaps and their role in crossflow mixing. The crossflow mixing model proposed is solely based on the characteristics of large-scale coherent structures. An attempt was made to quantify the role of turbulence in crossflow mixing, this part, however, fell short due to the limitations of the optical measurement techniques. Nevertheless, the structure based inter-channel cross flow mixing model proposed in this thesis covers a large range of Reynolds numbers and it is expected to enhance the capabilities of existing single channel analysis codes for all flow conditions of the coolant inside the core.

Recommendations for future work

Crossflow mixing was found to be a function of the scalar residence time in a coherent structure and the streamwise length of the gap region occupied by coherent structures. During the current study, no specific experimental measurements were performed to determine these two parameters. In the proposed crossflow mixing model the formulation of these parameters was based on information available in previous (near) relevant literature. It is highly recommended, however, to investigate these parameters in further detail to help improve the proposed model because of the following reasons:

1. Most of the available information on a scalar residence time pertains to the coherent vortices found in free shear layer type flows. Whereas, compound channels/tube bundle geometry belongs to a wall bounded type shear flow and the vortex dynamics in this case is different as compared to free shear flows.
2. Similarly, the existing literature on the vortex formation length (that exists before attaining a fully developed crossflow due to large-scale coherent structures) generally belongs to free shear flows. Additionally, in case of wall bounded shear flows, the vortex formation length in the relevant literature is reported to be a function of the geometry.

Based on the experience gained and conclusions drawn from the study, the following future work is suggested for resolution of the above-mentioned issues:

- To perform crossflow and crossflow mixing experiments in compound channels having a gap region shape similar to the one in a tube bundle. As an example, Figure 6-1 shows a cross-sectional view of such a setup with a more realistic gap geometry. In contrast to a tube bundle, in this setup the gap depth (D) and the minimum gap spacing (S) are relatively easy to vary. In addition, compound channels are best suited for optical measurement techniques, since in a tube bundle the multi-layered refractive index matching material may cause light attenuation problems. The use of non-intrusive, optical measurement techniques, preferably PIV, for the compound channels setup shown in Figure 6-1 is proposed for the investigation of large-scale structures/crossflow in the gap region. PIV has the advantage over point measurement techniques of finding the structure velocity, with relative ease, by using two points cross-correlation. The refractive index matching can be achieved by making curved surfaces out of FEP.

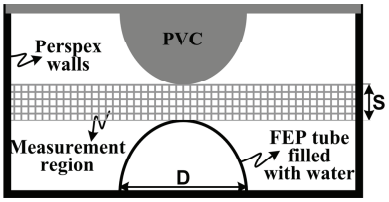

Figure 6-1: Cross-sectional view of a proposed compound channels setup for future study, based on the PIV measurement technique.

- Besides global crossflow mixing measurements (as was done in this work), determine the local, instantaneous concentration field in the gap region by using, e.g., Planar Laser Induced Fluorescence (PLIF) technique. This helps in characterizing the lateral transport of a passive scalar by a large-scale vortex, such as the residence time distribution of tracer material in a large-scale vortex (a quantity used in the proposed crossflow mixing model).
- By using PIV measurements determine the dependency of the vortex formation length on the channel Reynolds number and gap geometric parameters.
- A valuable addition to the crossflow measurements in a tube bundle geometry would be to obtain crossflow mixing data in such a geometry. One of the options could be the use of wire mesh sensors [67]. With the help of this technique, local single-phase crossflow mixing data in the lateral plane of a tube bundle can be obtained. Furthermore, the streamwise structure velocity might be estimated by cross correlating the crossflow mixing data series obtained from two wire mesh sensors separated by a certain streamwise distance. This leads to a more accurate prediction of structure size from the characteristic time scale of cross velocity pulsations in the gap region.

References

[1] Lin, B., Shiono, K., Numerical modeling of solute transport in compound channel flows, J. Hydraulic Research, 33(1995), pp. 773-788.

[2] Li, H. Y., Chao, S. M., Measurement of performance of plate-fin heat sinks with cross flow cooling, Int. J. Heat Mass Transfer, 52 (2009), pp. 2949-2955.

[3] Möller, S.V., On phenomena of turbulent flow through rod bundles, Exp. Thermal Fluid Sci., 4 (1991), pp. 25-35.

[4] The Future of Nuclear Power: an interdisciplinary MIT study, MIT Press (2003).

[5] Rogers, J.T., Todreas, N.E., Coolant interchannel mixing in reactor fuel rod bundles single-phase coolants, ASME Annual Winter Meeting, New York, U.S.A. (1968).

[6] Wu, X., On the transport mechanisms in simulated heterogeneous rod bundle subchannels, Nucl. Eng. Des. 158 (1995), pp. 125–134.

[7] Rowe, D. S., Measurement of turbulent velocity, Intensity and scale in rod bundle flow channels, PhD.-Thesis, Oregon State University, BNWL-1736, Battelle Pacific Northwest Laboratories, Richland, Washington (1973).

[8] Rowe, D. S., Johnson, B. M., Knudsen, J. G., Implications concerning rod bundle crossflow mixing based on measurements of turbulent flow structure", Int. J. Heat Mass Transfer, 17(1974), pp. 407-419.

[9] Rehme, K., The structure of turbulent flow through a wall subchannel of a rod bundle, Nucl. Eng. Des., 45(1978), pp. 311-323.

[10] Hooper, J. D., Developed single phase turbulent flow through a square-pitch rod cluster, Nucl. Eng. Des., 60(1980), pp. 365-379.

[11] Hooper, J. D., Rehme, K., Large-scale structural effects in developed turbulent flow through closely-spaced rod arrays, J. Fluid Mech., 145(1984), pp. 305-337.

[12] Hooper, J. D., Wood, D. H., Fully developed rod bundle flow over a large range of Reynolds number, Nucl. Eng. Des., 83(1984),pp. 31-46.

[13] Wu, X., Trupp, A.,C., Experimental study on the unusual turbulence intensity distributions in rod-to-wall gap regions, Exp. Thermal Fluid Sci., 6(1993), pp. 360-370.

[14] Meyer, L., Rehme, K., Large scale turbulence phenomena in compound rectangular channels, Exp. Thermal Fluid Sci, 8(1994), pp. 286-304.

[15] Guellouz, M. S., Tavoularis, S., The structure of turbulent flow in a rectangular channel containing a cylindrical rod, Exp. Thermal Fluid Sci., 23(2000), pp. 59-91.

[16] Lexmond, A. S., Mudde, R. F., van der Hagen, T., Visualization of the vortex street and characterization of the cross flow in the gap between two sub-channels, NURETH-11, Avignon, France, Oct. 2-6, (2005).

[17] Baratto, F., Bailey, S. C. C., Tavoularis, S., Measurements of frequencies and spatial correlations of coherent structures in rod bundle flows, Nucl. Eng. Des., 236(2006), pp. 1830-1837.

[18] Rogers, J. T., Tahir, A. E. E., Turbulent interchange mixing in rod bundles and the role of secondary flows, ASME Paper 75-HT-31 (1975).

[19] Möller, S. V., Single-phase turbulent mixing in rod bundles, Exp. Thermal Fluid Sci., 5(1992), pp. 26-33.

[20] Rehme, K., The structure of turbulence in rod bundles and the implications on natural mixing between the subchannels, Int. J. Hear Mass Transfer, 35(1992), pp. 567-581.

[21] Guellouz, M. S., Tavoularis, S., Heat transfer in rod bundle subchannels with varying rod-wall proximity, Nucl. Eng. Des., 132(1992), pp. 351-366.

[22] Biemüller, M., Meyer, L., Rehme, K., Large eddy simulation and measurement of the structure of turbulence in two rectangular channels connected by a gap, Engineering Turbulence Modeling and Experiments 3, Proc. of the 3rd Int. Symp., Heraklion, Greece, May 27-29, 1996; Ed. Rodi, W., Bergeles, G., Elsevier (1996), pp. 249-258.

[23] Merzari, E., Ninokata, H., Mahmood, A., Rohde, M., Proper orthogonal decomposition of the flow in geometries containing a narrow gap, Theor. Comp. Fl. Dyn., 23(2009), pp. 333-351.

[24] Meyer, L., From discovery to recognition of periodic large scale vortices in rod bundles as source of natural mixing between subchannels-A review, Nucl. Eng. Des., 240(2010), 1575-1588.

[25] van der Ros, T., Bogaardt, M., Mass and heat exchange between adjacent channels in liquid-cooled rod bundles, Nucl. Eng. Des., 12(1970), pp. 259-268.

[26] Chang, D., Tavoularis, S., Unsteady numerical simulation of turbulence and coherent structures in axial flow near a narrow gap, J. Fluid Eng., 127 (2005), pp. 458-466.

[27] Vonka, V., Measurement of secondary flow vortices in a rod bundle, Nucl. Eng. Des., 106(1988), pp. 191-207.

[28] Vonka, V., Turbulent transports by secondary flow vortices in a rod bundle, Nucl. Eng. Des., 106(1988), pp. 209-220.

[29] Ikeno, T., Kajishima, T., Analysis of dynamical flow structure in a square arrayed rod bundle, Nucl. Eng. Des., 240(2010), pp. 305-312.

[30] Westerweel, J., Fundamentals of digital particle image velocimetry, Meas. Sci. Technol., 8(1997), pp. 1379-1392.

[31] Street, R. L., Watters, G., Z., Vennard, J., K., Elementary fluid mechanics, 7th ed., (1996), Wiley, New York, pp. 335-338.

[32] Menter, F., R., Two-equation eddy-viscosity turbulence models for engineering applications. AIAA Journal, 32(1994), pp. 1598-1605.

[33] Sagaut, P., Large Eddy Simulation for Incompressible Flows: An introduction, 2nd ed., (2004), Springer, Berlin.

[34] Gavrilakis, S., Numerical simulation of low-Reynolds-number turbulent flow through a straight square duct, J. Fluid Mech., 244 (1992), pp. 101-129.

[35] Adrian, R., J., Christensen, K., T., Liu, Z., C., Analysis and interpretation of instantaneous turbulent velocity fields, Exp. Fluids, 29(2000), pp. 275-290.

[36] Chong, M., S., Perry, A., E., Cantwell, B., J., A general classification of three-dimensional flow fields, Phys. Fluids A2(5), (1990), pp. 765-777.

[37] Winant, C., D., Browand, F., K., Vortex pairing: the mechanism of turbulent mixing layer growth at moderate Reynolds number, J. Fluid Mech., 63 (1974), pp. 237-255.

[38] Brown, G., L., Roshko, A., On density effects and large structure in turbulent mixing layers, J. Fluid Mech., 64 (1974), pp. 775-816.

[39] Brereton, G., J., Kodal, A., An adaptive filter for decomposition of organized turbulent flows, Phys. Fluids, 6 (1994), pp. 1775–1786.

[40] Farge, M., Schneider, K., Pelligrino, G., Wray, A., Rogallo, R., Coherent vortex extraction in three dimensional homogeneous turbulence: comparison between CVS-wavelet and POD-Fourier decompositions, Phys. Fluids, 15 (2003), pp. 2886–2896.

[41] Delville, J., Ukeiley, L., Cordier, L., Bonnet, J., P., Glauser, M., Examination of large-scale structures in a turbulent plane mixing layer. Part 1. Proper orthogonal decomposition, J. Fluid Mech., 391 (1999), pp. 91–122.

[42] Berkooz, G., Holmes, P., Lumley, J., L., The proper orthogonal decomposition in the analysis of turbulent flows, Annu. Rev. Fluid Mech., 25(1993), pp. 539-575.

[43] Skinner, V., R., Freeman, A., R., Lyall, H., G., Gas mixing in rod clusters, Int. J. Heat Mass Transfer, 12(1969), pp. 265-278.

[44] Singh, K., Pierre, St., C., C., Single phase turbulent mixing in simulated rod bundle geometries, Trans. CSME, 1(1972), pp. 73-80.

[45] Trup, A., C., Azad, R., S., The structure of turbulent flow in triangular array rod bundles, Nucl. Eng. Des., 32(1975), pp. 47-84.

[46] Durst, F., Melling, A., Whitelaw, J., H., Principles and Practice of Laser Doppler Anemometry, 2nd ed., 1981, Academic Press, London.]

[47] Tummers, M., J., Investigation of a turbulent wake in an adverse pressure gradient using laser Doppler anemometry. PhD thesis, 1999, Delft University of Technology, The Netherlands.

[48] Benedict, L., H., Nobach, H., Tropea, C., Estimation of turbulent velocity spectra from laser Doppler data, Meas. Sci. Technol., 11(2000), pp. 1089-1104.

[49] Nobach, H., Local time estimation for the slotted correlation function of randomly sampled LDA data, Exp. Fluids, 32(2002), pp. 337–345.

[50] Budwig, R., Refractive index matching methods for liquid flow investigations, Exp. Fluids, 17(1994), pp. 350–355.

[51] Hassan, Y., A., Dominguez-Ontiveros, E., E., Flow visualization in a pebble bed reactor experiment using PIV and refractive index matching techniques, Nucl. Eng. Des., 238(2008), pp. 3080-3085.

[52] F. M. White, Viscous fluid flow, 2nd ed., 1991, McGraw-Hill New York.

[53] Eggels, J., G., M., Unger, F., Weiss, M., H., Westerweel, J., Adrian, R., J., Friedrich, R., Nieuwstadt, F., T., M., Fully developed turbulent pipe flow: A comparison

between direct numerical simulation and experiment, J. Fluid Mech., 268(1994), pp. 175–209.

[54] den Toonder, J., M., J., Drag reduction by polymer additives in a turbulent pipe flow: laboratory and numerical results, PhD thesis, 1996, Delft University of Technology, The Netherlands.

[55] Bonnet, J., P., Delville, J., Glauser, M., N., Antonia, R., A., Bisset, D., K., Cole, D., R., Fiedler, H., E., Garem, J., H., Hilberg, D., Jeong, J., Kevlahan, N., K., R., Ukeiley, L., S., Vincendeau, E., Collaborative testing of eddy structure identification methods in free turbulent shear flows, Exp. Fluids, 25(1998), pp. 197–225.

[56] Galbraith, K., P., Knudsen, J., G., Turbulent mixing between adjacent channels for single-phase flow in a simulated rod bundle, 12th Natl. Heat Transfer Conf. Tulsa, AIChE Symp. Ser. 68 (1971), pp. 90–100.

[57] Kraichnan, R., H., Inertial ranges in two-dimensional turbulence, Phys. Fluids, 10(1967), pp. 1417-1423.

[58] Brian L. White, B., L., Nepf, H., M., Scalar transport in random cylinder arrays at moderate Reynolds number, J. Fluid Mech., 487(2003), pp. 43–79.

[59] Breidenthal, R., Structure in turbulent mixing layers and wakes wing a chemical reaction, J. Fluid Mech., 109(1981), pp. 1–24.

[60] Browand, F., K., The structure of the turbulent mixing layer. Physica D18(1986), pp. 135–148.

[61] MacLennan, A., S., M., Vincent, J., H., Transport in the near aerodynamic wakes of flat plates, J. Fluid Mech., 120(1982), pp. 185-197.

[62] Personal communication with Dr. ir. Martin Rohde (Assistant Professor), PNR-R3, TNW, Delft University of Technology, The Netherlands.

[63] Davidson, P., A., Turbulence: an introduction for scientists and engineers, Oxford University Press (2004).

[64] Saarenrinne, P., Piirto, M., Turbulent kinetic energy dissipation rate estimation form PIV velocity vector fields, Exp. Fluids, 29(2000), pp. 300-307.

[65] Unal, M., F., Rockwell, D., On vortex formation from a cylinder. Part 1. The initial instability, J. Fluid Mech., 190(1988), pp. 491-512.

[66] Norberg, C., LDV measurements in the near wake of a circular cylinder," in Proceedings of the 1998 Conference on Bluff Body Wakes and Vortex-Induced Vibration, Washington, DC, edited by Bearman, P., W., and Williamson, C., H., K., (1998), pp. 1–12.

[67] Prasser, H., M., Grunwald, G., Rohde, U., Kliem, S., Höhne, T., Karlsson, R., Weiss, F., P., Coolant mixing in a Pressurized Water Reactor: Deboration transients, steam line breaks and emergency core cooling injection, Nucl. Technol. 143(2003), pp. 37-56.

Appendix – A

Derivation of a crossflow mixing model

A-1 Tracer transport in a single CST

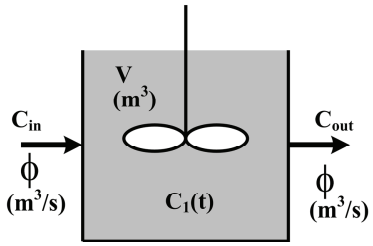

Figure A-1: A single continuous stirred tank (CST) of volume V with inlet and outlet volumetric flow rate of ϕ.

Figure A-1 shows the schematic of a single CST. The step response of a CST (C_{out}) to the injection of a tracer of concentration C_{in} at the inlet is given by the following equation:

$$V\frac{dC_1}{dt} = C_{in}\phi - C_{out}\phi \tag{A-1}$$

$$V\frac{dC_1}{dt} = (C_{in} - C_{out})\phi \tag{A-2}$$

$$\frac{dC_1}{(C_{in} - C_{out})} = \frac{\phi}{V}dt \tag{A-3}$$

Integrating between time 0 to t with corresponding concentrations $C_{out}(0)=C_o$ and $C_{out}(t)=C_1$

$$\int_{C_o}^{C_1}\frac{dC_1}{(C_{in} - C_1)} = \frac{\phi}{V}\int_0^t dt \tag{A-4}$$

$$\ln\frac{(C_{in} - C_1)}{(C_{in} - C_o)} = -\frac{\phi}{V}t \tag{A-5}$$

Further simplification leads to:

$$C_1(t) = C_{in} - (C_{in} - C_o)e^{-\frac{t}{\tau}} \tag{A-6}$$

where $\tau = \frac{V}{\phi}$ = the residence time of tracer in CST

The derivation of Equation (A-6) is based on the assumption that the tracer is instantly mixed with the bulk fluid in the CST and is non-reactive with fluid/walls.

A-2 Crossflow mixing by a series of CST

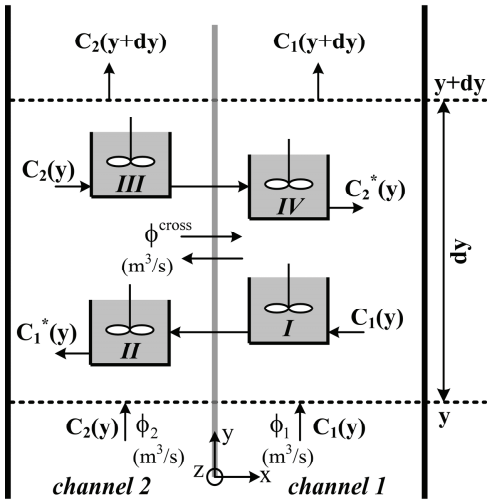

Figure A-2: Layout of change in tracer concentration (C) over a streamwise length dy. The spanwise tracer transport within dy, by a coherent structure, is assumed to take place through four CST's. Subscripts 1 and 2 identifies channel 1 and 2, respectively. Superscript * shows the change in spanwise tracer concentration within dy.

From Figure A-2, the stationary mass balance for channel 1 over a small streamwise section dy yields the following equation:

$$\phi_1 C_1(y) - \phi_1 C_1(y+dy) - \frac{1}{2}\phi_{12}^{cross} C_1(y) + \frac{1}{2}\phi_{21}^{cross} C_2^*(y) = 0 \qquad \text{(A-7)}$$

similarly for channel 2:

$$\phi_2 C_2(y) - \phi_2 C_2(y+dy) - \frac{1}{2}\phi_{21}^{cross} C_2(y) + \frac{1}{2}\phi_{12}^{cross} C_1^*(y) = 0 \qquad \text{(A-8)}$$

where

ϕ_1 = streamwise volumetric flow rate in channel 1;

ϕ_2 = streamwise volumetric flow rate in channel 2;

ϕ_{12}^{cross} = spanwise volumetric flow rate from channel 1 to 2;

ϕ_{21}^{cross} = spanwise volumetric flow rate from channel 1 to 2;

C_1 = tracer concentration in channel 1;

C_2 = tracer concentration in channel 2;

C_1^* = tracer concentration in fluid transferred laterally from channel 1 to 2 after passing through CST I and II;

C_2^* = tracer concentration in fluid transferred laterally from channel 2 to 1 after passing through CST III and IV.

Subtracting Equation (A-8) from Equation (A-7) and simplifying using

$$\phi_1 = \phi_2 = A_{ch} V_{bulk} \text{ and } \phi_{12}^{cross} = \phi_{21}^{cross} = Su^{rms} dy ,$$

yields:

$$- A_{ch} V_{bulk} \frac{d(C_1 - C_2)}{dy} dy - \frac{1}{2} u^{rms} S\left(C_1 - C_2 - C_2^* + C_1^*\right) dy = 0 \qquad \text{(A-9)}$$

where

A_{ch} = half of the cross sectional flow area of the test sections;

A_{gap} = the streamwise gap area facing channel 1 / 2);

S = minimum gap spacing;

V_{bulk} = bulk velocity;

u^{rms} = cross velocity fluctuations in the center of the gap region.

Considering the spanwise tracer transfer, due to a coherent structure, from channel 1 to 2 (C_1^*) through CST 1 and 2 (see Figure A-2), C_1^* can be estimated from Equation (A-6) as:

$$C_1^*(t) = C_1(t)\left(1 - e^{-\frac{t}{\tau}}\right)^2 \qquad \text{(A-10)}$$

Assuming that transport of tracer in the streamwise direction, y, is carried out by a coherent structure moving with velocity v^{str}, Equation (A-10) can be made independent of t by using:

$$t = \frac{y}{v^{str}} \qquad \text{(A-11)}$$

Therefore, Equation (A-10) becomes:

$$C_1^*(y) = C_1(y)\left(1 - e^{-\frac{y}{v^{str}\tau}}\right)^2 \tag{A-12}$$

and for channel 2:

$$C_2^*(y) = C_2(y)\left(1 - e^{-\frac{y}{v^{str}\tau}}\right)^2 \tag{A-13}$$

Substitution of Equations (A-12) and (A-13) in (A-9) gives:

$$-A_{ch}V_{bulk}d(C_1 - C_2) = u^{rms}S(C_1 - C_2)\left(1 - e^{\frac{-y}{v^{str}\tau}}\right)^2 dy \tag{A-14}$$

By taking C_1-C_2=ΔC in Equation (A-14) and rearranging different terms results in:

$$\frac{d\Delta C}{\Delta C} = -\frac{u^{rms}S}{A_{ch}V_{bulk}}\left(1 - e^{\frac{-y}{v^{str}\tau}}\right)^2 dy \tag{A-15}$$

Integrating between the limits y=0 and y=L, Equation (A-15) can be written as:

$$\frac{\Delta C(L)}{\Delta C(0)} = \exp\left[-\frac{u^{rms}S}{A_{ch}V_{bulk}}\left(L - \frac{v^{str}\tau}{2}\left(e^{-\frac{2L}{v^{str}\tau}} - 4e^{-\frac{L}{v^{str}\tau}} + 3\right)\right)\right] \tag{A-16}$$

Expanding in terms of ΔC yields:

$$\frac{C_1(L) - C_2(L)}{C_1(0) - C_2(0)} = \exp\left[-\frac{u^{rms}S}{A_{ch}V_{bulk}}\left(L - \frac{v^{str}\tau}{2}\left(e^{-\frac{2L}{v^{str}\tau}} - 4e^{-\frac{L}{v^{str}\tau}} + 3\right)\right)\right] \tag{A-17}$$

Considering injection of tracer in Channel 1:

$C_1(0)=C_o$

$C_2(0)=0$

$C_1(L)+C_2(L)=C_o$

Application of these boundary conditions results in:

$$\theta = \frac{C_2(L)}{C_o} = \frac{1}{2}\left[1 - \exp\left[-\frac{u^{rms}S}{A_{ch}V_{bulk}}\left(L - \frac{v^{str}\tau}{2}\left(e^{-\frac{2L}{v^{str}\tau}} - 4e^{-\frac{L}{v^{str}\tau}} + 3\right)\right)\right]\right] \qquad \text{(A-18)}$$

The proposed simplistic crossflow mixing model Equation (A-18) is derived by considering an infinite series of CST's in the axial direction with each CST having a finite length. Consequently, the model is based on a smooth axial tracer concentration profile whereas in reality it should be a discretized one.

A-3 Turbulence model for crossflow mixing

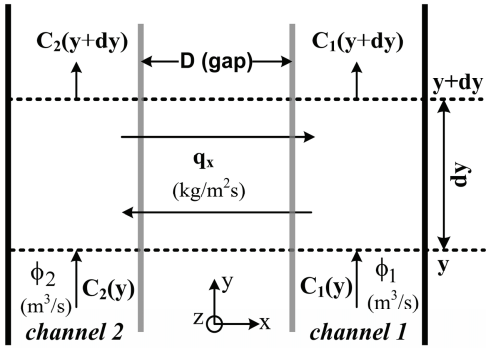

Figure A-3: Schematic of the mass balance over a streamwise length dy with q_x as the spanwise inter-channel mass flux through the gap of depth D and spacing S. Subscript 1 and 2 corresponds to channel 1 and 2, respectively.

From Figure A-3, the mass balance for channel 1 over a small streamwise section dy can be written as:

$$\phi_1 C_1(y) - \phi_1 C_1(y + dy) - S q_x dy = 0 \qquad \text{(A-19)}$$

similarly for channel 2:

$$\phi_2 C_2(y) - \phi_2 C_2(y + dy) + S q_x dy = 0 \qquad \text{(A-20)}$$

where

q_x = spanwise inter-channel mass flux through the gap region;

Subtracting Equation (A-20) from Equation (A-19) and simplifying by using

$$\phi_1 = \phi_2 = A_{ch}V_{bulk} \text{ and } C_1 - C_2 = \Delta C,$$

yields:

$$-A_{ch}V_{bulk}\frac{d(\Delta C)}{dy}dy - 2Sq_x dy = 0 \tag{A-21}$$

In Equations (A-19) to (A-21), ϕ_1, ϕ_2, S, C, A_{ch} and V_{bulk} have same meanings as given in § A-2.

Assuming that the spanwise mass flux through the gap region can be related to turbulent mass diffusivity (D_t) and change in the spanwise tracer concentration as:

$$q_x = -D_t\frac{\partial C}{\partial x} \approx -D_t\frac{(C_1 - C_2)}{(0 - D)} \approx D_t\frac{\Delta C}{D} \tag{A-22}$$

where D is the spanwise gap depth. Furthermore, it is assumed that by using Reynold's analogy the turbulent mass diffusivity can be related to turbulent viscosity as:

$$D_t \approx \nu_t \tag{A-23}$$

Using Equations (A-22) and (A-23) in Equation (A-21) and rearranging different terms results in:

$$\frac{d(\Delta C)}{\Delta C} = -2\frac{S\nu_t}{A_{ch}V_{bulk}D}dy \tag{A-24}$$

Integrating between the limits y=0 and y=L, Equation (A-24) can be written as:

$$\frac{\Delta C(L)}{\Delta C(0)} = \exp\left(-2\frac{SL\nu_t}{A_{ch}V_{bulk}D}\right) \tag{A-25}$$

Expanding in terms of ΔC yields:

$$\frac{C_1(L) - C_2(L)}{C_1(0) - C_2(0)} = \exp\left(-2\frac{SL\nu_t}{A_{ch}V_{bulk}D}\right) \tag{A-26}$$

Considering injection of tracer in Channel 1:

$C_1(0)=C_o$

$C_2(0)=0$

$C_1(L)+C_2(L)=C_o$

Application of these boundary conditions results in:

$$\theta = \frac{C_2(L)}{C_o} = \frac{1}{2}\left[1 - \exp\left(-2\frac{SL\nu_t}{A_{ch}V_{bulk}D}\right)\right] \tag{A-27}$$

Acknowledgements

Several individuals and institutions provided vital support during the evolution of the research work presented in this thesis. Higher Education Commission of Pakistan and Delft University of Technology (TUDelft), The Netherlands, provided financial support for the research. The last mentioned has provided me with a congenial intellectual home for nearly four years and has been generous in its investment of time and resources. The experimental work would not have been possible without the excellent support staff and facilities available at the Reactor Institute Delft and Kramers Laboratorium. In this context I am grateful to Dick, August, Jaap van Raamt, Jaap Kamminga, Wouter and Evert for helping me out in realizing the experimental setups with their expertise. Special thanks go to Ine Olsthoorn for taking care of my pre-defense formalities.

Above all, my deepest gratitude is to my supervisors Tim, Rob and Martin for their comments, suggestions and encouragement during my work at TUDelft. My interaction with Tim and Rob was mostly during our monthly review meetings. During the event, they both always encouraged me to speak up and get involved in constructive discussions. Their skills in guiding me towards a workable solution were remarkable. I am indebted to Tim and Rob for their support and keeping my research on track.

Martin was the one with whom I interacted most during my research, since he was my day-to-day supervisor. He was the one constantly exposed to my laziness and poor writing skills (good for Tim and Rob). Nevertheless, he handled every situation patiently (most of the time) and tactfully. I also had a very pleasant family interaction with Martin and surprisingly found out that he likes spicy food (a rarity in Dutch people). I would like to thank Martin for extending me a technical and personal support during my stay at TUDelft.

In the end, I am grateful to my family and friends for their constant moral support during my stay in The Netherlands.

About the author

1st of March 1965	Born in Lahore, Pakistan.
1986 to 1988	Obtained M.Sc. degree in Physics from Punjab University, Lahore, Pakistan.
1990 to 1992	Carried out Master's studies in Nuclear Engineering from Quaid-e-Azam University, Islamabad, Pakisan.
1992 to 2006	Joined Pakistan Atomic Energy Commission and worked as a safety analyst for nuclear power plants.
2006 to 2010	Pursued Ph.D. studies at TUDelft, The Netherlands, and investigated crossflow mixing in a vertical tube geometry.
2010 to date	Rejoined Pakistan Atomic Energy Commission and working at the position held prior to the doctoral studies.

Propositions

belonging to the Ph.D. thesis of Amer Mahmood

1. Besides turbulent mixing and diversion crossflow mixing, coherent vortices play a major role in crossflow mixing in a tube bundle geometry.
2. Stochastic processes govern the coherent vortices induced crossflow mixing in a tube bundle geometry.
3. In laboratory scale setups, 2D/3D PIV is the best technique to study large-scale coherent vortices.
4. The welfare of a multi-ethnic and multi-cultural Pakistani society strongly depends on a long-term continuation of the ongoing democratic process in Pakistan.
5. The inability of a unipolar world order to create a safer world to live in necessitates the formation of a multipolar world order.
6. The dominant role of the industrial sector in initiating research activities has transformed the industry into a puppeteer and scientists into their marionettes.
7. Ignoring a blasphemic act is the best way to avoid its consequent spread to inter-religions conflicts.
8. “Clash of interests” is a more suitable title to Samuel P. Huntington’s “Clash of civilizations”.
9. Experts in the fields of marketing and public relations, not the nuclear scientists, can revive nuclear power.
10. Electronic and print media sell news rather than that they inform people.

These propositions are regarded as opposable and defendable, and have been approved as such by the supervisors, Prof. dr. ir T.H.J.J. van der Hagen and Prof. dr. R.F. Mudde.

Stellingen

behorende bij het proefschrift van Amer Mahmood

1. Naast turbulente menging en menging veroorzaakt door ‘diversion crossflow’ spelen coherente vortices een grote rol bij de radiale menging in een reactorbundel.
2. Radiale menging door coherente vortices in een reactorbundel worden bepaald door stochastische processen.
3. De beste techniek om grote, coherente vortices in opstellingen op laboratoriumschaal te bestuderen is 2D/3D PIV.
4. De welvaart van een multi-etnische en multiculturele, Pakistaanse maatschappij is sterk afhankelijk van een langdurige voortzetting van het lopende democratiseringsproces in Pakistan.
5. Het onvermogen van een unipolaire wereldorde om een veiliger wereld te creëren laat de noodzaak van een multipolaire wereldorde zien.
6. De dominante rol van de industrie in het initiëren van onderzoeksinitiatieven heeft de industrie getransformeerd in poppenspelers en wetenschappers in haar marionetten.
7. Het negeren van een blasfemische daad is de beste manier om de daaruit voortkomende verspreiding van interreligieuze conflicten te vermijden.
8. “Clash of interest” is een passendere titel voor Samuel P. Huntington’s “Clash of civilizations”.
9. Niet de nucleaire wetenschappers maar de experts op het gebied van marketing en public relations kunnen zorgen voor een opleving van kernenergie.
10. Elektronische en gedrukte media verkopen nieuws in plaats van dat ze mensen informeren.

Deze stellingen worden opponeerbaar en verdedigbaar geacht en zijn als zodanig goedgekeurd door de promotoren, Prof. dr. ir T.H.J.J. van der Hagen en Prof. dr. R.F. Mudde.